Materials Science and Device Engineering for Organic Solar Cells

Nam Chul Cho

A dissertation
submitted in partial fulfillment of the
requirements for the degree of

Doctor of Philosophy

University of Washington
[2015]

Reading Committee:
Alex K-Y. Jen, Chair
Fumio S. Ohuchi
Xiaodong Xu
David S. Ginger

Program Authorized to Offer Degree:
Materials Science and Engineering

University of Washington

Abstract

Materials Science and Device Engineering for Organic Solar Cells

Nam Chul Cho

Chair of the Supervisory Committee:
Chair & Boing/Johnson Chair Professor Alex k-y Jen
Materials Science and Engineering

Solar cells are one of the important renewable energy sources as an alternative to fossil fuels. Since solar energy will never run out and harm the environment, the generation of electricity from solar energy is an ideal renewable energy source. During the last half-century numerous scientists have studied solar cells. By virtue of their tremendous efforts, the power conversion efficiency (PCE) of solar cells has significantly improved. In this dissertation, an overview of solar cell technology will be addressed in terms of materials development, device physics and engineering.

In chapter 1, working principles and developments of organic solar cells (OCSs) are briefly described. In chapters 2-5, *in-situ* n-doping and crosslinking of several interfacial materials, including fullerene derivatives and n-type semiconducting polymers, are described. The functionality and impact of solvent resistance and high conductivity of interfacial materials on

device performances are characterized in OSCs and organic thin-film transistor (OTFT) devices using X-ray photoelectron spectroscopy (XPS).

Chapter 6 shows the morphological evolution in bulk heterojunctions (BHJs) by controlling solvent-solute interactions using a binary solvent. The cohesive energy and solubility parameters, as well as the relative aggregation or crystallization of the active materials, are studied for the binary solvent additives.

In chapter 7, high dielectric constant photoactive functional side-chain polymers for controlling charge recombination dynamics in heterojunction polymer-fullerene solar cells are discussed. The photoactive polymers possessing nitrile side-chains show a 40% increase in dielectric constant (ε_r) at frequencies from 10^3-10^6 Hz. Bilayer heterojunctions made with the high dielectric polymer show improvements in device performance. Electroluminescence and sum-frequency generation experiments suggest that these increases are most likely not due to changes in the energy of the charge transfer state or changes in interface dipoles, while transient photovoltage measurements show that these improvements in device performance appear to be linked to suppressed non-geminate charge recombination rates.

TABLE OF CONTENTS

LIST OF FIGURES

LIST OF TABLES

ACKNOWLEDGEMENTS

I gratefully acknowledge Professor Alex Jen for giving me the opportunity to join his group and work for organic photovoltaic research. I am thankful for his guidance and financial support for the entire period of my PhD study. Professor Jen maintained an exciting research lab and I am honored to have been a part of his group. I also want to thank my committee members, Dr. Fumio Ohuchi, Dr. Xiaodong Xu and Dr. David Ginger for their effort and advices for my thesis.

The members of the Jen group have been good friends to me, and I really appreciate all of the great helps that I have received from lab-mates over the years. Dr. Hin-Lap Yip, Dr. Steven Hau, Dr. Kirsty Leong, Dr. Kevin O'Malley, Dr. Jingyu Zou, Kung-Shih Chen, Dr. Chang-Zhi Li, Dr. Chu-Chen Chueh, Nathan Cernetic, Dr. Su Huang, Dr. Jingdong Luo, Dr. Sei-Hum Jang, Dr. Hong Ma, Dr. Jeremy Intemann, Dr. Lijian Zuo, Dr. Jong Hyun Kim, Dr. Jaewoong Jung, Dr. Nara Cho, Shengqiang Liu, Po-Wei Liang, Spencer Williams, Ting Zhao, Brian Tran, Adharsh Rajagopal, and Caitlin Cramer.

I would like to acknowledge Dr. Cody Schlenker, Dr. Patrick Koelsch, Dr. Ben Krueger, Dr. Kristina Knesting, and Dr. Fei Ma from Departments of Chemistry, Chemical Engineering, and Physics for providing professional discussions and collaboration opportunities.

I would also like to thank my previous supervisor Professor Kwang-sup Lee for his endless love and help during my undergraduate and master degree. Without his help and trust I would not have been able to go this far. I would also like to thank Professor Tae-Dong Kim for all of the advice and especially some financial support. I'll never forget about it.

My deepest appreciation belongs to my parents, my sister, brother, wife, and daughters. Special thanks go to my wife Kyoung-Son. Her love and understanding are the strongest support for me to finish my PhD degree.

DEDICATION

I would like to dedicate my thesis to my wife Kyoung-Son Song who has always been there with me during my doctoral study.

Chapter 1. INTRODUCTION

1.1 INTRODUCTION

Solar cells are one of the important renewable energy sources as an alternative to fossil fuels. Renewable energy is the "*energy fueled in ways that do not use up natural resources or harm the environment*".[1] Since solar energy will never run out and harm the environment, the generation of electricity from the sun is an ideal renewable energy source. The following statement from Texas Solar Energy Society can help us to understand the importance of solar energy: "The amount of solar energy that falls on the earth's surface in 40 minutes equals the total annual energy consumption of all the world's people."[2] During the last half-century numerous scientists have studied solar cells. By virtue of their tremendous efforts, the power conversion efficiency (PCE) of the solar cells has significantly improved. In this dissertation, an overview of the solar cell technology will be addressed in terms of materials development, device physics and engineering.

1.2 ORGANIC SOLAR CELLS

Solar cells have been intensively studied since the development of the first solar cells at Bell Laboratories using crystalline silicon in the 1950s.[3] Currently, the PCE of crystalline silicon solar cells reaches up to 25%.[4] However, the high manufacturing cost of silicon solar cells is a main problem for market implementation. Organic solar cells (OSCs) bear the potential to develop low-cost, large area, lightweight, flexible, and transparent solar cells. This is due to the feasibility of tuning their opto-electrical and physical properties through molecular design and organic synthesis. In addition, polymeric materials are more suitable for flexible PSCs because of their intrinsic mechanical properties. Since the 1980s, when Tang demonstrated an organic

planar heterojunction solar cell with 1% of PCE, OSCs have become extensively studied and PCEs now reach up to more than 10%.[5] The performance of PSCs is mainly dependent on the electrical and optical properties of donor polymers[6-9] and acceptors[10, 11] in the active layer, and interfacial layers using electron transporting materials (ETMs) and hole transporting materials (HTMs).

In addition, careful device engineering to further control bulk and interface recombination, exciton dissociation and carrier transport is important to maximize PCE. Furthermore, to expand the economic viability of OSCs, their long-term stability also needs to be improved.

In general, OSCs are comprised of a BHJ active layer sandwiched between an indium tin oxide (ITO) anode and a low work-function metal cathode. A BHJ is ideally the bicontinuous composite of donor and acceptor phases with maximized interfacial area. BHJ solar cells are commonly made by solution processing of donor and acceptor materials. Figure 1.1 shows the general device structure and graphical illustration of a BHJ solar cell.

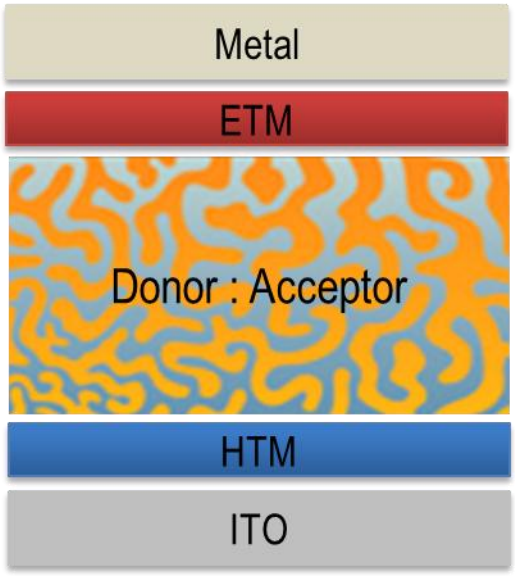

Figure 1.1 General device structure of BHJ polymer solar cells.

Compared to the bilayer structure, BHJ solar cells have higher exciton dissociation efficiency and PCE because the interface between donor polymer and acceptor materials has a larger surface area than that of the bilayer structure. By controlling the optical and electrical properties of donor and acceptor materials and the morphology of the active layer, high-performance devices can be fabricated.

1.2.1 *Device Configurations: Conventional and Inverted*

The long-term stability of OSCs is an important factor for their economic viability. The degradation of device performance for OSCs with conventional architecture is mainly due to the fact that low work-function top electrode metal, such as Ca and Al, is easily oxidized.[12]

To overcome this problem, PSCs with an inverted structure (ITO/ETM/BHJ active layer/HTM/metal anode stacks) have been developed. The inverted architecture enables the use of the air-stable high work-function metals, such as Ag or Cu, because the polarity of the device is reversed by the adoption of appropriate interfacial materials (ETMs and HTMs). [13, 14] Therefore, interfacial materials are one of the key elements for efficient inverted PSCs. Besides the advantage of air stability, high work function metals allow us to deposit the top electrode by using non-vacuum techniques such as lamination or direct printing.

1.2.2 *Exciton Generation and Dissociation in OSCs*

The working principles of OSCs with the schematic description of the exciton generation, diffusion, separation and transport of each carrier are outlined in **Figure 1.2**.

Figure 1.2a shows the process of exciton generation by absorbing light within donor materials (D). Generally organic materials have higher extinction coefficient (above 10^5 cm^{-1}) than inorganic materials. Therefore, the thickness of the active layer in OCSs is only ~100-200 nm,

which gives sufficient absorption yield in the devices. However, the thickness of inorganic thin film solar cells, for example, copper indium gallium selenide (CIGS) solar cells, is up to 1-2 micrometers. In the case of crystalline silicon solar cells, which is an indirect bandgap semiconductor, the thickness is more than 100 micrometers.

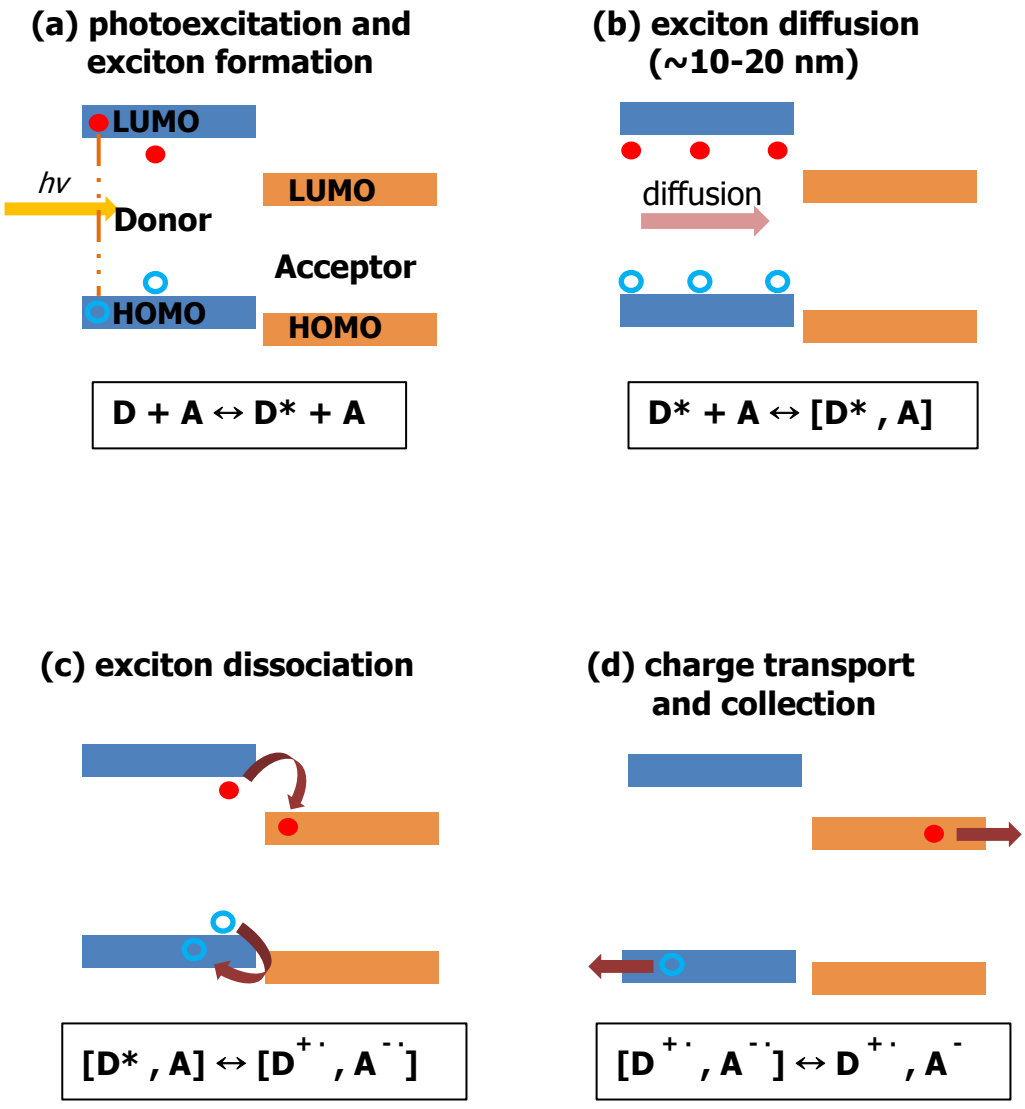

Figure 1.2 The illustration of exciton generation, diffusion, dissociation and transport of each carriers.

When the excitons generated from the donor material reach an interface by diffusion (**Figure 1.2b**), the electrons transfer to the acceptor material (A), yielding a coulombically bound electron-hole pair (**Figure 1.2c**). In OSCs, qmost of the exciton dissociation occurs solely across the donor/acceptor interfaces and when the energy loss from dissociation exceeds the exciton binding energy. The field dependent exciton dissociation probability, $P(F)$ can be described by Braun[15] and Onsager[16] theory as

$$P(F) = \frac{k_d(F)}{k_d(F) + k_f}$$

, where k_f, and k_d are the geminate recombination rate and the dissociation rate of excitons to free charge carriers, respectively. The field dependent exciton dissociation rate $k_d(F)$ can be simply described as

$$k_d(F) = \frac{3\gamma}{4\pi r^3} exp\left(-\frac{E_b}{kT}\right)$$

, where γ, r, E_b, and kT are the Langevin type bimolecular recombination rate, the exciton radius, the exciton binding energy, and the thermal energy, respectively.[17] Note that the exciton binding energy ($E_b = q^2/4\pi\varepsilon_o\varepsilon_r r$) and dielectric constant play a critical role in the exciton dissociation.

In practice, the dissociation efficiency can be influenced mainly by (i) dielectric constant of active materials,[18, 19] (ii) interfacial dipole between donor and acceptor,[20] (iii) conjugation length or energetic or spatial disorder of donor polymers,[21, 22] and (iv) additional local electric field generated by plasmonic effects or ferroelectric dipoles using ferroelectric materials.[23-25]

Lowering exciton binding energy by increasing the dielectric constant of active materials is the most fundamental approach to increase exciton dissociation efficiency. In organic semiconductors, direct thermally driven exciton dissociation is difficult because the exciton

binding energy (E_b~0.5-1 eV) is much larger than the thermal energy at room temperature (kT~0.025 eV) as a result of low relative dielectric constants (ε_r~2-4).

In addition to the dielectric constant, interfacial dipoles between donor and acceptor can influence the dissociation efficiency. Recently, the energy level offset between poly(3-hexylthiophene) (P3HT) and [6,6]-phenyl-C_{61} butyric acid methyl ester (PCBM) was successfully modified by incorporating surface segregated monolayers of fluorinated PCBM and P3HT.[20] Generally, materials that possess permanent dipoles can shift energy levels at the organic/metal and organic/organic interfaces and also within individual layers.[26-28] In organic solar cell devices, the interfacial dipole effect is most noticeable in the bilayer device architecture in which interfacial dipoles do not cancel each other, dissimilar to the BHJ devices.

Conjugation length and energetic or spatial disorder of donor polymers also play a crucial role in exciton dissociation. Very recently, Schwarz *at al*. have reported how the conjugation length of poly(*p*-phenylene) derivatives affect the exciton dissociation by field-dependent photocurrent measurement.[22] Previously, Deibel *at al*. used Monte Carlo simulation to point out that the improved delocalization of charge carriers by increasing conjugation length helps exciton dissociation.[21] As they claimed, better carrier delocalization results in higher local mobility, weaker binding energy of CT excitons, and concomitantly higher dissociation probability for electron-hole pairs.

1.2.3 *Recombination of Charge Carriers*

Once the bound electron-hole pairs have separated into free charge carriers, the free carriers transport to the electrodes and extracted (**Figure 1.2d**). During charge transport, charge carrier recombination can occur. This recombination process is called bimolecular or non-geminate recombination. Geminate, or monomolecular, recombination occurs during exciton

dissociation. In solar cell devices, a current density *J* is determined by the exciton generation and recombination of charge carriers, which can be described by the continuity equation:

$$-\frac{1}{q}\frac{dJ}{dx} = \mathrm{G} - \mathrm{R}$$

, where G and R are the exciton generation rate and non-geminate recombination rate, respectively. This means that the overall photocurrent in the device originate from the sum of photogenerated charge carrier current and a loss current:

$$J = J_{gen} + J_{loss}$$

Geminate and trap assisted recombination are considered as a first order process. Non-geminate recombination is considered as a second order process because two independent mobile carriers are involved in the recombination process. For disordered organic semiconductors with low charge carrier mobility ($\leq$1cm^2 V^{-1} s^{-1}), non-geminate recombination is the main recombination process. This type of recombination can simply be described by the Langevin recombination rate:

$$\gamma = \frac{q\mu}{\varepsilon_0 \varepsilon_r}$$

, where q and μ are the electron charge and electron or hole mobility, respectively.[29, 30]

In the bilayer devices, free electrons and holes transport through separated layers. Therefore, non-geminate recombination is minimal, which is the ideal case for charge transport. In BHJ solar cells, the morphology is crucial for efficient charge separation and transport.[31, 32] A bicontinuous phase-separated morphology with domain size on the order of several nanometers to tens of nanometers, matching the exciton diffusion length, can be described as the favorable morphology. This kind of disordered environment in BHJ causes severe non-geminate recombination resulting in shorter charge carrier lifetime (τ) and carrier density (n). The role of carrier lifetime on the change in open circuit voltage (Voc) can be seen in the equation below:[33]

$$qV_{oc} = \Delta E_{DA} - n_A k_B T ln\left(\frac{k_f}{k_d}\frac{k_{rec} N_H H_A}{J_x/a_o}\right)$$

, where k_{rec} (= 1/τ) is the bimolecular recombination rate, k_f and k_d are respectively the rate constants for polaron pair recombination and dissociation, N_H is the HOMO edge density of states on the donor side of the junction, H_A is the defect density on the acceptor side, J_X is the exciton flux reaching the donor/acceptor interface, a_o is the spatial extent of the polaron pair, ΔE_{DA} is the energy offset at the D/A interface, n_A is an ideality factor,[25, 26] k_b is Boltzmann's constant, and T is temperature. In chapter 7, we will show detailed experimental methods to evaluate carrier lifetimes, density, and their role in Voc.

1.2.4 *Extraction of Charge Carriers*

Extraction of charge carriers from the active materials to the electrodes is an important process in SCs. Thin interlayers introduced between the metal electrodes and the active layers significantly improve the charge extraction efficiency. This is because the interlayers reduce energetic barriers and tune interfacial dipoles at the metal/semiconductor interfaces. In addition, the interlayers minimize recombination by harvesting one charge carrier more rapidly than the other, preventing the accumulation of space charges at the interfaces. These thermodynamic and kinetic charge selectivity of interlayers are crucial for efficient charge extraction. However, a nonselective contact at the electrode causes severe recombination. Recombination at the interlayer/ semiconductor interfaces occurs if the transport of majority charge carriers from the active layer to the interlayer is faster than the transport of majority carriers through the interlayer to the electrodes. Recombination current at interfaces for electrons and holes is generally defined by the surface recombination rate S

$$J_s = qS[n(0) - n_0(0)] + qS[p(d) - p_0(d)]$$

, where q is the elementary charge, n_0 and p_0 are the equilibrium concentration of electrons and holes at the contacts, respectively. *n* and *p* are the charge carrier concentrations inside the device, respectively. In the above equation, the anode location is defined as x = 0 and the cathode location is defined as x = *d*. As we will discuss in chapter 2-5, we find that introducing a thin conducting interlayer is a powerful method to reduce the surface recombination. Particularly, we focused on developing in situ n-doped and crosslinked n-type semiconducting materials to make solvent resistant and highly conducting interlayers. Detailed materials properties and their electrical, optical, and physical properties will be discussed.

1.2.5 *Solar Cell Characterizations*

To characterize the device performance of the OSCs, the most important figure of merit is PCE. The PCE represents the ratio of the maximum output power to the incident light power, which can be obtained from current-voltage characteristics under a standard illumination condition. The standard air mass (AM) 1.5 global reference spectrum was shown in **Figure 1.3** **Figure 1.4** shows the schematic current–voltage characteristics of BHJ SCs.[34] The PCE can be determined by open circuit voltage (V_{oc}), short circuit current density (J_{sc}) and fill factor (*FF*), which are represented in the following equations.

$$PCE = \frac{P_{max}}{P_{in}} = \frac{V_{mpp} \times J_{mpp}}{P_{in}} = \frac{V_{oc} \times I_{sc} \times FF}{P_{in}}$$

, V_{mpp} and I_{mpp} are the voltage and current at the maximum power point. V_{oc} is the voltage where the J vs. V curve crosses the x-axis, and the short-circuit current (I_{sc}) is the current where the J vs. V curve crosses the y-axis. J_{sc} is defined as I_{sc} divided by device area. *FF* is defined as the quotient of P_{max} divided by the product of V_{oc} and I_{sc}. In real devices series resistance (contact

resistance) and parallel resistance (influenced by local shunts between two electrodes) are also an important factor for current density.

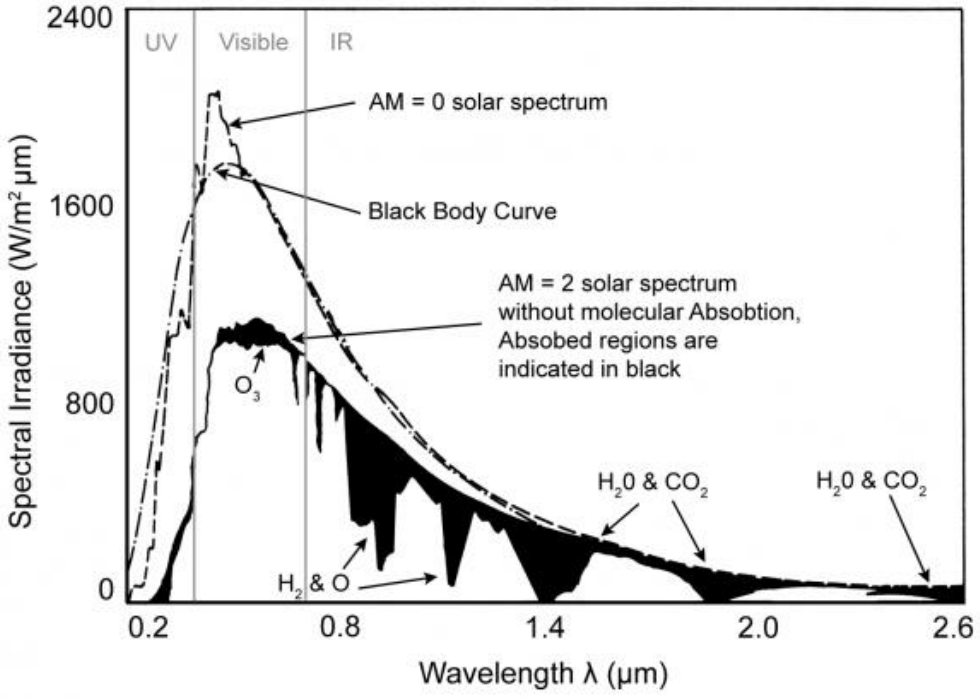

Figure 1.3 The AM 1.5 global solar spectrum [35]

The external quantum efficiency (EQE) is another important factor to evaluate the spectral response of a solar cell. EQE at a certain wavelength is the ratio of the photocurrent to the power of the incident monochromatic illumination, which can be expressed as:

$$EQE\ (\lambda) = 1.24 \frac{J_{sc}(\lambda)}{\lambda \times P(\lambda)}$$

, where λ is the wavelength of interest in the unit of micrometers, $J_{sc}(\lambda)$ is the short-circuit current density, and $P(\lambda)$ is the incident power density.

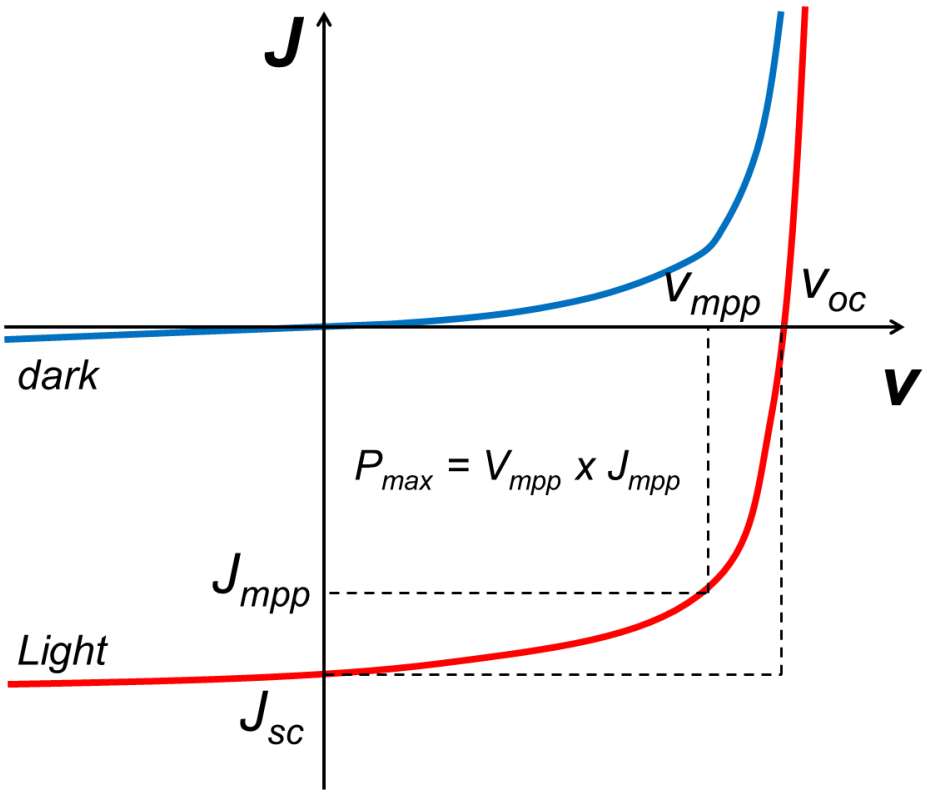

Figure 1.4 Typical current–voltage characteristics of BHJ SCs.

Chapter 2. N-DOPING OF THERMALLY POLYMERIZABLE FULLERENES AS AN ELECTRON TRANSPORTING LAYER FOR INVERTED POLYMER SOLAR CELLS

2.1 INTRODUCTION

As we mentioned earlier, PSCs with a conventional structure are comprised of a BHJ active layer sandwiched between an indium tin oxide (ITO) anode and a low work-function metal cathode. However, low work-function metal electrodes are quite unstable under ambient conditions.[15] To overcome this problem, PSCs with an inverted device structure had been developed which enables the use of stable and printable high work-function metals as hole collecting top electrodes and low work-function metal oxide as electron collecting bottom electrodes. This results in significantly improved stability in an ambient.[16,17]

Reversing the polarity of charge-collecting electrodes in inverted PSC can be achieved by adopting appropriate electron-transporting and hole-transporting materials between the ITO/BHJ and BHJ/Metal interfaces, respectively. Efficient interfacial materials should possess several desired physical, chemical, and electronic properties including (1) appropriate energy level matching between the electrodes and active layer to facilitate unipolar charge extraction to the corresponding electrode; (2) high conductivities to minimize the Ohmic loss from series resistance; (3) high solvent resistance to facilitate multilayer film deposition from solutions; (4) low optical absorption to maximize the number of photons reaching the active layer; and (5) chemically inert to prevent interfacial reactions with electrodes for achieving long-term stability. Several classes of materials had been explored as possible electron selective materials for inverted PSCs. The most widely studied ones are n-type inorganic metal oxides including titanium oxide[18] and zinc oxide.[19, 20] Despite their good electron selective properties, the sensitivity of their electrical properties to the surface adsorption of oxygen and UV-irradiation may complicate the use of these materials in PSCs.[21-23] Modifications of the metal oxide surface using fullerene-based self-assembled monolayers[24, 25] or thin films[26] had been demonstrated as an

efficient strategy to further improve the interfacial properties between metal oxide and BHJ film. These have resulted in enhanced device efficiency and stability. Ultra-thin insulating aluminum oxide[27] and cesium oxide obtained through thermal decomposition of cesium salt[28] have also been used to modify the ITO work functions to facilitate electron collection in inverted cells.

Although a large number of studies have been performed on n-type inorganic interfacial materials, only few attempts have been made on polymer or small molecule based n-type interfacial materials for inverted PSCs even though they have great advantages compared to inorganic materials, such as the versatility of tuning their optical, electrical, and physical properties through organic synthesis. In addition, polymeric materials are intrinsically more flexible, making them a better option for plastic solar cells that are bendable and rugged.

One of the limiting factors for directly using conjugated polymers or small molecules as interfacial materials in OPV devices is their relatively low conductivities, which resulted in high series resistance and poor Ohmic contact with the electrodes.[29] As a result, improving the conductivity of interfacial transport layers through chemical doping is required for the realization of high performance solar cells. This strategy has been widely used in vacuum-evaporated small molecule-based solar cells in which the small molecule semiconductor and dopant can be co-deposited to achieve controllable and stable doping.[29] However, chemical doping in solution processed transport layer is more challenging. Unlike small molecule-based multilayer devices that can be fabricated by subsequent deposition through vacuum processes, polymer-based interfacial materials should possess good solvent resistance to prevent solvent-induced erosion during the multi-layer film deposition process. In addition, concurrent development of stable dopants that are compatible with solution process is necessary.

Thermal- or photo-crosslinkable charge-transporting materials had been demonstrated as efficient interfacial materials that provide adequate solvent resistance for the fabrication of polymer light-emitting diodes.[30] This class of material has also been employed as hole-transporting layers in OPV cells to improve the hole collection property.[31, 32, 33] Recently, cross-linkable fullerene materials were developed and employed as an n-type interfacial layer between ZnO and the active layer to enhance the electron collection property in inverted OPV cells.[26] However, without ZnO, fullerene is ineffective as a good electron-transporting material (ETM) in inverted PSCs because its low conductivity compared to metal oxides. Therefore, n-doping of fullerene is required to enhance the conductivity of the electron-transporting layer. n-Type doping has been studied in vacuum-deposited small molecule based solar cells in which the fullerene electron-transporting layer is doped with decamethylcobaltocene (DMC) to achieve significantly improved PCE compare to the undoped cells.[34] Crystallographic study of the fullerene complex with DMC reported by Konarev *et al*. showed that fullerene anion and DMC cation form a stable three-dimensional framework with solvent molecules.35 Because the solid-state ionization energy of DMC (3.3 eV) 34 is smaller than the LUMO of PCBM-S (~3.7eV), efficient n-doping of PCBM-S can be achieved through electron transfer from the HOMO of the dopant to the LUMO of the fullerene derivative.

The focus of the current study is to demonstrate improved device performance of inverted PSCs by incorporating robust fullerene side-chain polymers that are chemically doped with DMC to form an efficient electron-transporting interfacial layer. The fullerene polymer films produced by thermal polymerization on ITO substrates possess good solvent resistance. Chemical n-doping of fullerene polymers with DMC is shown to significantly enhance the PCE. The improved device performance is attributed to the decreased series resistance and efficient

electron extraction via the n-doped PCBM-S polymer films. We also investigate n-channel organic thin-film transistors (OTFTs) using n-doped fullerene polymers to characterize the effect of doping on the electrical properties of the PCBM-S.

2.2 RESULTS AND DISCUSSION

2.1.1 Synthesis and characterization

We have designed PCBM-S to match several requirements as follows. First, the monomer (PCBM-S) should be easily polymerizable in solid state. Second, the size of the reactive units should be as small as possible to maintain reasonable electron mobility of the polymer. Finally, the polymer film should be insoluble in common organic solvents to allow multilayer solution-processing and the resulting polymer film also need to have good morphological stability during device processing.

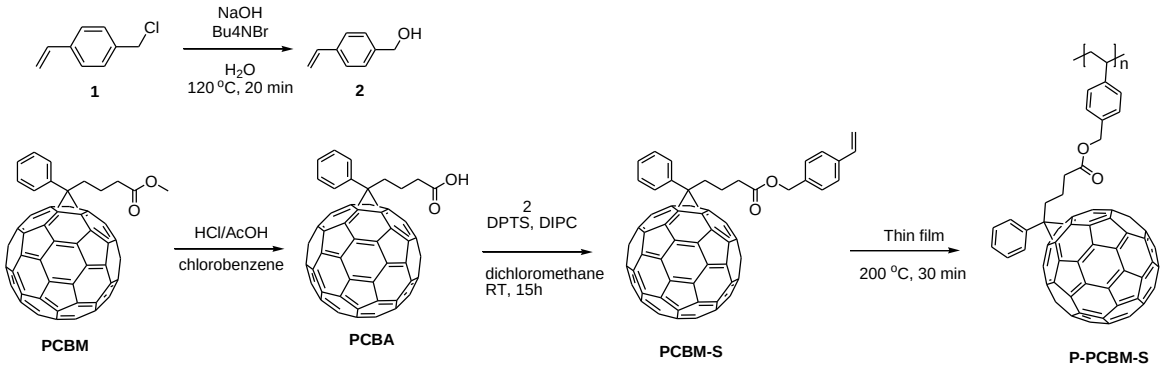

Figure 2.1 Synthetic route of fullerene polymer

The PCBM-S was synthesized by the esterification of [6,6]-phenyl-C_{61}-butyric acid (PCBA) with 4-vinyl benzyl alcohol (2), as shown in Figure 2.1. The PCBM-S was characterized by NMR spectroscopy and elemental analysis.

2.1.2 Thermal properties

The thermal properties of PCBM-S were studied by DSC. As shown in Figure 1, PCBM-S exhibited a glass-transition temperature (T_g) of 114 ℃. After annealing above T_g, the PCBM-S showed exothermic peaks at 170 ℃ and 230 ℃, which are believed to be the thermal polymerization of styrene linkage.[38] In the second scan, these peaks are no longer detectable. This implies that long-range molecular motion of the polymerized PCBM-S (P-PCBM-S) is significantly limited after thermal polymerization and therefore, we expect that the polymer film should have good morphological stability.

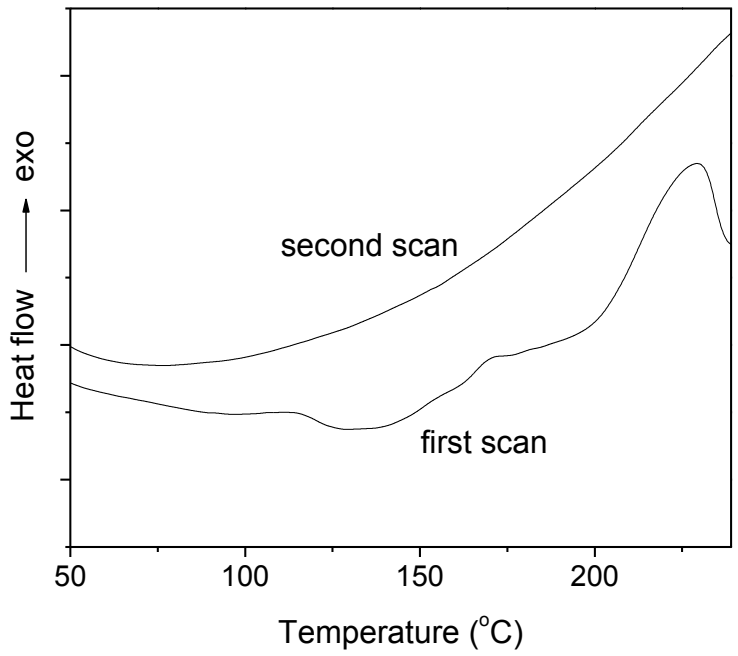

Figure 2.2 DSC thermograms of the PCBM-S with a heating rate of 10 ℃/min.

2.1.3 Absorption properties

Figure 2.3 shows the UV-Vis-NIR absorption spectra of the thin films of undoped and 6 wt% DMC doped PCBM-S on glass substrate measured before and after washing with chlorobenzene. All films were prepared by spin-coating, then polymerized by thermal annealing at 200 ℃ for 30 min under inert conditions. The small decrease in the absorption intensities observed for both undoped and 6 wt% DMC doped P-PCBM-S films after rinsing with chlorobenzene demonstrates effective solvent resistance of the films.

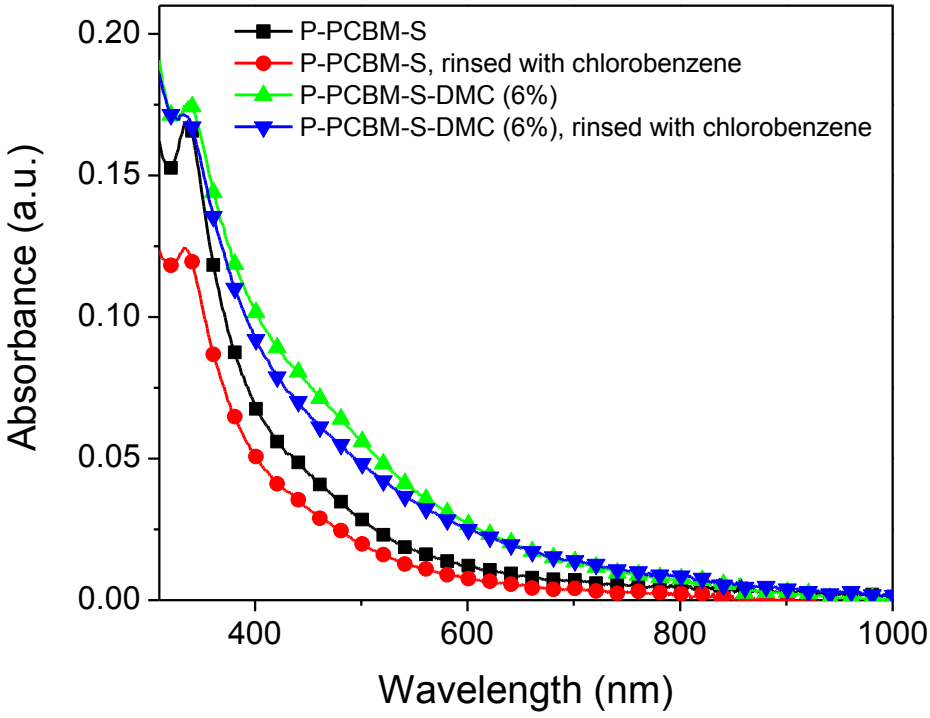

Figure 2.3 Absorption spectra of the undoped and DMC doped P-PCBM-S polymer films on glass substrate before and after washing with chlorobenzene.

2.1.4 Photovoltaic Properties

Figure 2.4 shows the *J-V* characteristics of inverted polymer solar cells with and without modification of ETM. Devices of architecture ITO/ETM/P3HT:PCBM/ PEDOT:PSS

/Ag were tested under simulated AM 1.5G illumination at 100 mW/cm^2. The results show clear evolution of *J-V* curves as a function of the doping concentration of DMC in P-PCBM-S films. A summary of the photovoltaic parameters for the devices is given in Table 2.1. Note that the PCE increases significantly from 1.24% to 2.53% with an increase in dopant (DMC) concentration from 0 to 10 wt%. The best performance was obtained from devices with 10 wt% doped PCBM-S. These improvements are attributed from the enhanced electrical conductivity and improved electron extraction efficiency of P-PCBM-S as a result of increased doping level. As shown in Table 2.1, the enhanced conductivity of the P-PCBM-S causes an overall decrease in series resistance (R_s) from 1110 Ω cm^2 for undoped P-PCBM-S

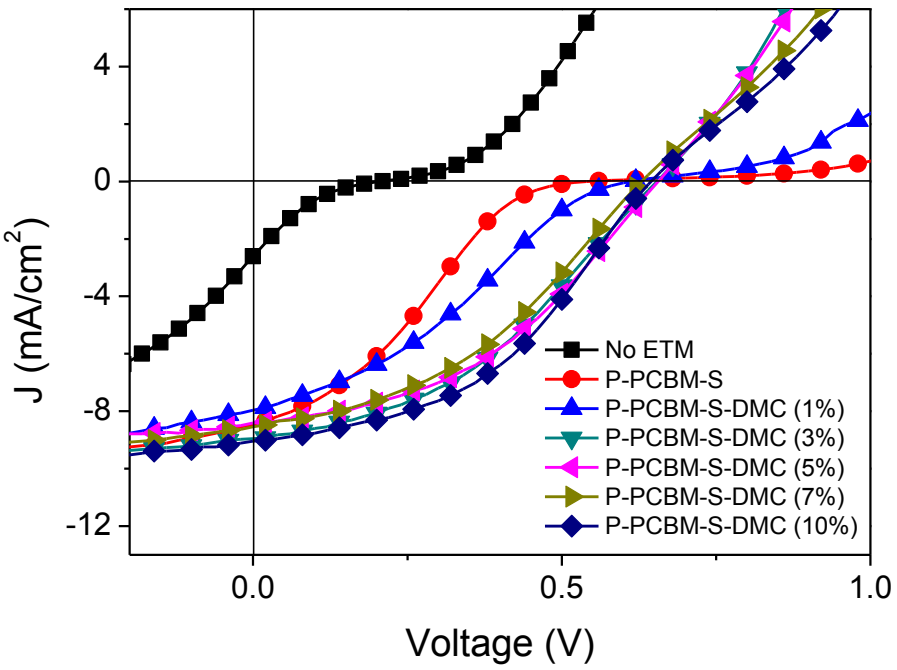

Figure 2.4 *J-V* curves of inverted polymer solar cells as a function of the doping concentration of DMC in P-PCBM-S films.

to 50 Ω cm^2 for 10 wt% doped P-PCBM-S, as well as increase in fill factor (FF) from 0.27 to 0.44. There is also a pronounced enhancement in J_{sc}, V_{oc}, FF, and thus PCE for 3 wt% and 5 wt% doped P-PCBM-S relative to the undoped device. Since there is no significant increase in PCE of the 10 wt% doped device compared to the 3-5 wt% doped device, we suggest that 3-5 wt% is an effective doping concentration for present experiments.

Table 2.1 Summary of device performance with various ETMs.

ETM	PCE (%)	V_{oc} (V)	J_{sc} (mA/cm^2)	FF	R_s ($\Omega \cdot cm^2$)
No ETM	0.08	0.21	2.60	0.21	315
P-PCBM-S	1.24	0.54	8.47	0.27	1110
P-PCBM-S-DMC (1%)	1.46	0.61	7.95	0.31	350
P-PCBM-S-DMC (3%)	2.33	0.65	8.96	0.40	40
P-PCBM-S-DMC (5%)	2.32	0.66	8.42	0.42	40
P-PCBM-S-DMC (7%)	2.16	0.63	8.53	0.40	50
P-PCBM-S-DMC (10%)	2.53	0.64	9.06	0.44	50

2.1.5 Morphology

For PSC applications, good film quality without pinholes or aggregates is essential since it plays a crucial role in the lifetime and efficiencies of solar cell devices. To investigate how the morphology of the P-PCBM-S film affects the device performance, we studied the surface morphology of n-doped P-PCBM-S films prepared under different spincoating conditions and evaluated the corresponding device performance. Devices based

on 3 wt% DMC doped P-PCBM-S films spin-coated by 7000 rpm shows almost same device performance (*PCE*: 2.30%, V_{oc}: 0.65 V, J_{sc}: 8.90 mA/cm^2; *FF*: 0.41) with the devices spin-coated by 4000 rpm (*PCE*: 2.33%, V_{oc}: 0.65 V, J_{sc}: 8.96 mA/cm^2, *FF*: 0.40).

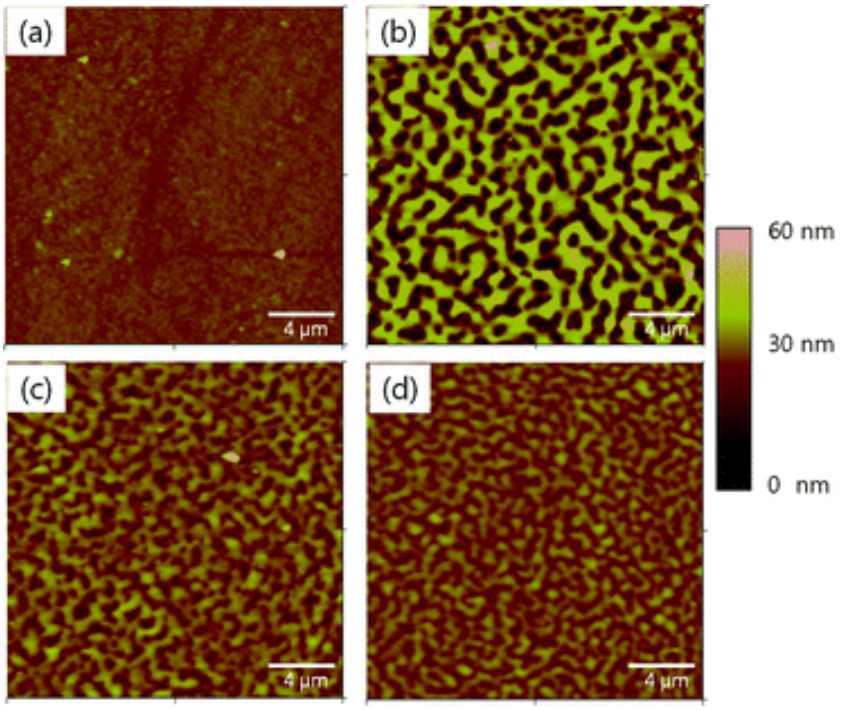

Figure 2.5 AFM images of P-PCBM-S (a), 3% DMC doped P-PCBM-S casted by different spin speeds: 2000 rpm (b), 4000 rpm (c), and 7000 rpm (d).

However, decreasing the spin speed to 2000 rpm results in shorting of devices. This shorting results from the poor morphology that originates from dewetting between the P-PCBM-S layer and ITO. The significant morphological differences of n-doped P-PCBM-S films as a function of the spin speed were investigated by AFM (Figure 2.5). The DMC doped P-PCBM-S films spin-coated by 2000 rpm has a very rough surface (9.7 rms) due to dewetting, whereas the films spin-coated by the speed of 4000 and 7000 rpm give relatively smooth surfaces (4.0 rms and 2.7 rms, respectively). There are two plausible mechanisms that could

explain the dewetting of the film spin-coated at the speed of 2000 rpm. One is that the surface energy of the P-PCBM-S film could be significantly changed by DMC compared to the undoped P-PCBM-S film. Compared to doped P-PCBM-S films, undoped P-PCBM-S films on ITO shows low surface roughness (1-1.5 rms) regardless of the spin speeds. Another reason for the morphological difference from different spin speed is that the faster solvent evporation rate at higher spin speed may alter the drying kinetics of the film, which resulted in smoother film by surpressing the dewetting property.[39]

2.1.6 Organic Field-Effect Transistors

The electrical conductivity of the charge transport materials used in polymer solar cells is an important factor that governs the performance of the devices. Thus, we further investigated the electron-transporting properties of n-doped P-PCBM-S via the fabrication of n-type OTFTs. The 1, 3, 5, 7 and 10 wt% of DMC doped PCBM-S solutions were prepared by the same method used for fabricating solar cells. The n-doped PCBM-S solutions were spin-coated onto a heavily doped $n^{++}Si$ wafer with a 200 nm-thick SiO_2 layer with a top contact geometry and Au was used as the source and drain electrodes.

With increasing the doping concentration from 0 to 3% in P-PCBM-S films, the OTFTs devices showed well known doping effects such as negative shift of threshold voltages and decrease of on-off ratio as shown in Figure 2.6 (a) and Table 2.2.[40] The device with undoped P-PCBM-S shows field-dependent transfer characteristics, whereas the devices with highly doped (5-10 wt%) P-PCBM-S exhibit field-independent properties with small I_{on}/I_{off} ratio of <10, which is a characteristic of conducting materials. In addition, Figure 2.6 (b) clearly shows that the output current of devices at zero gate bias condition increased upon increasing the amount of dopant, indicating that the doping concentration directly affect the amount of

charge carriers and is responsible for the increased electrical conductivity of the doped P-PCBM-S films.

(a)

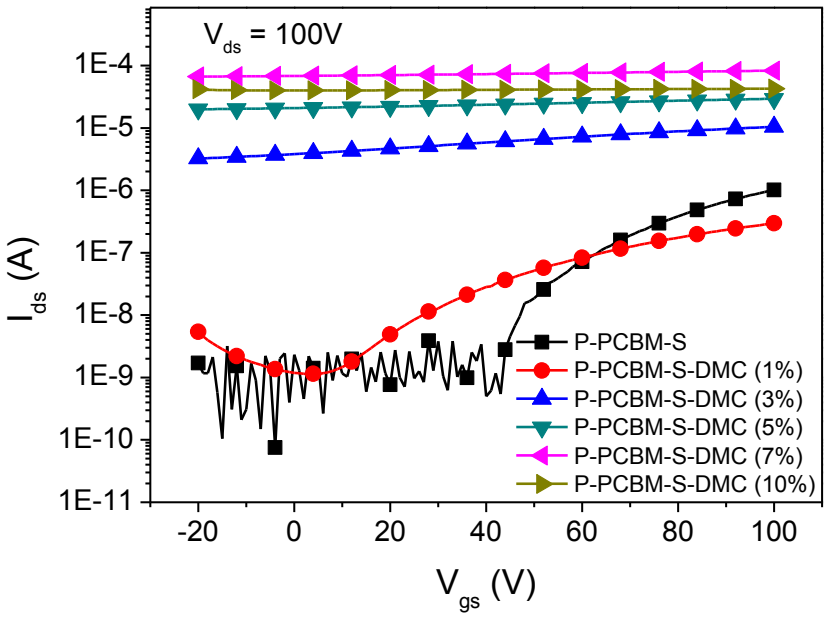

(b)

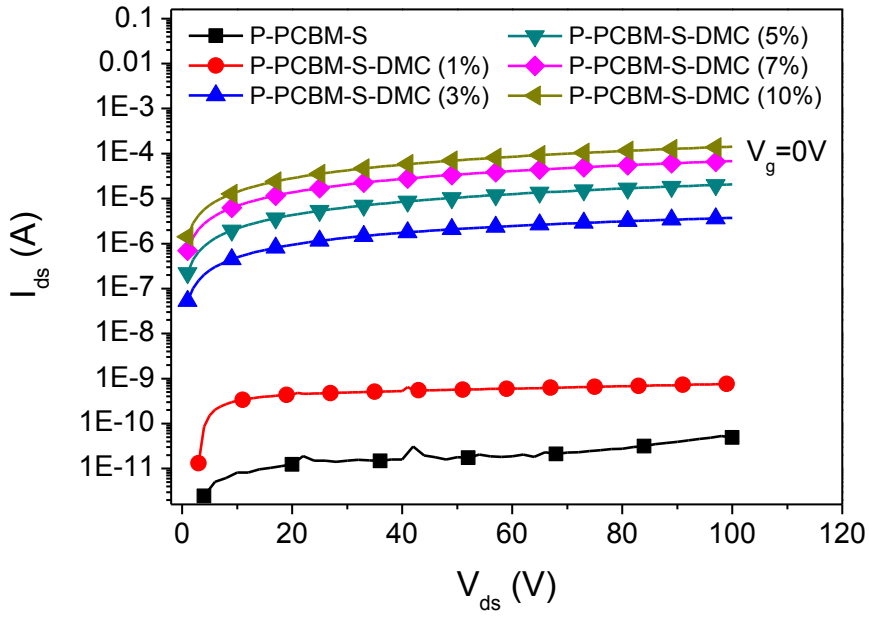

Figure 2.6 (a) Transfer characteristics of OTFTs with undoped and DMC doped P-PCBM-S as active layers at varying doping concentrations. (b) Output curves at zero gate voltages for the same devices.

Table 2.2 OTFT electrical properties for undoped and DMC doped P-PCBM-S transistors at different doping concentrations measured in the N_2-filled glovebox.

ETM	μ ($cm^2/V \cdot s$)	I_{on}/I_{off}	V_t(V)	σ (S/m)
P-PCBM-S	1.45×10^{-4}	10^3	42.0	1.65×10^{-7}
P-PCBM-S-DMC (1%)	1.35×10^{-5}	10^2	6.8	1.53×10^{-6}
P-PCBM-S-DMC (3%)	2.76×10^{-5}	10	-20.2	1.43×10^{-2}
P-PCBM-S-DMC (5%)	-	<10	-	8.54×10^{-2}
P-PCBM-S-DMC (7%)	-	<10	-	2.84×10^{-1}
P-PCBM-S-DMC (10%)	-	<10	-	5.96×10^{-1}

The conductivity of the films was derived from gated two-terminal measurements and the conductivity can be calculated from the equation of $\sigma(V_g) = (L/A)(I_d/V_d)$, where L and A are channel length and cross-sectional area of the device, respectively. The conductivities calculated from the slope of V_d-I_d curves at zero gate voltage are were summarized in Table 2.2. There is a pronounced enhancement in conductivity of 1.65×10^{-7} S/cm for undoped P-PCBM-S to 5.96×10^{-1} S/cm for 10 wt% doped P-PCBM-S. These values are comparable with previously reported results.[40] Moreover, the overall trend of increased output current with doping concentration is well matched with the decrease of series resistance in the solar cells (Table 2.1). For example, there are significant improvements in both output current of OTFT devices and series resistance of solar cell devices from 1% doped P-PCBM-S to 3% doped P-PCBM-S. However, they are saturated after 3% of doping concentration. In particular, the annealed device with 10% of DMC in P-PCBM-S shown in Figure 2.6 (b) had more than 6 orders of magnitude higher drain current than that of the device with undoped P-PCBM-S. The systematic transition of device characteristics including threshold voltage (V_t), conductivity, and on-off current ratio (I_{on}/I_{off}) as a function of the doping concentration are

obvious and it further elucidates the relationship between the electrical properties of the n-doped P-PCBM-S layers and the device performance of solar cells.

2.2 CONCLUSION

A new thermally polymerizabled fullerene derivative has been synthesized to explore the use as an interfacial electron-transporting material for inverted polymer solar cells. The key advantage of this fullerene polymer (P-PCBM-S) is that it enables multi-layer solution processing and facilitates cascade electron transport for efficient electron collection in PSCs. It was demonstrated that chemical n-doping of P-PCBM-S almost double the power conversion efficiency of inverted devices. The improved device performance is attributed to the decreased series resistance and efficient electron extraction from the active layer through the n-doped P-PCBM-S interfacial layer.

2.3 EXPERIMENTAL

Materials Synthesis: All chemicals were purchased from Aldrich Chemical Corporation unless otherwise specified. Regio-regular poly(3-hexylthiophene) (P3HT) and PCBM were purchased from Rieke Metals, Inc. and American Dye Source, Inc, respectively, and was used as received. 4-vinylbenzyl alcohol (2) and PCBA were synthesized according to literature methods.[36, 37]

Synthesis of PCBM-S: A solution of PCBA (40 mg, 0.045 mmol), 4-vinylbenzyl alcohol (8.97mg, 0.067 mmol) and 4-dimethylaminopyrindine-4-toluenesulfonate (19.67 mg, 0.067 mmol) in dichloromethane (30 mL) in a round bottom flask was stirred for 5 min at room temperature. After 5 min, 1,3-diisopropyl carbodiimide (28.14 mg, 0.225 mmol) was added and the solution was allowed to stir for 12 hours. The coupling reaction was monitored by thin-layer

chromatography. After removal of solvent, the crude product was purified by column chromatography using toluene/hexane (1:1, v/v). The PCBM-S was collected by filtration and washed with methanol to give a brown solid (20 mg, 55 % yield).^{1}H NMR (300 MHz, $CDCl_3$, 25℃, TMS) : δ= 2.19 (m, 2H), 2.59 (t, 2H), 2.93 (m, 2H), 5.12 (s, 2 H), 5.32 (d, J = 16.8, 1H), 5.80 (d, J = 18.3, 1H), 6.68 (q, J=10.8, 1H), 7.28-7.59 (m, 7 H), 7.93(d, J = 4.8, 2 H); ^{13}C NMR (125 MHz, $CDCl_3$, 25℃, TMS) : δ= 22.4, 33.7, 34.1, 51.9, 66.2, 79.9, 114.4, 128.3,128.5, 128.6, 132.1, 135.3, 136.3, 137.6, 138.1, 140.8, 141.0, 142.1, 142.2, 142.2, 142.3, 142.9, 143.0, 143.1, 143.8, 144.0, 144.4, 144.5, 144.7, 144.8, 145.1, 145.1, 145.2, 145.9, 147.8, 148.8. Anal. Calcd for $C_{80}H_{20}$: C, 94.85, H, 1.99. Found: C, 93.28, H, 1.48.

Absorption, thermal property and morphology Measurements: A Perkin-Elmer Lambda-9 spectrophotometer was used to measure UV-Vis spectra. The thermal property was studied using differential scanning calorimetry (DSC) (DSC2010,TA instruments) under a heating rate of 10 ℃/min and a nitrogen flow of 50 mL/min. The surface morphology of the polymer films were studied using the tapping mode atomic force microscopy (AFM) from Veeco a Nanoscope III controller.

Fabrication and Characterization of Solar Cells: To fabricate the inverted solar cells, ITO-coated glass substrates (15 Ω/□) were cleaned in sequential ultrasonic baths of detergent water, de-ionized water, acetone, and isopropyl alcohol. Substrates were then treated with oxygen plasma for 5 min. A thin layer of PCBM-S was prepared by spin-coating of the PCBM-S solution (5 mg/ml of PCBM-S in chloroform with different mount of DMC) and then annealed at 200 ℃ for 30 min in the glove box. Afterward, PCBM (American Dye Source, Inc., 99.0% purity) and P3HT (Rieke Metals, Inc., 4002-E grade) (0.7:1 weight ratio) in a chlorobenzene solution (60 mg/ml) was spin-coated on the PCBM-S layer in a glove box and annealed at 160

℃ for 10 min to get a active layer with thickness of ca. 200 nm. After annealing, a PEDOT:PSS solution (H. C. Starck, Clevios 4083) was spin-coated onto the active layer to get a layer with 50 nm thickness.[24] These samples were annealed for 10 min at 120 ℃ on a hot plate. A metal electrode (Ag) was then vacuum-deposited at a base pressure of 2×10^{-6} torr at a rate of 2 Å/s. The *J–V* characteristics of the solar cells were tested under ambient conditions using a Keithley 2400 SMU and an Oriel xenon lamp (450 W) with an AM1.5 filter. The device illumination area of 0.0314 cm^2 was defined by using a physical mask to minimize photocurrent generation from the edge of the electrodes. The light intensity was calibrated to 100 mW/cm^2 using a calibrated silicon solar cell with a KG5 filter, which is traced to the National Renewable Energy Laboratory. The performance of the devices was averaged over at least 5 devices for each processed condition.

Fabrication and Characterization of OTFTs: Heavily n-doped silicon substrates with a 300 nm-thick thermally grown SiO_2 dielectric (from Montco Silicon Technologies, Inc.) was used to fabricate top contact OTFTs. The substrates were treated with HMDS by vapor phase deposition in a vacuum oven (200 mTorr, 100℃, 2 hours) before spin-coating of PCBM-S. The undoped and doped PCBM-S films were spin-coated in the glove box. The 1 wt% of PCBM-S in chloroform was used to obtain a film thickness of 50 nm. Interdigitated source and drain electrodes (W=9000 μm, L=90 μm, W/L=100) were defined by evaporating a 100 nm Au at 10^{-6} Torr. An Agilent 4155B semiconductor parameter S6 analyzer was used to characterize OTFT properties.. The electron mobility was calculated in the saturation regime from the linear fit of $(I_{ds})^{1/2}$ *vs* V_{gs}. The V_t was obtained as the x intercept of the linear section of the plot of $(I_{ds})^{1/2}$ *vs* V_{gs}.

Chapter 3. IN SITU CROSSLINKING AND N-DOPING OF SEMICONDUCTING POLYMERS AND THEIR APPLICATION AS EFFICIENT ELECTRON TRANSPORTING MATERIALS IN INVERTED POLYMER SOLAR CELLS

3.1 INTRODUCTION

Bulk-heterojunction polymer solar cells (PSCs) have attracted considerable attention as a promising candidate for inexpensive and flexible solar cells.[36-38] The performance of PSCs is mainly dependent on the electrical and optical properties of donor polymers[6-9] and fullerene acceptors[10, 11]in the bulk-heterojunction (BHJ) active layer and interface engineering using electron- and hole-transporting materials (ETMs and HTMs). By virtue of extensive studies on novel active and interfacial materials, the power conversion efficiencies (PCE) of PSCs with conventional architecture (ITO/HTM/BHJ active layer/metal cathode stacks) have already surpassed 7%.[39, 40] However, to improve the economic viability of PSCs, their long-term stability and efficiency need to be further improved. The degradation of device performance for PSCs with conventional architectures is mainly due to the fact that the low work-function metal top electrode such as Ca and Al can be easily oxidized.[12] To overcome this problem, PSCs with an inverted structure (ITO/ETM/BHJ active layer/HTM/metal anode stacks) have been developed. The inverted architecture enables the use of an air-stable high work-function metal such as Ag or Cu because the polarity of the device is reversed by the adoption of appropriate interfacial materials (ETMs and HTMs).[13, 14] Therefore, interfacial materials are one of the key elements for efficient inverted PSCs.[15]

Efficient electron selective materials should fulfill several requirements with regards to their electrical, chemical, and physical properties such as: i) appropriate highest occupied molecular orbital (HOMO) and lowest unoccupied molecular orbital (LUMO) levels for efficient electron extraction and hole blocking properties, ii) solvent resistance to prevent solvent-induced erosion during multilayer solution processing, iii) sufficient conductivity to decrease series resistance and improve the fill factor (FF), iv) low extinction coefficient at visible wavelengths to minimize

optical losses, and v) smooth film morphology and good adhesion with both indium tin oxide (ITO) and the active layer.

Inorganic metal oxides such as TiO_x and ZnO have been intensively investigated as ETMs in inverted PSCs because of their appropriate energy levels for selective extraction of electrons and blocking holes from the BHJ. Moreover, these materials have sufficient conductivity, and are transparent to visible light. However, their photoconductivity can be significantly altered by the adsorption of oxygen upon illumination of light,[41-43] which can decrease the stability of the device.[44] Fullerene-based self-assembled monolayers[45, 46] or crosslinkable fullerenes[47] have been used to modify the metal oxide surface to further improve of the interfacial properties between the metal oxide and BHJ films, resulting in enhanced device efficiency and stability.

Compared to their inorganic counterparts, organic-based semiconductors have more promise as interface materials for polymer solar cells due to the feasibility of tuning their opto-electrical and physical properties through molecular design and organic synthesis. In addition, polymeric materials are more suitable for flexible PSCs because of their intrinsic mechanical robustness. However, there has been limited application of organic-based electron selective interface materials in PSCs due to the lack of materials with appropriate solvent resistance for solution processed multilayer devices.[48, 49]

To develop efficient organic-based ETMs, two major issues need to be simultaneously addressed. First, they have relatively low inherent conductivities and form a poor electrical contact with the electrodes compared to metal oxide-based ETMs.[50] Thus, increasing the conductivity of interfacial materials by chemical n-doping is necessary to achieve efficient PSCs. This method has been extensively employed to improve vacuum-deposited small molecular organic solar cells.[51-56] However, n-doping of polymers is more challenging since there are few

dopants that are both stable and suitable for solution processing.[26, 32-35] Recently, Wei *et al*. reported (4-(1,3-dimethyl-2,3-dihydro-1*H*-benzoimidazol-2-yl)phenyl)dimethylamine (N-DMBI) as an efficient organic n-dopant which has good solubility in common organic solvents.[57] The conductivities of N-DMBI doped PCBM films reached up to ~2×10^{-3} S/cm, showing that N-DMBI can be an efficient n-dopant. Interestingly, OFET devices with N-DMBI doped PCBM films show improved air stability compared to undoped devices.

The second major limiting factor for using organic semiconductors as interface materials is their poor solvent resistance to prevent solvent-induced erosion during the fabrication of solution-processed multilayer devices. To circumvent this problem, thermally cross-linkable small molecule organic semiconductors have been introduced as interfacial layers to provide suitable solvent resistant films to fabricate both organic light-emitting diodes[58] and PSCs.[59, 60] Recently, Png *et al*. reported an alternative crosslinking method using bis(perfluorophenyl) azide (bisPFPA) crosslinker to produce crosslinked semiconducting polymer films.[61] The active singlet nitrenes produced by the UV-induced photolysis of the azide moiety can react with the alkyl side chains of the polymers with high photocrosslinking efficiency. In addtion, this selective crosslinking chemistry can minimize the resultant effects on the electrical properties of the semiconducting polymers since the conjugated backbone is not involved in the crosslinking reaction.

Here, we demonstrate an *in-situ* process of n-doping and crosslinking of n-type semiconducting polymers to make highly conductive and solvent resistant ETMs for inverted PSCs. Thiophene and naphthalene diimide (NDI) copolymers were used as an ETM (Figure 3.1). These polymers were crosslinked with bisPFPA and the resultant films possess good solvent resistance. Concurrently, the NDI copolymers were chemically n-doped with various doping

ratios of N-DMBI, which substantially improved the PCE from 0.69% to 3.42%. We also fabricated organic thin film transistor (OTFT) devices to investigate the impact of n-doping on the electrical conductivities of NDI copolymers and to correlate these conductivities with the subsequent PSC performance.

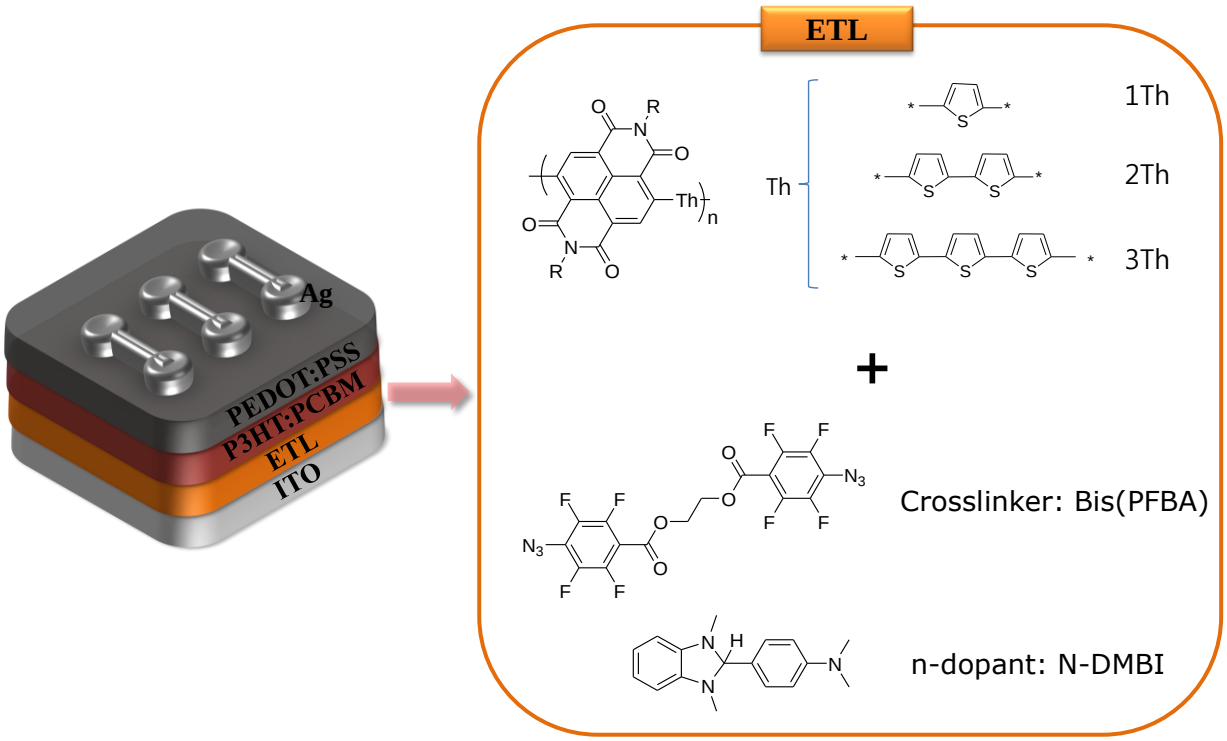

Figure 3.1 The structure of inverted PCSs and materials used for in situ crosslinked and doped ETMs.

3.2 Results and Discussion

3.2.1 *Film properties of NDI copolymers*

Thiophene-NDI copolymers were chosen because they have been proven to be good n-type semiconductorsfor organic thin film transistors (OTFT).[62-64] The synthesis and the electrical properties of the NDI copolymers used in this study (PNDI-1Th, PNDI-2Th, andPNDI-3Th) were reported elsewhere.[65] The bisPFPA and N-DMBI were synthesized according to previously reported methods.[66, 67] To prepare the *in-situ* crosslinked and n-doped NDI copolymer films, N-

DMBI, bisPFPA, and the NDI copolymers were co-dissolved in chlorobenzene. The amount of crosslinkers (bisPFPA) was fixed to be 10 wt% relative to the polymers for all devices. The doping concentration was varied from 0 to 15 wt% relative to the polymers. The film quality of ETMs is important because it can markedly affect the lifetime and PCE of PSCs. Optical microscope images of photo-crosslinked PNDI-1Th containing 15wt% of dopant (hereafter referred to as x-PNDI-1Th (15%)) illustrate photo-patterned structures (Figure 3.2a). The film was covered with a photomask and exposed to deep UV light (λ = 254 nm) for 5 min at room temperature for photo-patterning and then washed with chlorobenzene.

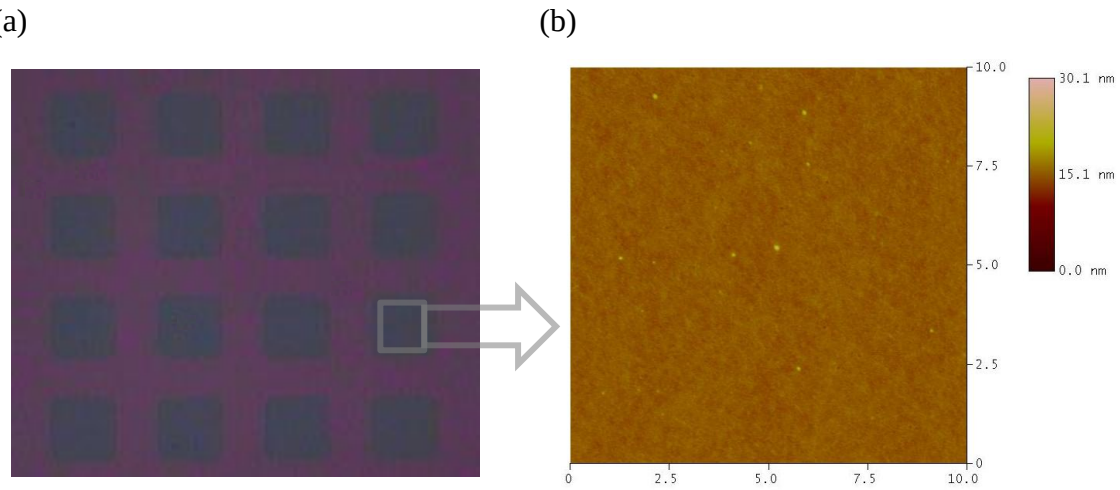

Figure 3.2 Optical microscope image of photo-patterned x-PNDI-1Th (15%). The size of patterned structure is 70×70 μm. Inset: the same images with smaller magnification. (b) AFM image of the x-PNDI-1Th (15%) measured from the photo-patterned area.

The photo-patterning experiment reveals that the PNDI-1Th (15%) was efficiently and homogeneously crosslinked by UV illumination and the crosslinking occurs only in the exposed area with clear edges. Figure 3.2b shows the AFM image of the photo-patterned area. The crosslinked film shows a smooth surface and no phase segregation.

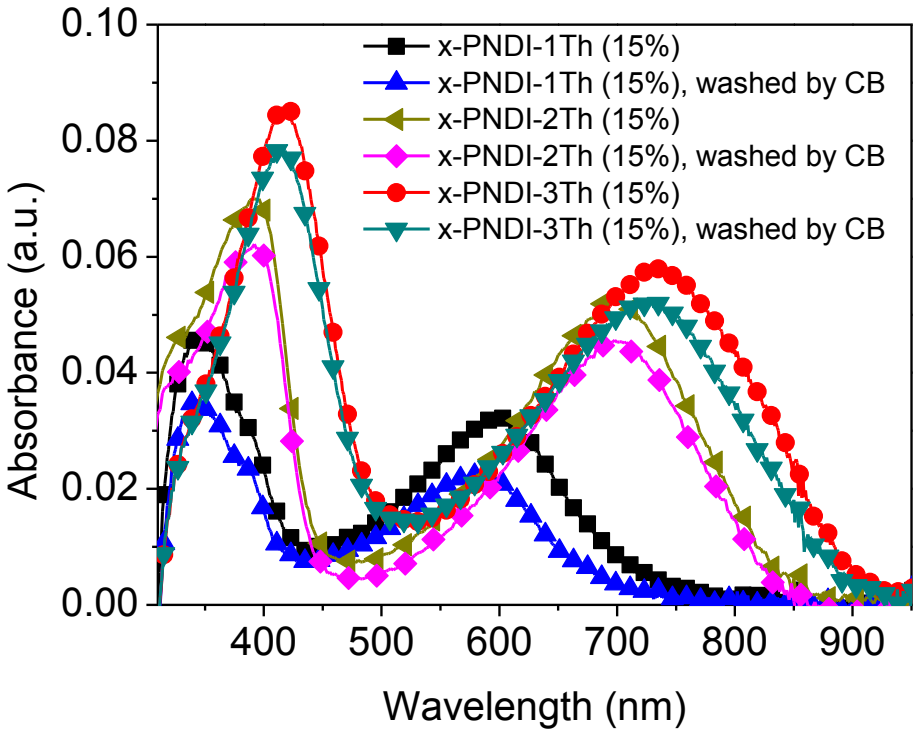

Figure 3.3 Absorption spectra of x-PNDI-1Th (15%), x-PNDI-2Th (15%) and x-PNDI-3Th (15%) films on glass substrate before and after washing with chlorobenzene (CB).

Figure 3.3 shows the UV-Vis-NIR absorption spectra of the thin films of x-PNDI-1Th (15%), x-PNDI-2Th (15%) and x-PNDI-3Th (15%) films on glass substrate measured before and after washing with chlorobenzene.After washing with chlorobenzene, there are only small reduction in the absorption intensities, which shows that all crosslinked polymer films have effective solvent resistance.

3.2.2 *Solar cell performances*

Inverted PSCs were fabricated with ITO/ETM/P3HT:$PC_{61}BM$/PEDOT:PSS/Ag stacks and tested under simulated AM 1.5G illumination at 100 mW/cm^2. Three different NDI copolymers, which were crosslinked *in-situ* and n-doped from 0 to 15%, were used as ETMs. The thickness of

the ETM films was optimized to reduce series resistance (R_s) and light absorption, while sustaining good electron-transporting properties. A ZnO ETM was used as a control to compare with the NDI copolymers. The performance of the devices is shown in Figure 3.4 and the photovoltaic parameters are summarized in Table 3.1.

All devices with undoped NDI copolymers exhibit an s-shape kink in the current density-voltage (*J-V*) curves (Figure 3.4b, 3.4c, and 3.4d). Upon increasing the doping concentration in the crosslinked films, devices show a progressive evolution of diode behavior in the *J-V* curves with improved J_{sc}, V_{oc}, *FF,* and *PCE*. For example, the *PCE* of the device with PNDI-1Th significantly increases from 0.69% to 3.42% with an increase in doping concentration from 0 to 15wt% (Figure 3.4b). The optimized device using n-doped PNDI-1Th showed even better performance than that of the control device using ZnO as ETM (*PCE*: 3.21%). PNDI-2Th and PNDI-3Th also showed the same trend of increasing *PCEs,* but the maximum *PCE* was obtained at 10wt% of doping concentration (Figure 3.4c and 3.4d). The *PCEs* of the devices with x-PNDI-2Th (10%) and x-PNDI-3Th (10%) were 3.24% and 3.17%, respectively (Table 3.1).

The overall improvement in device efficiency is attributed to the increase in the electrical conductivity and improved electron extraction efficiency of NDI copolymers as a result of increased levels of doping. It is noteworthy that in all devices, J_{sc} and V_{oc} were largely improved by increasing doping concentrations from 0 to 5 wt% and generally plateaued above 5 wt%. The enhanced conductivity of the polymers also results in an overall decrease in series resistance (R_s), as well as an increase in FF. The calculated R_s value from the device with undoped x-PNDI-1Th is 64$\Omega \cdot cm^2$. By increasing doping concentration up to 15 wt%, R_s value decreases to 12 $\Omega \cdot cm^2$ (Table 3.1). The devices with x-PNDI-2Th and x-PNDI-3Th also showed the same trend of

decreasing R_s Values (Table 3.1). A more detailed study of the effect of doping on mobility and conductivity is reported in the OTFT section.

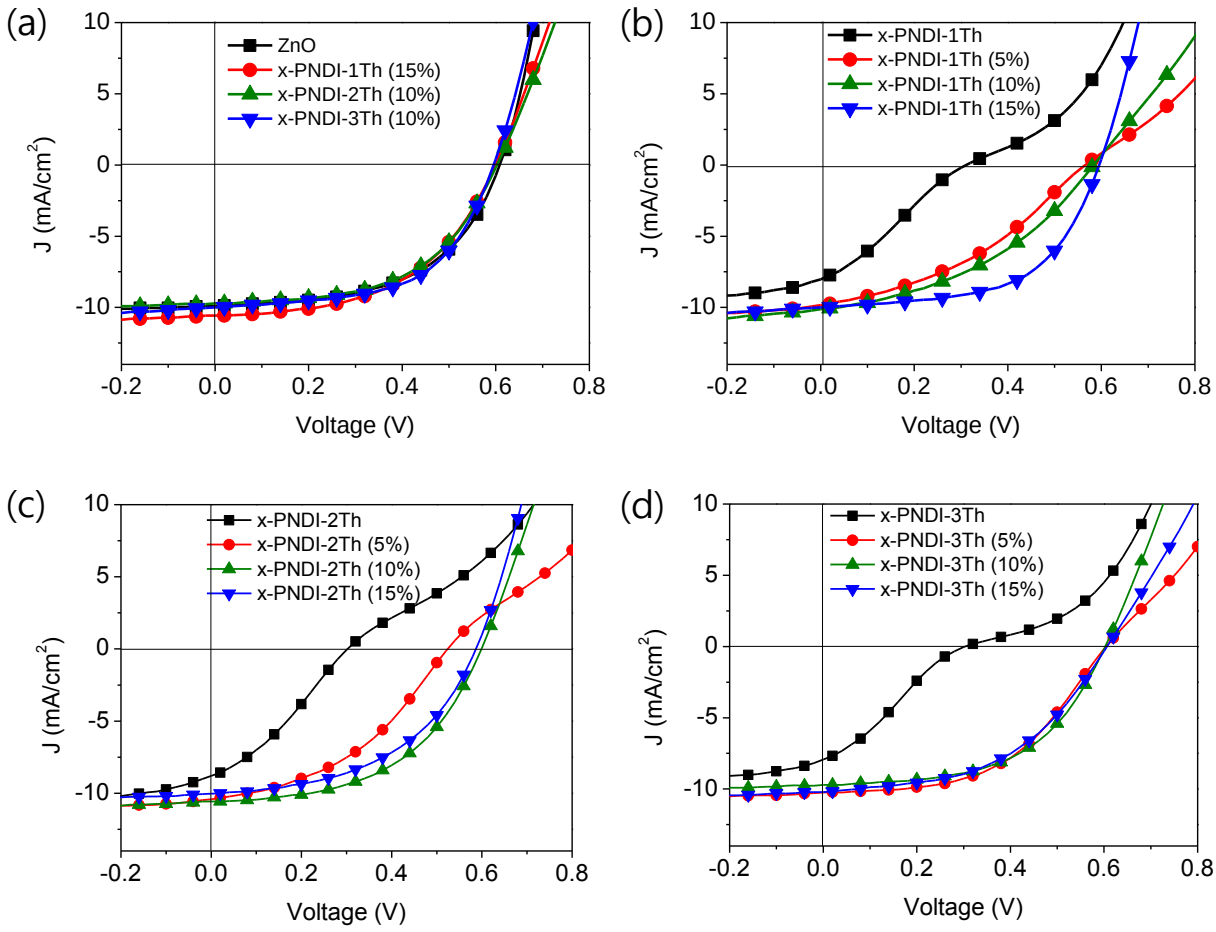

Figure 3.4 *J-V* characteristics of inverted PSCs for (a) ZnO and three different NDI copolymers with best doping levels showing maximum *PCE*s. Figure (b), (c), and (d) shows the evolution of *J-V*curves with a increase of doping concentration in x-PNDI-1Th, x-PNDI-2Th, and x-PNDI-3Th layers, respectively.

There is a small but nevertheless notable difference in *PCE* among the devices with three undoped polymers. The device with x-PNDI-2Th shows highest PCE (0.85%), while the devices with x-PNDI-1Th and x-PNDI-3Th exhibit lower PCE values (0.69 and 0.64%, respectively).

This data is compiled in Table 3.1. For undoped polymeric interfacial materials, there are two important factors governing device performance. One is the carrier mobility and the other is the HOMO and LUMO energy level of the polymers. As reported in previous publications, the electron mobilities of PNDI-1Th, PNDI-2Th and PNDI-3Th were 3.1×10^{-3}, 3.9×10^{-2} and 7.6×10^{-2} $cm^2/V \cdot s$.[68]

Table 3.1 Summary of device performance with ZnO and x-PNDI-1Th (0-15%), x-PNDI-2Th (0-15%) and x-PNDI-3Th (0-15%).

ETM	V_{oc} [V]	J_{sc} [mA/cm^2]	FF	PCE [%]	R_s [$\Omega \cdot cm^2$]
ZnO	0.61	9.97	0.53	3.21	8
x-PNDI-1Th	0.30	8.25	0.28	0.69	64
x-PNDI-1Th (5%)	0.57	10.30	0.36	2.10	41
x-PNDI-1Th (10%)	0.58	10.60	0.39	2.44	24
x-PNDI-1Th (15%)	0.59	10.00	0.58	3.42	12
x-PNDI-2Th	0.30	8.97	0.31	0.85	37
x-PNDI-2Th (5%)	0.52	10.40	0.42	2.29	29
x-PNDI-2Th (10%)	0.60	10.50	0.52	3.24	13
x-PNDI-2Th (15%)	0.59	10.40	0.47	2.89	13
x-PNDI-3Th	0.30	8.33	0.26	0.64	102
x-PNDI-3Th (5%)	0.60	10.40	0.49	3.10	27
x-PNDI-3Th (10%)	0.60	9.70	0.54	3.17	14
x-PNDI-3Th (15%)	0.60	9.60	0.52	3.00	20

The better *PCE* and higher J_{sc} for the device containing x-PNDI-2Th may originate from superior electron mobility compared to x-PNDI-1Th. Interestingly, the *PCE* of the device with PNDI-3Th is lower than that of x-PNDI-1Th and x-PNDI-2Th even though PNDI-3Th has the highest electron mobility. This is likely because of inappropriate energy level matching between PNDI-3Th and P3HT, that is, the HOMO level of PNDI-3Th (5.13 eV) is very close to the HOMO level of P3HT (5.10 eV).[44] Therefore, PNDI-3Th is unable to block holes leaked from the active layer. However, the HOMO levels of PNDI-1Th and PNDI-2Th are -5.62 and -5.30 eV, respectively, which are deeper than that of PNDI-3Th, thus, these materials should have a better hole-blocking ability. On the other hand, the LUMO levels of PNDI-1Th, PNDI-2Th and PNDI-3Th are -3.85, -3.79 and -3.76 eV, respectively.

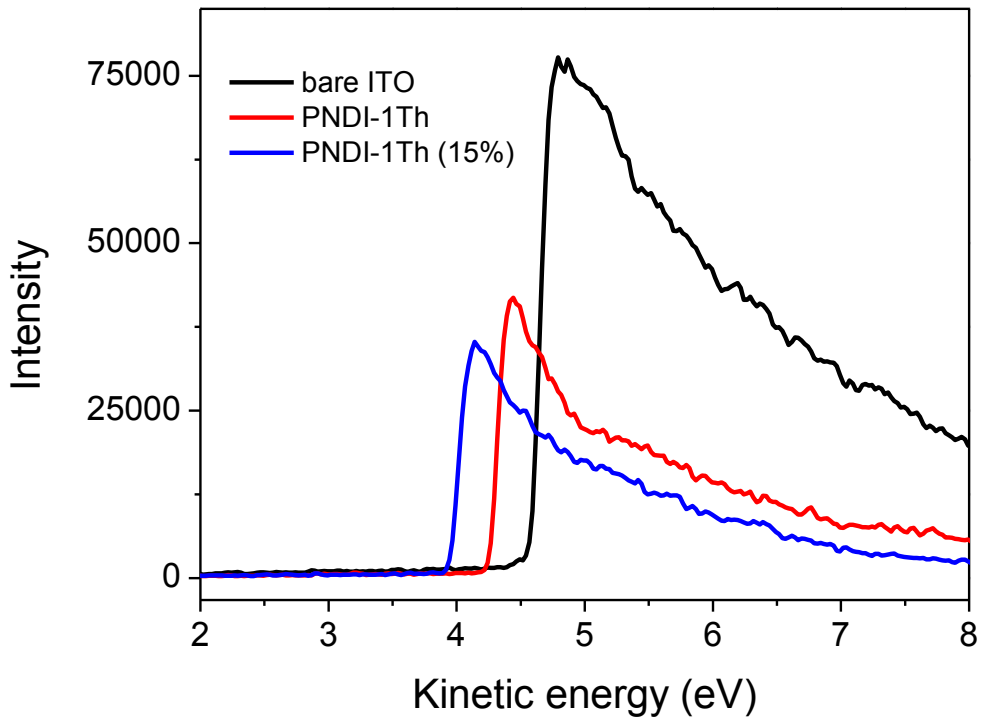

Figure 3.5 Secondary cutoffs of bare ITO, PNDI-1Th and PNDI-1Th (15%) films on ITO substrate measured by XPS.

These values are not significantly different and thus, efficient electron transport from PCBM to NDI copolymers can be achieved. In addition, it is important to understand the electronic structure of n-doped NDI-copolymers. The electronic structures of PNDI-1Th and PNDI-1Th (15%) were evaluated by means of the measurements of x-ray photoemission spectroscopy (XPS) (Figure 3.5).

Detailed experimental setup has been reported elsewhere.[47] PNDI-1Th and PNDI-1Th (15%) films on ITO substrates were prepared by the same method as described in solar cell fabrication. The work function of ITO calculated from the secondary electron cut-off was 4.55 eV and this value is well matched with the work function value of the ITO reported in the literature.[48] As shown in Figure 3.5, n-doping strongly reduces the work function of the PNDI-1Th from 4.20 to 3.91 eV. This work function shift means that the Fermi level position of the PNDI-1Th was shifted toward the LUMO level by increasing the number density of electrons through n-doping.

Compared to conventional PSCs, the main advantage of inverted PSCs is their improved air-stability. Recently, the Bao group reported that OFET devices with N-DMBI doped PCBM[49] and pyronin B doped perylene diimides[50] as active layers show exceptional device stability in ambient conditions. To examine the air stability of the devices with x-PNDI-1Th (15%), unencapsulated inverted PSCs were fabricated and device efficiency was measured after storage in air for 20 days. The device measured right after fabrication showed a *PCE* of 3.42% with V_{oc} of 0.59 V, J_{sc} of 10.0 $mAcm^{-2}$ and FF of 0.58 (Table 1). After 20 days, the *PCE* remains 89% of the original value (*PCE*: 3.04%, V_{oc}: 0.59 V, J_{sc}: 9.27 mA/cm^{-2} and FF: 0.54) (Figure 3.6).

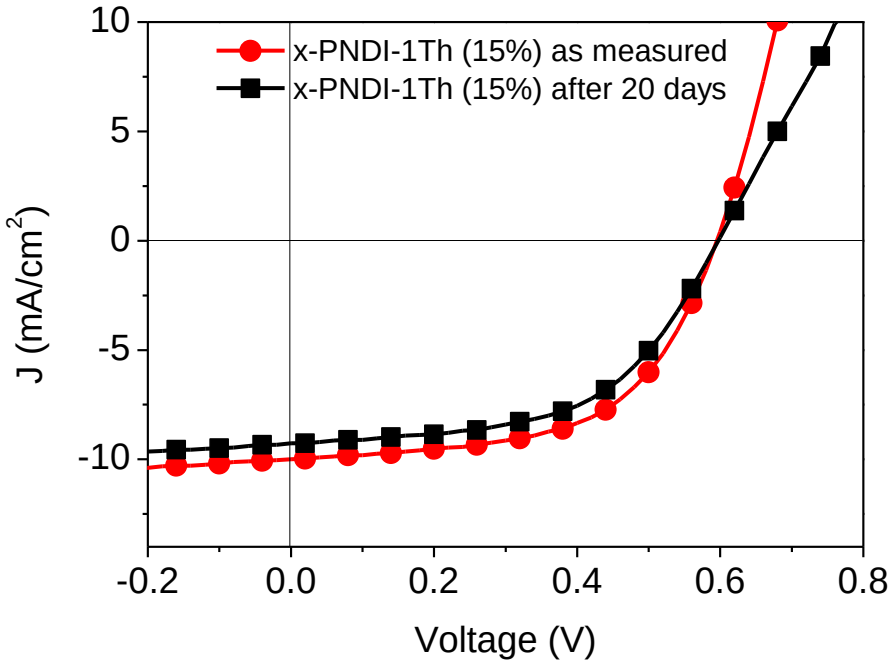

Figure 3.6 *J-V* characteristics of un-encapsulated inverted PSCs withx-PNDI-1Th (15%) before and after exposureto ambient conditions for 20 days.

3.2.3 *Organic Thin Film Transistors*

Since the electrical conductivities of the ETMs used in PSCs play a crucial role in the device performances, we further investigated the electron-transporting properties of crosslinked and doped PNDI-1Th in OTFT devices. PNDI-1Th and x-PNDI-1Th (0-15%) solutions were prepared by the same method used in solar cell devices. The polymer solutions were spin-coated at 2000 rpm. The OTFT devices were fabricated in the typical top-contact, bottom-gate geometry on hexamethyldisilazane (HMDS) treated doped-Si/SiO_2 wafers. All device testing was performed in an inert atmosphere. A linear fit was applied in the saturation region of the sqrt I_{ds} vs V_g curve in order to calculate charge carrier mobility using the standard equation of metal-oxide-semiconductor field-effect transistors: $I_{ds} = (\mu W C_0/2L)(V_g - V_t)^2$.

The characteristics of OTFTs using neat polymer (PNDI-1Th) showed typical n-type behavior at positive gate-source bias (V_{gs} = +100 V), with mobility of 1.93× 10^{-4} $cm^2/V \cdot s$ similar to those reported previously in the literature (Figure 3.7a and Table 3.2).[68] Crosslinking of PNDI-1Th decreased the electron mobility to 4.75× 10^{-6} $cm^2/V \cdot s$ probably because crosslinking interrupts the molecular packing of the polymer. The on/off ratios of PNDI-1Th increased from 10^2 to 10^4 and V_t shifted from 6 to 13 V after crosslinking.

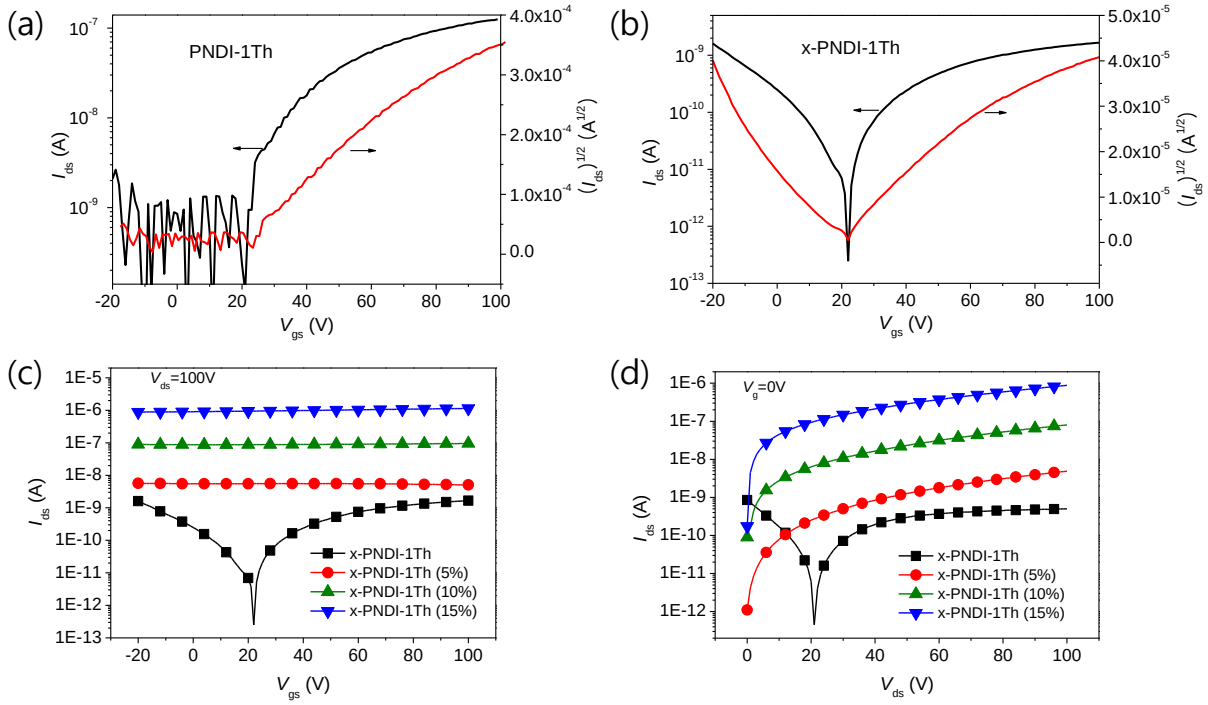

Figure 3.7 Transfer characteristics of OFETs with (a) PNDI-1Th, (b) x-PNDI-1Th and (c) x-PNDI-1Th at varying doping concentrations. (d) Output curves at zero gate voltages for the same devices.

Table 3.2 OTFT electrical properties for PNDI-1Th before and after crosslinking.

ETM	μ [$cm^2/V \cdot s$]	I_{on}/I_{off}	V_t [V]
PNDI-1Th	1.93×10^{-4}	10^2	6
x-PNDI-1Th	4.75×10^{-6}	10^4	13

Table 3.3 Summary of conductivity forx-PNDI-1Th at different doping concentrations measured from OTFT devices.

Active layer	σ [S/m]
x-PNDI-1Th	1.56×10^{-6}
x-PNDI-1Th (5%)	2.41×10^{-5}
x-PNDI-1Th (10%)	3.83×10^{-4}
x-PNDI-1Th (15%)	4.04×10^{-3}

The devices comprised of n-doped x-PNDI-1Th reveal that n-doping significantly improves electrical conductivity of the polymer (Figure 3.7c and d and Table 3.3). All of the doped devices exhibit field-independent *I-V* behavior with negligible on/off ratios,which are typical behaviors of conductors (Figure 3.7c and Table 3.2).

Figure 3.7d shows that the output current of devices increased with increasing the doping concentrations. Field-effect conductivity was derived from gated two-terminal measurements with the equation of $\sigma=(L/A)(I_d/V_d)$, where L and A are the channel length and cross-sectional area of the devices, respectively.[51] As doping concentration increased from 0 to 15%, the conductivity increased monotonically from 1.56×10^{-6} to 4.04×10^{-3} S/m. The dependence of

conductivity on the doping concentration of x-PNDI-1Th-based OTFT devices helps to explain the observed improvement of the PCEs of solar cells.

3.3 CONCLUSION

In conclusion, we have studied the *in-situ* process of n-doping and crosslinking of thiophene-NDI copolymers to make highly conductive and solvent resistant ETMs. Not only the device performance of PSCs using n-doped and crosslinked polymeric ETMs is similar to that reported with metal oxide based ETMs, but these devices also show good air-stability. Thus, this work opens the way for taking further steps toward all-organic solar cells and for progress on generally applicable polymeric interface materials, providing an effective fabrication method for solution-processed multilayer solar cell devices.

3.4 EXPERIMENTAL

Fabrication and characterization of OTFT devices: Thin film transistors were fabricated as typical top contact, bottom gate devices on silicon substrates. Heavily doped p-type silicon <100> substrates from Montco Silicon Technologies Inc. with a 300 nm (±5 nm) thermal oxide layer acted as a common gate and dielectric layer. After cleaning the substrates by sequential ultrasonication in acetone, methanol, and isopropyl alcohol for 10 min followed by air plasma treatment, a self-assembled monolayer of HMDS was formed by vapor deposition. The substrates were then washed with chloroform and isopropyl alcohol to remove physisorbed silane agents. Polymer thin films were deposited from a 0.5 wt % chlorobenzene solution by spin-coating (2000 rpm for 30s). Additional solutions contained 10 wt% of crosslinker, and 5, 10, and 15 wt% of the dopant. Selected substrates were submitted to a UV cross-linking treatment (λ = 254 nm) for 6 min. Thermal annealing was performed at 110 ℃ on a hot-plate for 10 min under

nitrogen atmosphere. Inter-digitated source and drain electrodes (W = 9000 μm, L= 90 μm) made of gold (50 nm thick) were deposited on top of the active layers by thermal evaporation at 1.0 Å/s through a shadow mask from a resistively heated Mo boat under high vacuum (5.0×10^{-7} torr). A HP4145B semiconductor parameter analyzer controlled by locally written LabView codes through a GPIB interface was used for characterization. All device characterization was performed in a nitrogen atmosphere.

Fabrication and characterization of inverted PSCs: To fabricate the inverted PSCs, ITO glass substrates were cleaned with de-ionized water, acetone, and isopropyl alcohol, and then treated with oxygen plasma. Polymer thin films (x-PNDI-nTh (0-15%)) were deposited from a 0.5 wt % chlorobenzene solution by spin-coating (4000 rpm for 30s). Polymer solutions contained 10 wt% of crosslinker, and 5, 10, and 15 wt% of the dopant. The substrates were submitted to a thermal annealing (150 ℃ for 10 min) and a UV cross-linking (λ = 254 nm, 6 min) under nitrogen atmosphere. Afterward, a chlorobenzene solution (60 mg/ml) of PCBM (American Dye Source, Inc., 99.0% purity) and P3HT (Rieke Metals, Inc., 4002-E grade) (0.7:1 weight ratio)was spin-coated on the electron transporting layer and annealed at 160 ℃ for 10 min. After annealing, a PEDOT:PSS solution (H. C. Starck, Clevios 4083) was spin-coated onto the active layer, and then the devices were annealed for 10 min at 120 ℃. A metal electrode (Ag) was then vacuum-deposited at a rate of 2 Å/s.

Chapter 4. IN SITU N-DOPING AND CROSSLINKING OF FULLERENE DERIVATIVES FOR EFFICIENT AND ROBUST ELECTRON-TRANSPORTING LAYER IN POLYMER SOLAR CELLS

4.1 INTRODUCTION

By virtue of comprehensive investigations of interfacial materials, active materials and device engineering, the PCE of bulk hetero-junction polymer solar cells (BHJ PSCs) has been significantly improved over the last decade.[5] As one of the key elements in PSCs, interfacial layers play a crucial role in transporting charge carriers from the active material into the electrode and in preventing interfacial charge recombination.[69, 70] More specifically, an ideal interfacial layer usually serves several functions in PSCs such as (i) energy level tuning at the interfaces between the electrodes and the active layer to achieve Ohmic contact,[71, 72] (ii) determining the polarity of the electrodes and improving charge selectivity to minimize interfacial charge recombination and improve the rectification of the current-voltage response with unipolar charge extraction,[73, 74] (iii) controlling surface morphology of the active layer by altering the surface energy of the interfacial layers to obtain appropriate vertical phase segregation in the BHJ active layer,[75-79] and (iv) improving chemical and mechanical stability of devices.[80, 81] However, simultaneously fulfilling multiple functions with a single interfacial material remains one of the key challenges to PSCs. Recently, apart from the commonly used inorganic electron transporting layer (ETL) (TiO_x, ZnO, etc.), several organic interfacial materials such as polyethyleneimine (PEI),[82] ethoxylated polyethyleneimine (PEIE),[83] polyfluorene derivatives (PFN),[84] and Fulleropyrrolidium iodide (FPI) have been used for inverted PSCs.[85, 86] Particularly, a thin layer of non-conjugated polyelectrolytes (PEI and PEIE) efficiently reduce the work function of the ITO from 4.8 to ~4.0 eV, which increases the built-in potential within the devices and concomitantly enhances open-circuit voltages (V_{oc}).[82, 83]

On the other hand, the molecular doping of conjugated polymer and small molecule based interfacial materials is important to PSCs.[87-89] The successful development of PSC devices by

incorporating doped semiconducting layers is mainly due to the ability to tune their electronic properties by increasing conductivity and shifting the Fermi-levels towards the transport states, which result in good Ohmic contact at the metal/doped semiconductor interfaces and reduces the energetic barrier at doped semiconductor/semiconductor (active layer) interfaces.[90, 91] However, doped interfacial layers using typical conjugated polymers and small molecules are rarely applied to PCSs because they often have low solvent resistance and have poor morphology with severe phase separation between inorganic dopants and semiconductors at high doping concentration. Furthermore, in the case of inorganic dopants, metal ions can diffuse through semiconducting transport layers during device processing and operation, which can cause electrical shorting of the devices and limits device lifetime.[92]

Previously we have demonstrated that *in-situ* chemical n-doping of crosslinked fullerene[93] and naphthalene diimide[94] provide a conductive organic layer with desired solvent-resistance for ETL in inverted PSCs.[93, 94] While performance was enhanced, we also found that the diffusion of inorganic dopants was problematic and caused severe phase separation resulting in a rough surface morphology. In addition, dewetting of the conductive layer was also found to occur at high doping concentration.[93] Benzoimidazol based organic n-dopants have been used together with a bis(perfluorophenyl) azide crosslinker to circumvent these problems by creating *in-situ* n-doped and crosslinking of naphthalene diimide-based polymeric ETLs.[94] However, achieving desired electrical and mechanical properties of the ternary blend of the dopant, crosslinker and n-type polymer is non-trivial and required tedious optimization process, which complicates the use of those materials for OPVs.

Recently we found that iodide on FPI (and common tetrabutyl ammonium salt) can undergo anion-induced electron transfer (AIET) to the fullerene core, which results in n-doping

of fullerene. A high conductivity of up to 2.0 S/m has been obtained via electron transfer from iodide on fulleropyrrolidinium ions (**FPI**) to its fullerene core.[95-98] However, the use of **FPI** as a ETL for PSCs is limited because it can be dissolved in both nonpolar (chloroform, *o*-dichrolobenzene) and polar (methanol) solvents. Thus, it is imperative to develop a simple method to make fullerene-based ETLs with high conductivity and good solvent resistance.

Herein we report efficient and robust ETLs by incorporating conductive fullerene dopant into a thermally crosslinkable fullerene matrix. The in-situ process of n-doping and crosslinking has significantly improved the PCE of PSCs from 2.43 to 5.26% in proof-of-concept devices by improving the electrical conductivity and solvent resistance of the ETLs. The ETLs were further studied by characterizing organic thin film transistor (OTFT) devices and x-ray photoelectron spectroscopy (XPS) to correlate enhanced electrical conductivities and energy level alignment with the device performances in PSCs.

4.2 Results and Discussion

4.2.1 *Synthesis of Crosslinkable Fullerene and its optical, electrical, and thermal properties*

We have designed styrene group functionalized crosslinkable fullerene, (1,4-di(vinylbenzyl)fullerene, hereafter referred to as **Full-s**) to make the size of the reactive units as small as possible in order to acheive high electron mobility. We stress that this is so far the most simple structure of crosslinkable fullerene.[99] The synthesis of **Full-s** is achieved in one pot reaction from [60]fullerene (Figure 4.1a). Reduction of C_{60} with potassium/1-methylnaphthalene at room temperature in THF afforded C_{60} dianion as a dark red solution. The reaction of the dianion with 4-vinylbenzyl chloride afforded **Full-s** in 45% yield, and was characterized by MALDI-TOF MS, proton and carbon NMR, as well as single crystal analysis.

In the single-crystal analysis of **Full-s**, it shows that fullerene cores were tightly packed together

with the closest fullerene's centroid-to-centroid distance of ~9.92 Å (Figure 4.2), which is even shorter than the reported value of [C_{60}]PCBM crystals (~10.13 Å).[100] A densely packed molecular structure can be seen in Figure 4.1b, showing that fullerene and vinylbenzyl groups are orderly segregated in a crystalline phase, which would ideally facilitate styrene cross-linking, while maintaining the fullerene channel in order to enable efficient charge transport.

The **bis-FPI** doped **Full-x** films were simply prepared by spin-coating a chlorobenzene (CB) solution of two fullerene materials and then crosslinking them via thermal annealing resulting in a solvent resistant film. Concurrently, n-doping occurs through AIET in solid state from iodide in **bis-FPI** to the fullerene core (Figure 4.1c (right)). The chemical structure of **bis-FPI** was shown in Figure 4.1c (left). Figure 4.1d shows the schematic representation of the device structure of PSCs with **bis-FPI** dispersed **Full-x** layers.

The energy levels of **Full-s** were studied by cyclic voltammetry. The result shows that there are three stable and reversible reduction peaks. The first reduction potential ($E_{1/2}^{red\,1}$) was observed at –1.08 V. This value is similar to that of PCBM (**$E_{1/2}^{red1}$**: –1.07 V) (Figure 4.3a), which suggests that **Full-s** has similar LUMO level with PCBM. Figure 4.3b shows the thermal properties of **Full-x** studied by differential scanning calorimetry (DSC). There is a distinct exothermal peak at 230 °C, which is ascribed to the thermal crosslinking of the styrene groups on **Full-x**. Note that there is no obvious transition peaks in the second scan, showing that **Full-s** is fully crosslinked by thermal annealing. The solvent resistance of the crosslinked **Full-x** film was studied by absorption spectroscopy. The Full-x films containing 25 mol% of bis-FPI, hereafter referred to as Full-x (25%, bis-FPI), were prepared by spin coating of a chlorobenzene solution and crosslinked by annealing at 210 ℃ for 30 minutes in a dry nitrogen filled glove box.

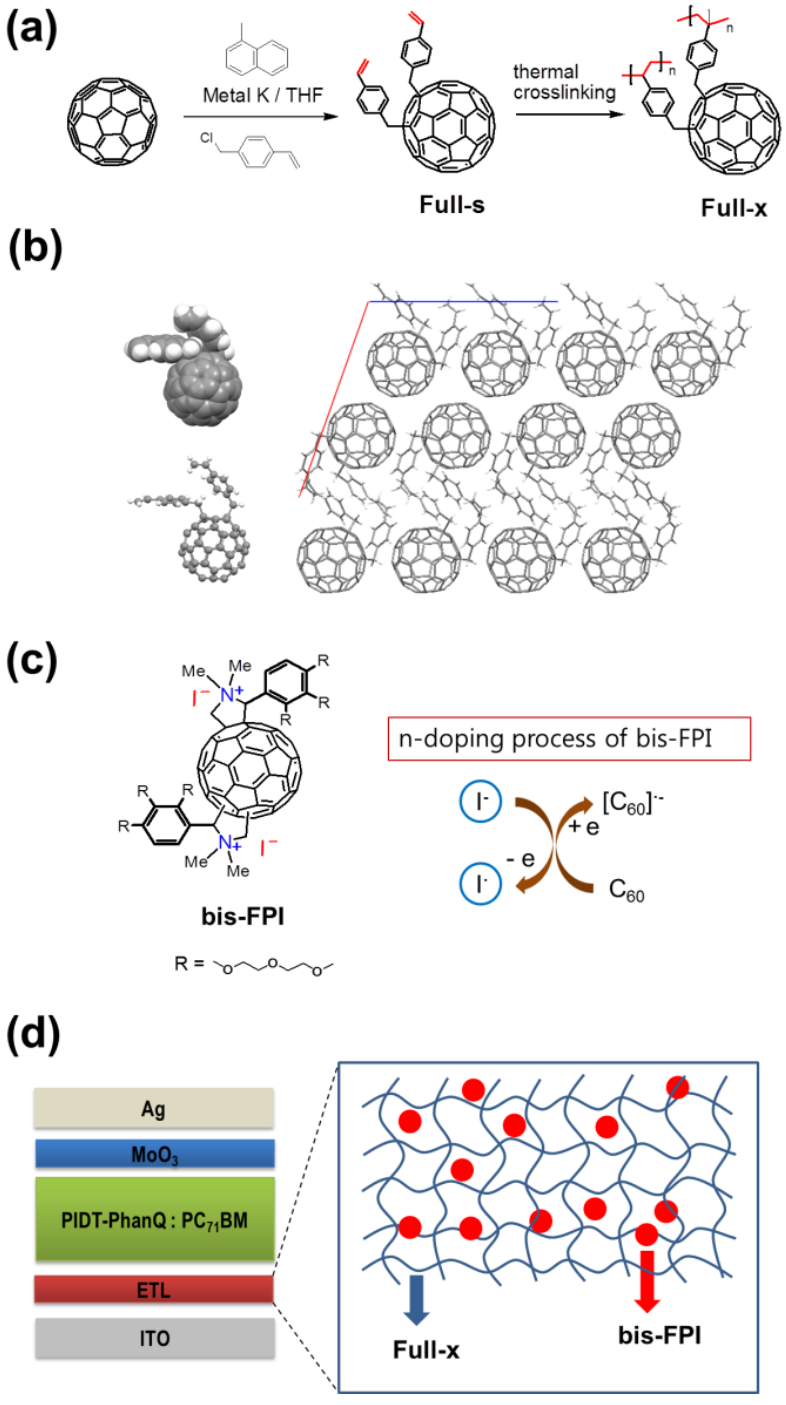

Figure **4.**1 (a) The synthetic procedure of **Full-s** and its thermally crosslinked **Full-x**. (b) The single crystal analysis of **Full-s**. Molecular packing of **Full-s** shows that fullerene and vinylbenzyl groups segregated in a crystalline phase. (c) The chemical structure of **bis-FPI** (left) and its doping mechanism through anion-induced electron transfer (AIET) process (right). (d) Schematic representation of the device structure of PSCs with **bis-FPI** dispersed **Full-x** layers.

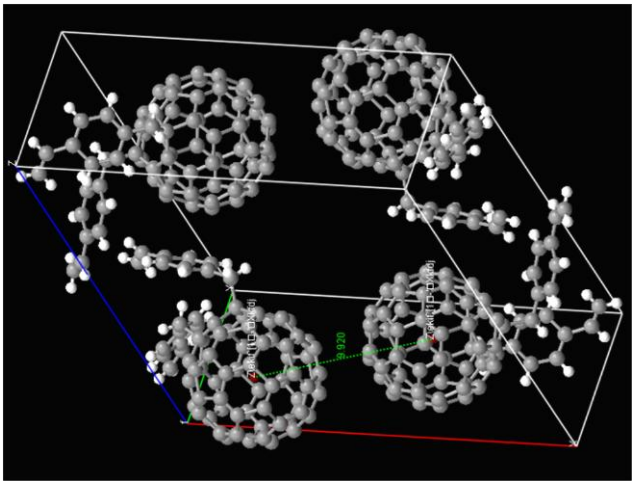

Figure 4.2 Single-crystal analysis of **full-s** showed the closest centre-to-centre distance of 0.99 nm for two fullerenes.

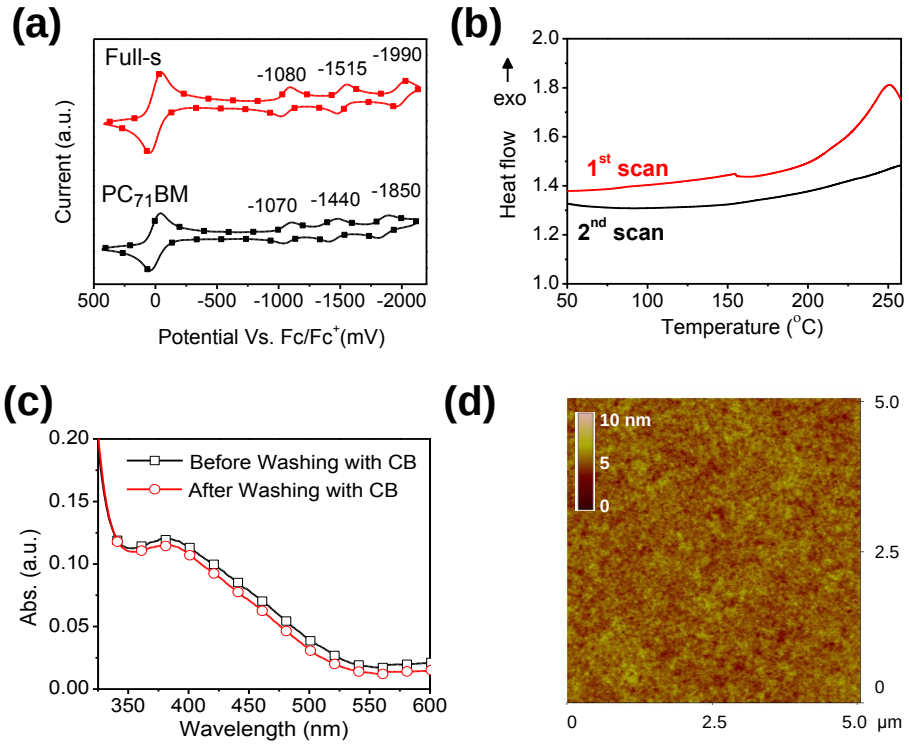

Figure 4.3 (a) Cyclic voltammogram of **Full-s** and $PC_{71}BM$ in ODCB/MeCN (5:1 v/v) (0.5 mM) containing TBAH (0.1M) at a scan rate of 100 mV s^{-1} (b) DSC thermograms of **Full-s**. (c) Thin film absorption spectra of **Full-x (25%, bis-FPI)** before and after washing with chlorobenzene. (d) AFM images of **Full-x (25%, bis-FPI)**.

Figure 4.3c shows the absorption spectra of the **Full-x (25%, bis-FPI)** films before and after washing with chlorobenzene, which reveals that **Full-x (25%, bis-FPI)** films have good solvent resistance. Atomic force microscopy (AFM) was used to investigate the topography and surface roughness of the **Full-x (25%, bis-FPI)** films. Figure 4.3d shows the height images of the x-Full films with a surface roughness of 0.5 nm, indicating that the film is smooth and homogeneous.

4.2.2 *Solar cell Performances*

As a proof-of-concept, we have fabricated inverted PCSs using **Full-x** films with various **bis-FPI** concentrations. Solar cell devices were fabricated with ITO/ETL/PIDT-PhanQ:$PC_{71}BM$/ MoO_3/Ag stacks, and tested under simulated AM 1.5G illumination at 100 mW/cm^2 in a dry N_2 filled glove box. The active layers were deposited on ETLs by spin coating the PIDT-PhanQ:PC71BM (1:3, weight ratio) solution (40 mg/ml in DCB) and then annealed at 110 ℃ for 10 min in the glove box. A MoO_3 (5 nm) and metal electrode (Ag) (100 nm) were then deposited via thermal evaporation. Figure 4.4a shows the *J-V* characteristics of devices fabricated with different concentrations of **bis-FPI**. The photovoltaic parameters are summarized in Table 4.1. The thickness of ETLs was optimized to 12 nm. Note that J-V curves show clear trend as a function of the concentration of **bis-FPI**. By increasing the concentration of **bis-FPI** from 0 to 25%, the PCE increases from 2.43 to 5.26% as a result of an increase in J_{sc}, FF, and most notably V_{oc} (from 0.53 to 0.83), which is mainly attributed to the decreased interfacial resistance and concomitantly the reduced interfacial recombination at the ETLs.

Previously, it has been reported that ethylene oxide groups reduce the work function of ITO due to interface dipoles, which results in an improved V_{oc} due to an increase in the built-in potential and thus decreasing the interfacial resistance.[101, 102] Thus, one can argue that the increase of V_{oc} is attributed to modulate the ITO work function from the interfacial dipoles formed between the

ethylene oxide side chains and ITO, when increasing **bis-FPI** concentration in ETLs. Note that **bis-FP** is the neutral fulleropyrrolidine without ammonium iodide. Therefore, there is no doping effect on the devices.

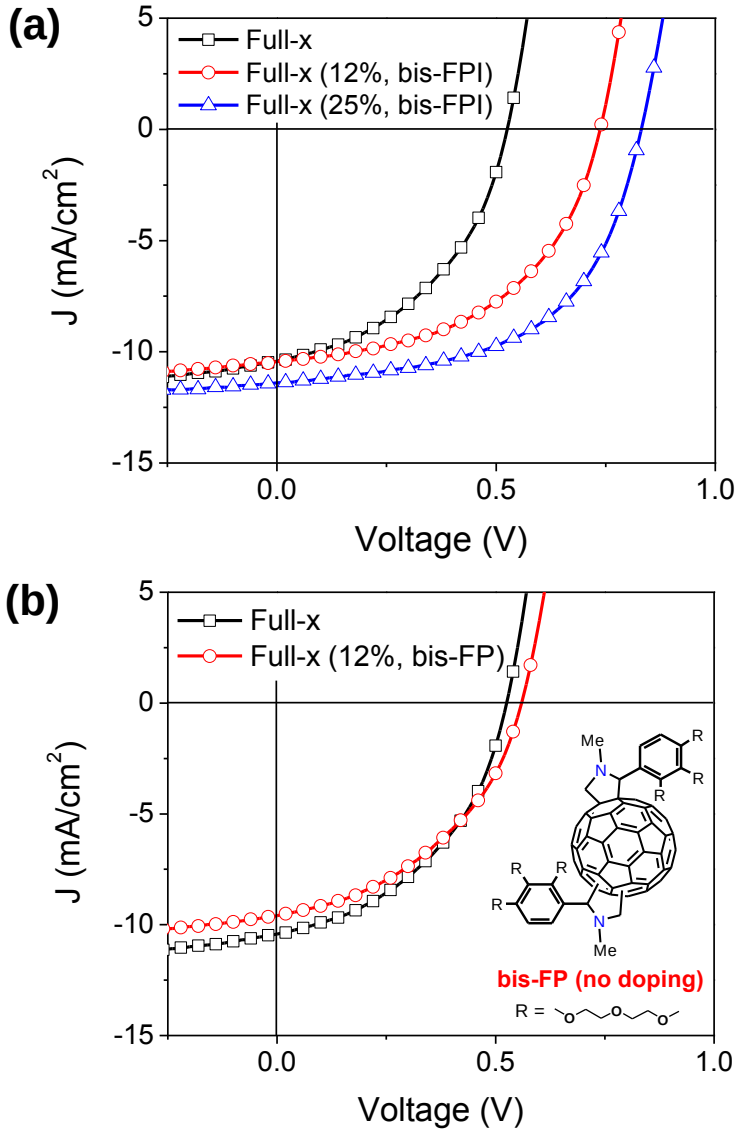

Figure 4.4 (a) *J-V* characteristics of PCSs fabricated by **Full-x** with different concentration of **bis-FPI**. (b) the chemical structure of **bis-FP** (inset figure) and the device performance of the devices made with bis-FP.

To clarify this, we fabricated reference devices by using **bis-FP** which is the neutral fulleropyrrolidine[103] with same ethylene oxide side-chains and similar chemical structure to **bis-FPI** except for ammonium iodide (inset in Figure 4.4b). As shown in Figure 4.4b and Table 4.1, only subtle fluctuations of the V_{oc} and the other device parameters were observed when **bis-FP** is used. This result clearly shows that the interfacial dipole effect from ethylene oxide functional group is negligible in these devices.

Table 4.1. Summary of device performance with various dopant concentrations.

ETL	*PCE* (%)	V_{oc} (V)	J_{sc} (mA/cm^2)	*FF*
Full-x	2.43	0.53	10.4	0.44
Full-x(12%, bis-FPI)	3.88	0.74	10.5	0.50
Full-x (25%, bis-FPI)	5.26	0.83	11.4	0.56
Full-x (12%, bis-FP)	2.32	0.56	9.6	0.43

The thickness of the ETLs is a critical factor for device performance because it plays an important role in series resistance[93] and the spatial distribution of the optical field within the device.[104] Two different films were fabricated by changing the spin speed (5k rpm for 12 nm and 2k rpm for 24 nm). The PCE of the devices fabricated with 25% bis-FPI was improved from 3.36 to 5.26% by decreasing the thickness from 24 nm to 12 nm (Figure 4.5 and Table 4.2).

The estimated series resistances (R_s) for 12 nm and 24 nm of ETLs are 3.36 and 4.26 Ω/cm^2, respectively. This indicates that the thickness of ETLs is one of the key factors in determining the overall series resistance and charge collection efficiency. From our previous work, we have found that the thickness below 10 nm often causes shorting of the devices in doped ETLs.[94] Therefore, we set the minimum thickness of ETLs as ~10 nm.

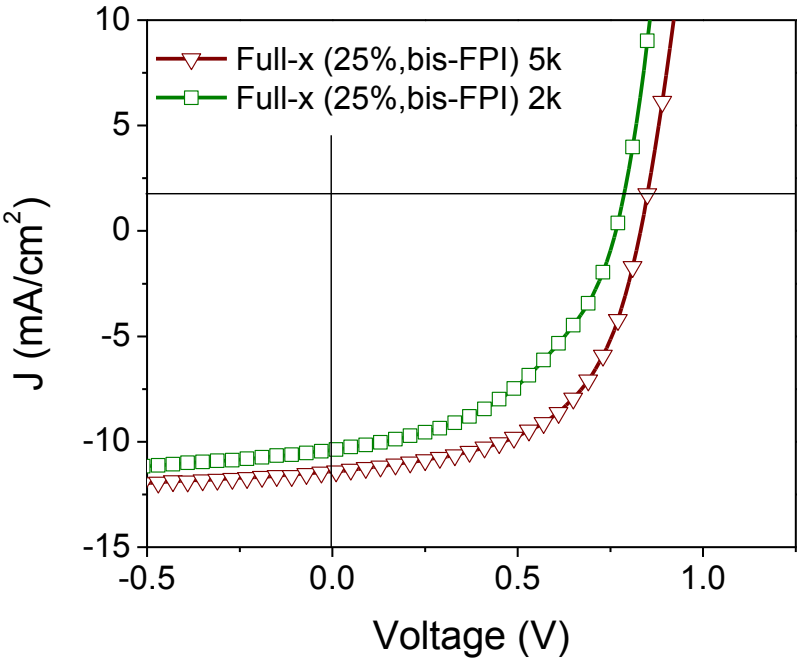

Figure 4.5. The thickness dependence of device performance for Full-x (25%, bis-FPI) fabricated by two different spin speed (5k rpm for 12 nm and 2k rpm for 24 nm).

Table 4.2 Summary of device performance with different thickness of ETLs.

ETL	PCE (%)	V_{oc} (V)	J_{sc}(mA/cm^2)	FF
Full-x (25%, bis-FPI), 12 nm	5.26	0.83	11.4	0.56
Full-x (25%, bis-FPI), 24 nm	3.66	0.76	10.4	0.46

4.2.3 *Organic Thin Film transistors and XPS analysis*

It is well known that doping of the semiconducting transport layer reduces Ohmic losses at metal/doped semiconductor interfaces by increasing the electrical conductivity. Furthermore, the doping can facilitate the extraction of photogenerated charge carriers by lowering the energetic barrier for charge carrier extraction at doped semiconductor/active layer interface. This occurs

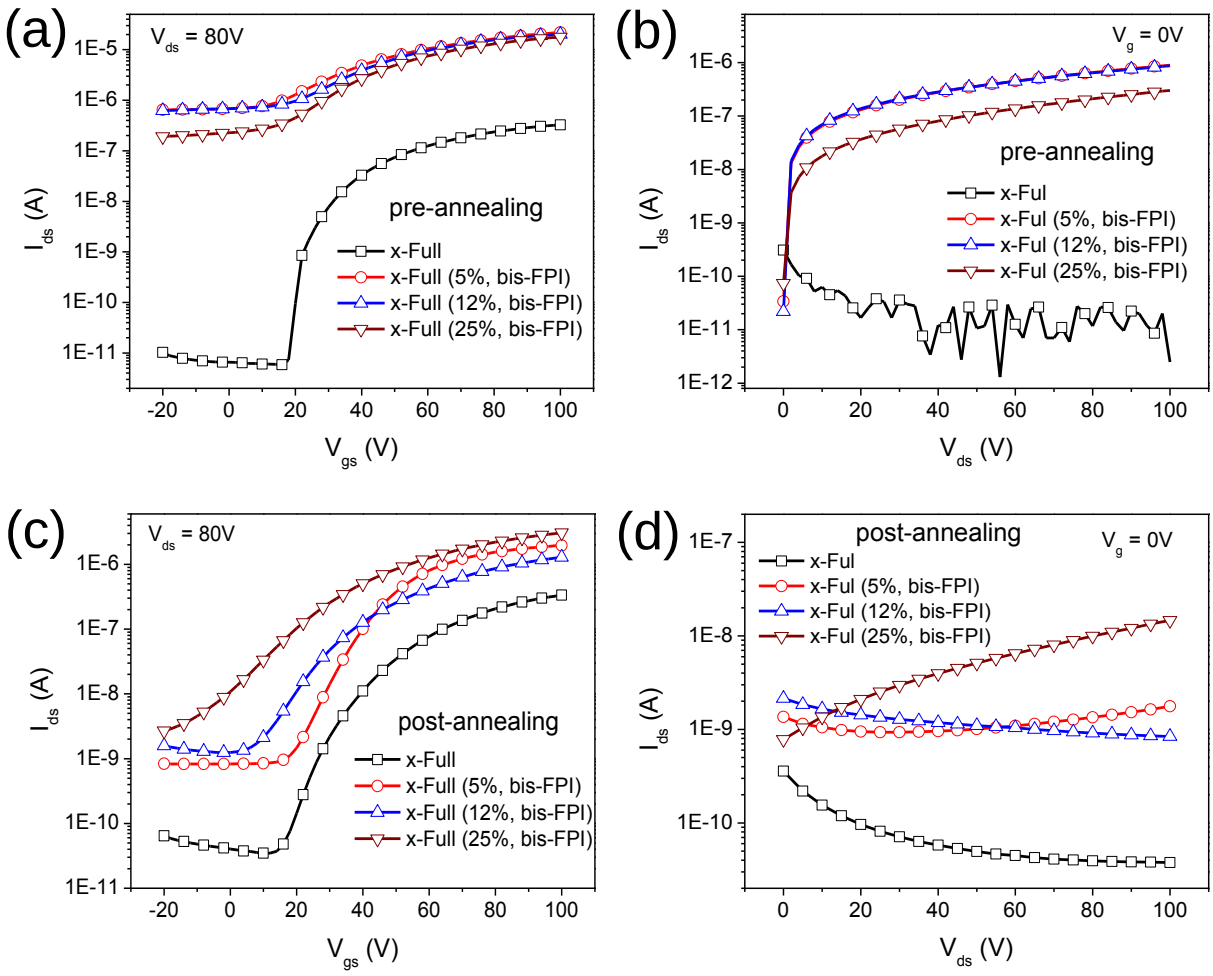

Figure 4.6 Transfer characteristics of OTFT devices with x-Full at varing bis-FPI concentrtion before crosslinking (pre-annealing) (a) and after crosslinking (post-anneaning) (c). Output charateristics for the same devices before crosslinking (b) and after crosslinking (d).

when favourable energy level alignment is achieved through a work function shift or when the energy levels become almost flat. To further investigate the electrical conductivity of the **x-Full** (**bis-FPI**) films and their energetic alignment, we have fabricated OTFT devices and conducted XPS measurements. All **x-Full** (**bis-FPI**) films studied in OTFT and XPS measurement were prepared by the same method with ETLs in solar cell devices. The OTFT devices were fabricated

with $p^{++}Si/SiO_2$/BCB/Full-x (bis-FPI)/Ag structures, and were characterized in a glove box with an Agilent 4155B semiconductor parameter analyzer. A thermally crosslinked divinyltetramethyl siloxane-bis(benzocyclobutene) (BCB) layer was used to passivate the surface hydroxyl groups on the SiO_2 gate dielectric. Charge carrier mobility was calculated with a linear fit of the saturation region of the square root of I_{ds} versus V_{gs} using the standard equation: $I_{ds} = [(\mu WC_0/2L)/(V_g-V_t)^2]$, where W, C_0, and L are channel width, capacitance of gate dielectrics and channel length, respectively. The electrical conductivity was estimated from the V_d-I_d curves measured at zero gate bias as reported previously.[98]

As shown in Figure 4.6c and Table 4.3, undoped **Full-x** exhibited a typical n-type transfer curve with electron mobility of 3.1×10^{-4} $cm^2/V \cdot s$ and an on/off ratio of 9.6×10^3, indicating that it is a typical n-type semiconductor. Upon increasing the concentration of **bis-FPI** up to 25%, all devices show a negative shift in threshold voltage, decrease of on-off ratio, and increase of output current. This suggests that an n-doping process via AIET has efficiently occurred. The electrical conductivity of **Full-x** films increased up to ~10^{-4} S/cm upon increasing the concentration of **bis-FPI** (**Table 2**). It is worth noting that AIET process has already occurred in **Full-s (bis-FPI)** films without thermal annealing, which agrees with our previous study.[98]

Note that **Full-s** is referred to as non-crosslinked films. For example, the conductivity of **Full-s (12%**, **bis-FPI)** and **Full-s (25%**, **bis-FPI)** is 9.1×10^{-3} and 2.0×10^{-3} S/m, respectively (Figure 4.6b and Table 4.3). The conductivity of **Full-s (25%**, **bis-FPI)** is one order of magnitude higher than that of the **Full-x (25%**, **bis-FPI)** films. This is probably due to the fact that crosslinking at relatively high temperature causes the degradation of electrical properties of **bis-FPI**. Nevertheless, it represents one of the rare examples of doped fullerene films that can be processed and survive such harsh processing conditions (annealing at 210 ^oC for 30 min). The

OTFT data clearly shows that the enhanced conductivity of about three orders of magnitude upon the addition of **bis-FPI** into **Full-x** matrix is the origin of the improved device performance in solar cells.

Table 4.3 Summary of device performance with various ETMs. The electrical properties for pre-annealed devices for **Full-s** were shown in parenthesis.

ETL	σ (S/m)	μ (cm2/V·s)	I_{on}/I_{off}	V_t (V)
x-Full	3.1×10^{-7} (1.3×10^{-7})	3.1×10^{-4} (3.4×10^{-4})	9.6×10^{3} (5.6×10^{4})	30 (21)
x-Full (5%, bis-FPI)	7.9×10^{-6} (9.5×10^{-3})	2.1×10^{-3} (1.3×10^{-2})	2.4×10^{3} (3.4×10^{1})	30 (3)
x-Full(12%, bis-FPI)	3.5×10^{-6} (9.1×10^{-3})	4.8×10^{-4} (1.5×10^{-2})	1.0×10^{3} (3.2×10^{1})	16 (9)
x-Full (25%, bis-FPI)	1.3×10^{-4} (2.0×10^{-3})	1.2×10^{-3} (8.1×10^{-3})	1.1×10^{3} (9.3×10^{1})	6.5 (13)

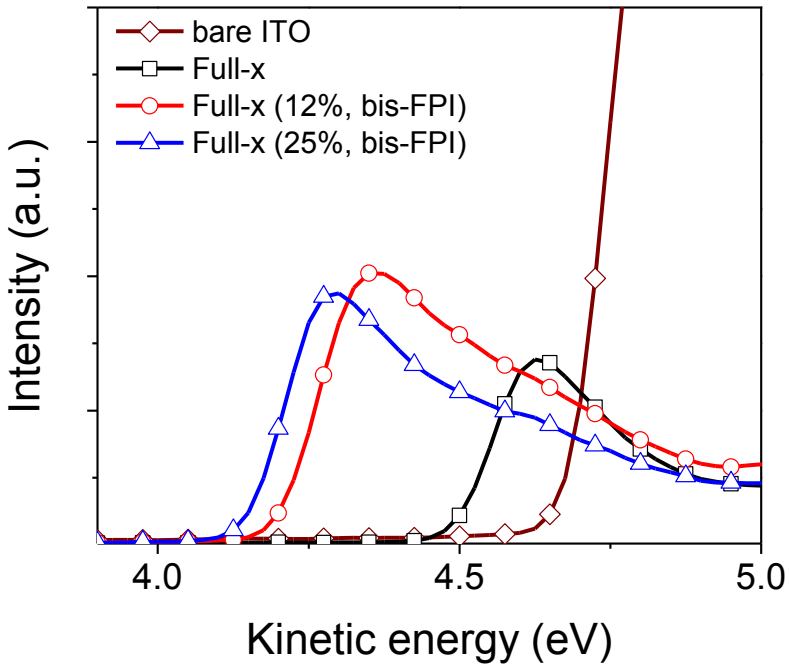

Figure 4.7 Secondary cutoffs of bare ITO and **Full-x** films with different **bis-FPI** concentration on ITO substrate measured by XPS.

Not only does the enhanced conductivity, but also the electronic structure of the doped ETLs play an important role in the charge carrier extraction efficiency. For efficient electron transport from the active layer to the electrodes through ETLs, a work function of the ETLs should be similar with that of PCBM active layer in order to reduce V_{oc} and J_{sc} losses by decreasing energetic barriers at the interfaces. As shown in Figure 4.7, we observed that the work function of the films measured from x-ray photoemission spectroscopy (XPS) reduced from 4.49 eV (**Full-x**) to 4.15 eV (**Full-x (25%, bis-FPI)**). These results further clarify that the appropriate energy level alignment together with enhanced conductivity are the key parameters for efficient extraction of charge carriers from active layers.

4.3 CONCLUSION

In this work, we have investigated a fullerene self-dopant and a crosslinkable fullerene as an ETL for inverted polymer solar cells. The functions and impact of solvent resistant and highly conducting ETLs on the device performance were clearly characterized in the OSC and OTFT devices together with XPS analysis. The specific properties of the fullerene self-dopant can be investigated in the future to further simplify *in-situ* doping and crosslinking process.

4.4 EXPERIMENTAL

Synthesis: All reactions dealing with air- or moisture-sensitive compounds were carried out using standard Schlenk technique. All ^{1}H (500 MHz) and ^{13}C (125 MHz) spectra were recorded on a Bruker AV500 spectrometer. Spectra were reported in parts per million from internal tetramethylsilane (δ 0.00 ppm) or residual protons of the deuterated solvent for ^{1}H NMR and from solvent carbon (e.g. δ 77.00 ppm for chloroform) for ^{13}C NMR. AFM images under tapping mode were taken on a Veeco multimode AFM with a Nanoscope III controller. Cyclic

voltammetry (CV) measurements were carried out in a one-compartment cell under N_2, equipped with a glassy-carbon working electrode, a platinum wire counter electrode, and an Ag/Ag+ reference electrode. Measurements were performed in ODCB/MeCN (5:1 v/v) (0.5 mM) containing tetrabutylammonium hexafluorophosphate (0.1 M) as a supporting electrolyte with a scan rate of 100 mV/s. All potentials were corrected against Fc/Fc+. C_{60} and PCBMs were purchased from American Dye Source. The matrix for MALDI-TOF-MS used 2:1 mixture of alpha-cyano-4-hydroxycinnamic acid (CHCA)/2,5-dihydroxybenzoic acid (DHB) in acetonitrile. C_{60} was purchased from American Dye Source. 4-Vinylbenzyl chloride was purchased from Sigma-Aldrich. Unless otherwise noted, materials were purchased from Aldrich Inc., and used after appropriate purification.

*Synthesis of 1,4-di(vinylbenzyl) fullerene (**Full-s**)* To a freeze-thaw degassed mixture of C_{60} (2000 mg, 2.78 mmol) and 1-methylnaphthalene (11.8 ml, 83 mmol, 30 equiv.) in 250 mL THF, metal Potassium (271 mg, 6.95 mmol) was added in one portion. A dark red solution was produced after stirring under argon at room temperature for 5 hours. 4-vinylbenzyl chloride (8.5 ml, in 90% purity, ~ 54 mmol) was then added. With stirring for another 3.5 hours, the reaction mixture was then heated 50 ^{o}C for overnight, finally quenched with degassed saturation aqueous NH_4Cl (2 mL). The concentrated resulting mixture was precipitated by methanol. Crude product was absorbed with silica gel, then separated by silica gel column (eluent: first with CS_2/hexane = 1/5, then CS_2/hexane = 1/2, then CS_2). Compound 9 was achieved in 45 % yield. **Full-s** ^{1}H NMR (300 MHz, $CDCl_3$): δ 3.88 (s, 4H, C*H*$_2$), 5.27 (dd, J_1 = 5.0 Hz and J_2 = 0.9 Hz, 2H), 5.27 (dd, J_1 = 8.25 Hz and J_2 = 0.9 Hz, 2H), 6.76 (dd, J_1 = 3.30 Hz and J_2 = 10.8 Hz, 2H), 7.56 (m, 8H, Ar-*H*) ^{13}C NMR (125 MHz, $CDCl_3$): δ 48.44, 60.47, 114.01, 128.26, 131.22, 135.76, 138.84, 140.54, 141.98, 142.45, 142.64, 142.97, 143.09, 143.19, 143.71, 143.94, 144.12, 144.25, 144.27, 144.37,

144.67, 144.69, 144.77, 145.01, 145.50, 146.14, 146.92, 146.97, 147.17, 148.63, 148.64, 151.72, 157.71.

Fabrication and characterization of OTFT devices: A top contact OTFT devices were fabricated on silicon substrates. Heavily p-doped Si/SiO_2 (300nm) substrates were purchased from Montco Silicon Technologies Inc. The substrates were cleaned by sequential ultrasonication in acetone, methanol, and isopropyl alcohol. A thermally crosslinked divinyltetramethylsiloxane-bis(benzocyclobutene) (BCB) layer was used to passivate the surface hydroxyl groups on the SiO_2 gate dielectric. The Full-x (bis-FPI) films were prepared from a 2 wt % chlorobenzene solution by spin-coating (5000 rpm for 120s). The gold (50 nm thick) electrodes were deposited on top of the fullerene films by thermal evaporation at 1.0 Å/s through a shadow mask under high vacuum (5.0×10^{-7} torr). The devices were characterized in a glove box with an Agilent 4155B semiconductor parameter analyzer.

Fabrication of PSCs: ITO coated glass substrates were cleaned by sequential ultrasonication in acetone, methanol, and isopropyl alcohol, and then treated with oxygen plasma. The ETLs (Full-x and Full-x (bis-FPI)) were prepared from a 2 wt % chlorobenzene solution by spin-coating (2000 rpm and 5000 rpm for 120s). The substrates were submitted to a thermal annealing (210 ℃ for 30 min) under N_2 atmosphere. The active layers were deposited on ETLs by spin coating the PIDT-PhanQ:PC71BM (1:3, weight ratio) solution (40 mg/ml in DCB) and then annealed at 110 ℃ for 10 min in the glove box. A MoO_3 (5 nm) was then deposited via thermal evaporation at a rate of 0.2 Å/s. Afterward, a metal electrode (Ag) (100 nm) was vacuum-deposited at a rate of 2 Å/s.

Chapter 5. PHOTO-CROSSLINKED CONDUCTING FULLERENE INTERLAYERS FOR POLYMER SOLAR CELLS

5.1 INTRODUCTION

Extraction of photo-generated charge carriers from the active materials to the electrodes is a critical process for improving power conversion efficiency (PCE) in PSCs.[69, 105-110] In general, thin interlayers are introduced between the metal electrodes and the active layers significantly improve the charge extraction efficiency. This is because the interlayers tune energetic barriers and interfacial dipoles at the metal/semiconductor interfaces, thus playing a crucial role in transporting charge carriers.[111] In addition, the interlayers minimize surface recombination by harvesting one of the charge carriers more rapidly than the other, preventing the accumulation of space charges at the interfaces.[112, 113] They also improve the chemical, mechanical, and morphological stabilities of the devices.[75-77, 80, 81]

Over the last decade, a conducting polymer, poly(ethylenedioxythiophene):poly(styrene sulfonate) (PEDOT:PSS), has been almost universally used as a hole transporting material (HTM) in PSCs. Its usage is attributed to its high conductivity, orthogonal solubility to the active layers, good solution processability, and appropriate energy levels with respect to commonly used transparent metal electrodes such as indium tin oxide (ITO).

In contrast to the development of PEDOT:PSS, relatively little attention has been paid to develop stable organic electron transporting materials (ETM). Recently, several polyelectrolyte interlayers have been reported to increase device performance by manipulating the work function of ITO.[82-84] In addition, chemical n-doping of semiconducting polymers and small molecules has been used to make a better electrical contact by reducing contact resistances at interfaces.[87, 114] In practice, developing solution-processable and stable n-doped organic semiconductors is challenging because of the intrinsic instabilities of doped semiconductors and the difficulty of finding suitable dopants that have oxidative stability in ambient conditions and solid-state

miscibility with host materials.[115] Previously, a self n-doped fullerene was developed as a highly conducting ETM with a high conductivity of up to 2×10^{-2} S cm^{-1}.[116] **Bis-FPI** has great advantages over traditional semiconductors doped with inorganic and organic dopants, particularly in its ability to be self-doped via anion-induced electron transfer (AIET) from iodide to fullerene cage of fulleropyrrolidium-iodide (**FPI**). More recently, we have developed efficient and solvent resistant ETMs by incorporating **bis-FPI** into a styrene functionalized thermally crosslinkable fullerene.[117] However, we found that the conductivity of **bis-FPI** doped crosslinked fullerene films decreased one order of magnitude because of the harsh annealing process (210 ℃ for 30 min) required for thermal crosslinking. This is due to the degradation of pyrrolidium-iodide functional group of **bis-FPI** at relatively high temperature. Therefore, the feasibility of using a thermally crosslinkable fullerene with **bis-FPI** is limited, especially for sophisticated and multilayered organic electronic devices. Thus, an investigation of a crosslinking method that does not sacrifice the electrical properties of **bis-FPI** is needed to further develop **bis-FPI** interlayers.

Herein we report the development of photo-crosslinked and conducting fullerene-based ETMs by incorporating a bis(perfluorophenyl) azide (PFPA) photo-crosslinker into the **bis-FPI** (**Figure 5.1a**). We show that the use of photo-crosslinked **bis-FPI** (hereafter referred to as **x^{post}-bis-FPI**) significantly enhances charge extraction efficiency and concomitantly improves device performances in PSCs. In particular, we observe that introducing PFPA crosslinker into the **bis-FPI** significantly increases electrical conductivity after photo-crosslinking. By taking advantage of these improvements, we fabricate the proof-of-concept devices for tandem solar cells and double layered organic thin-film transistor (OTFT) devices using **x^{post}-bis-FPI**, showing that **x^{post}-bis-FPI** can be a good candidate for multilayered organic electronic devices. The **x^{post}-bis-**

FPI was studied in further detail by using X-ray photoelectron spectroscopy (XPS) and conductivity measurement to investigate its energy levels and charge transporting properties and to correlate its electronic properties with device performances.

5.2 RESULTS AND DISCUSSION

5.2.1 *Photo-crosslinking of bis-FPI*

PFPA was chosen as a photo-crosslinker because the active singlet nitrenes generated by the UV-induced photolysis of the azide functional groups can react with the ethylene oxide side chains of **bis-FPI**.[118] To prepare **x^{post}-bis-FPI** films, **bis-FPI** and PFPA (1:0.25, w/w) were dissolved in methanol and then spin coated onto active layer. The uncrossliked **bis-FPI**/PFPA film (hereafter referred to as **x^{pre}-bis-FPI**) was photo-crosslinked by irradiating it with UV light (254 nm) for 20 min. The **x^{post}-bis-FPI** films were n-doped via AIET as reported previously.[116] To evaluate the efficiency of photo-crosslinking, selective photo-patterning experiments and absorption measurements were carried out. **Figure 5.1b** and **c** respectively show the schematic illustration of the photo-patterning process using a photo-mask and the optical microscope image of the patterned **x^{post}-bis-FPI** after developing the uncrosslinked area with methanol. We also observed negligible absorption change in **x^{post}-bis-FPI** films (crosslinked without photo-mask) after washing with water and methanol (**Figure 5.1d**). These results reveal that crosslinking occurs efficiently and homogeneously. Atomic force microscopy (AFM) images show that **x^{post}-bis-FPI** films before and after washing with methanol have low surface roughness (0.8 and 1.2 nm, respectively) (**Figure 5.2**).

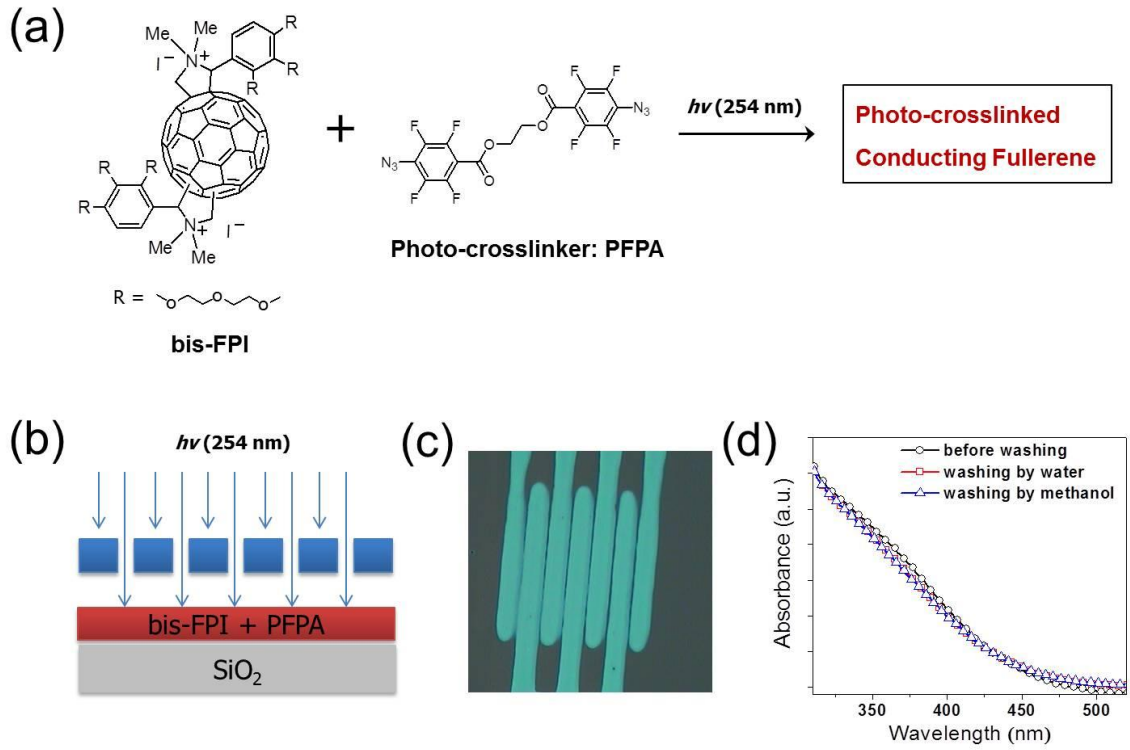

Figure 5.1. (a) The chemical structure of **bis-FPI** and photo-crosslinker (PFPA). (b) Schematic representation of the photo-patterning process using interdigitated cross-finger type photomask. (c) Optical microscope image of photo-patterned **bis-FPI**. The width of patterned cross-finger is ca. 90 μm. (d) Absorption spectra of **x^{post}-bis-FPI** films on ITO substrate before and after washing with water and methanol.

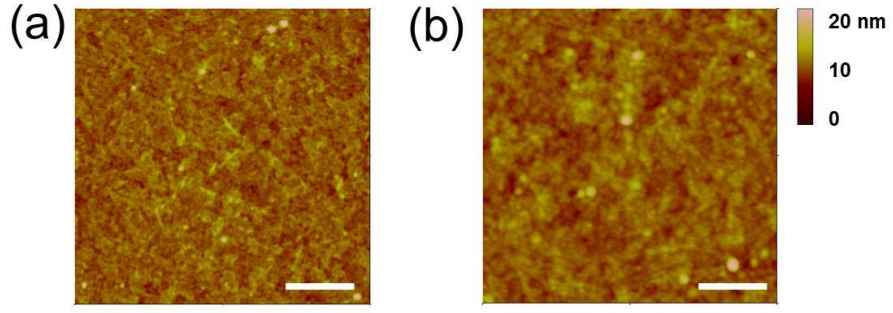

Figure 5.2. (a) AFM images of **x^{post}-bis-FPI** before washing and (b) after washing with methanol. The size of scale bar is 1 μm.

5.2.2 *Single-Junction Solar Cells*

Prior to demonstrating the feasibility of using **x^{post}-bis-FPI** for multilayered organic electronic devices such as tandem solar cells and double layered OTFTs, we investigated the crosslinking effect on the performance of PIDTT-DFQT:$PC_{71}BM$ based single-junction solar cells with the configuration of ITO/PEDOT:PSS/active layer/ETM/Ag (**Figure 5.3a**). **Figure 5.3b** shows the chemical structure of PIDTT-DFQT. Detailed optical and electrical properties of PIDTT-DFQT were reported elsewhere.[119] The device performances were tested under simulated AM 1.5G illumination at 100 mW cm^{-2}. **Figure 5.3c** and **Table 5.1** show the current-voltage characteristics of the devices and corresponding average photovoltaic parameters, respectively. As expected, the devices without ETM (w/o ETM) show poor device performances (*V*oc: 0.75 V, *J*sc: 9.88 mA cm^{-2}, FF: 0.49, and PCE: 3.65 %). However, the devices comprised of **x^{pre}-bis-FPI** show that this interlayer largely improves overall device performances (*V*oc: 0.92 V, *J*sc: 10.82 mA cm^{-2}, FF: 0.64, and PCE: 6.34 %). In general, these improvements are attributed to enhanced charge extraction efficiency, which is closely correlated with improved thermodynamic charge selectivity and the respective energy levels of the interlayers and electrodes.[117, 120] In addition, the kinetic charge selectivity, which is related to the charge transfer and surface recombination rate at the interlayer, also contributes to the enhanced charge extraction efficiency. In PSCs, a nonselective contact at the electrode causes severe recombination of charge carriers. Recombination at the interlayer/semiconductor interfaces occurs if the transport of charge carriers from the active layer to the interlayer is faster than the transport of carriers through the interlayer to the electrodes.[105] Recombination current at interfaces for electrons and holes is generally defined by the surface recombination rate S[112, 113, 121-123]

$$J_s = qS[n(0) - n_0(0)] + qS[p(d) - p_0(d)] \quad (1)$$

where q is the elementary charge, n_0 and p_0 are the equilibrium concentration of electrons and holes at the contacts, respectively. *n* and *p* are the charge carrier concentrations inside the device, respectively. In Equation (1), the anode location is defined as x = 0 and the cathode location is defined as x = *d*. In PSCs, introducing a thin conducting interlayer between the active layer and metal electrodes is a powerful method to reduce the surface recombination. This is conceptually analogous to the method applied in amorphous silicon solar cells where heavily doped Si is used as an interlayer to ensure Ohmic contacts and concurrently to suppress the diffusion of minority carriers at the highly doped region by back-surface-field.[124-126] An electric field generated at the interfaces between Si and heavily doped Si introduces a barrier to minority carriers diffusing to the wrong electrodes. In this regard, improved device performance by introducing **bis-FPI** interlayers is mainly attributed to the reduced contact resistance and concurrently decreased surface recombination rate by fast and selective extraction of electrons. The reduced surface recombination can be indicated by dark *J*-*V* characteristics. **Figure 5.3d** shows that introducing **bis-FPI** interlayers causes a strong reduction of the dark current. The relationship between the saturation dark current density (J_0) and *V*oc can be expressed as: $Voc = (nkT/q) \ln (Jsc/J_0)$, where *n*, *k*, *T*, and *q* are the diode ideality factor, Boltzman's constant, temperature, and elementary charge, respectively. Here, J_0 is closely correlated to the kinetics of charge generation/recombination. A large value of J_0 represents the recombination of charge carriers via diffusion of minority carriers towards the wrong electrodes, as is the case for our devices without ETMs. Thus, reduced recombination at the interfaces by introducing **bis-FPI** appears to account for the increase in *V*oc.

Interestingly, the device with **x^{post}-bis-FPI** shows superior PCE with increased *J*sc (12.04 mA cm^{-2}) compared to that of the devices with **x^{pre}-bis-FPI (**10.82 mA cm^{-2}) (**Figure 5.3c**).

Below, we show that this marked improvement in *J*sc is closely related to the increased electrical conductivity of **bis-FPI** after photo-crosslinking.

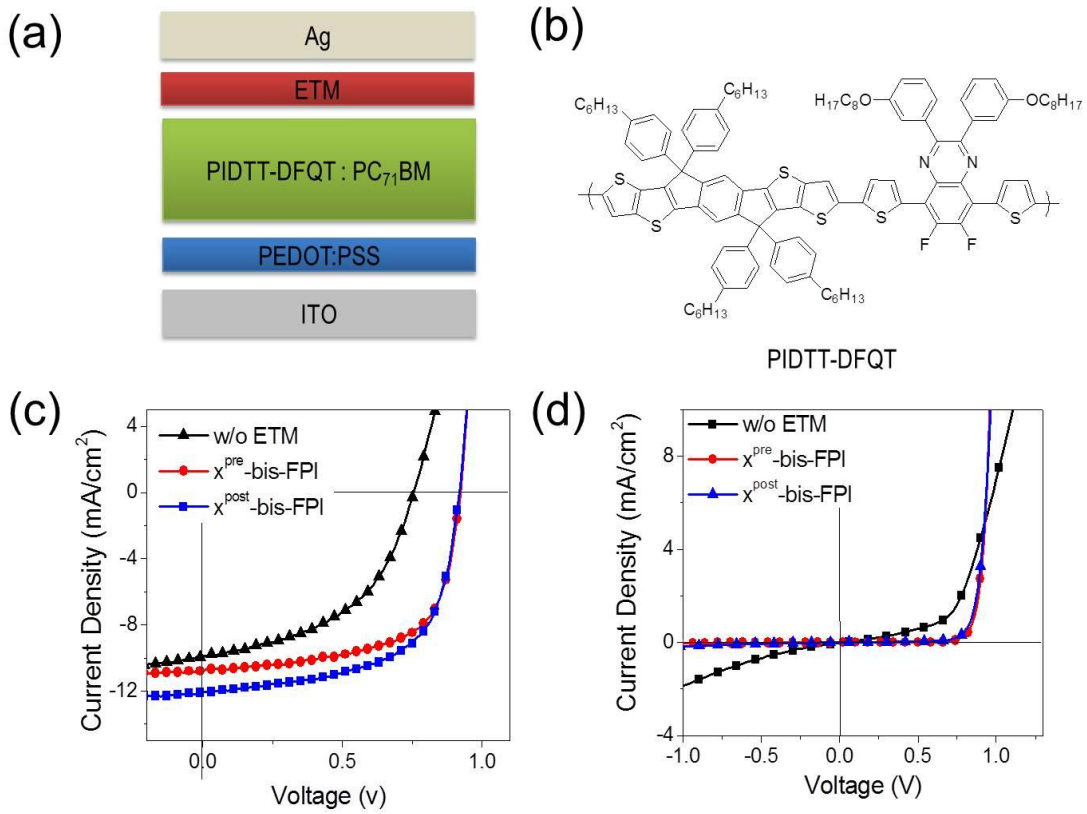

Figure 5.3. (a) Schematic representation of the device structure of PSCs. (b) The chemical structure of donor polymer (PIDTT-DFQT). (c) *J–V* characteristics of PCSs fabricated with different interlayers and (d) their dark *J-V* characteristics.

Table 5.1. Summary of device performances with different interlayers for single junction PSCs and tandem PSCs. Numbers in parentheses indicate the average values.

ETM	Voc [V]	Jsc [mA/cm^2]	FF	PCE [%]
w/o ETM	0.75 (0.74)	9.88 (9.80)	0.49 (0.47)	3.65 (3.41)
x^{pre}-bis-FPI	0.92 (0.92)	10.82 (10.75)	0.64 (0.63)	6.34 (6.23)
x^{post}-bis-FPI	0.92 (0.92)	12.04 (11.95)	0.62 (0.61)	6.82 (6.71)
tandem	1.47 (1.44)	8.71 (8.60)	0.57 (0.57)	7.30 (7.06)

5.2.3 *Electrical Properties and Energetics of crosslinked bis-FPI*

We observe that the photo-crosslinking of **bis-FPI** largely increases *J*sc (**Figure 5.3c** and **Table 5.1**). In order to investigate how the photo-crosslinking influences its electrical properties and energetics and to correlate these properties with the subsequent device performances, we performed conductivity measurement and X-ray photoelectron spectroscopy (XPS). The **x^{pre}-bis-FPI** and **x^{post}-bis-FPI** films were prepared by the same method used in the solar cell devices. The solutions were spin-coated on divinyltetramethylsiloxane-bis(benzocyclobutene) (BCB) doped Si/SiO_2 substrates as reported previously.[93, 117] After evaporating Au electrodes on top of the **bis-FPI** layer, two-terminal conductivity was measured using an Agilent 4155B semiconductor parameter analyzer. The electrical conductivity was calculated from the *I-V* curves. We observed that the photo-crosslinking of **bis-FPI** remarkably increased electrical conductivity from 2.5×10^{-9} to 1.4×10^{-5} S/cm (**Figure 5.4a**). A first insight into how photo-crosslinking impacts electrical conductivity can be obtained by comparing the conductivity of crosslinked and uncrosslinked **bis-FPI** upon increasing the concentration of the crosslinker

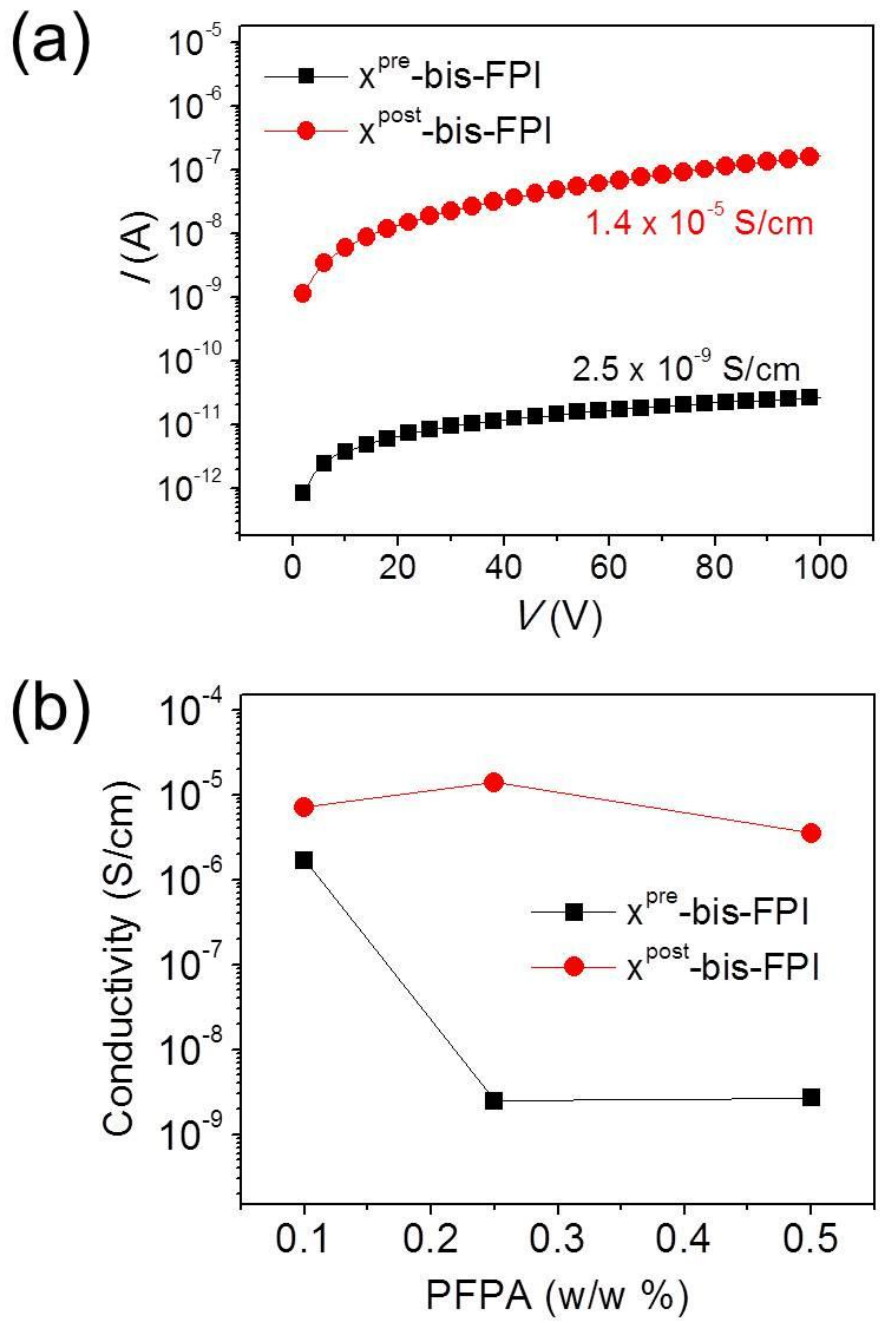

Figure 5.4. (a) Output current for **x^{pre}-bis-FPI** and **x^{post}-bis-FPI** devices. (b) Conductivity of **x^{pre}-bis-FPI** and **x^{post}-bis-FPI** upon increasing the concentration of the crosslinker (PFPA).

(**Figure 5.4b**). The conductivity of uncrosslinked **bis-FPI** decreases significantly with increasing PFPA concentrations, whereas the crosslinked **bis-FPI** does not. This rerult implies that PFPA can be a good bridge material for charge transport in crosslinked **bis-FPI** films. We assume that

the crosslinking of **bis-FPI** produce more ordered structures as confirmed from XRD spectra of the crosslinked and uncrosslinked **bis-FPI** films (**Figure 5.5**). In general, forming rigid and interconnected network structure could reduce electron-photonon interaction and reorganization energy, which can facilitate the charge transport process.[127] Therefore, we believe that increased electrical conductivity of crosslinked **bis-FPI**, mainly associated with structural evolution, facilitates the charge transport process and thus appears to account for the increase in *J*sc in our PSC devices.

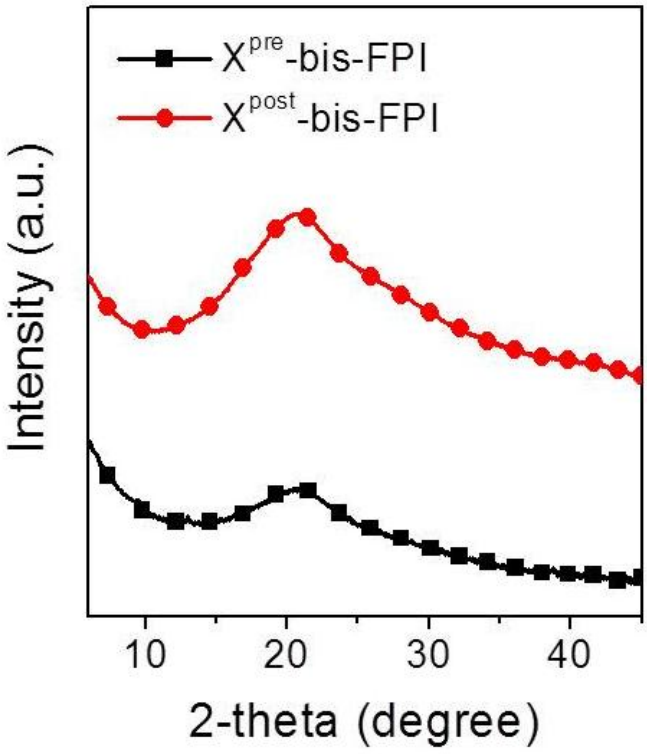

Figure 5.5. XRD spectra of **x^{pre}-bis-FPI** and **x^{post}-bis-FPI**.

It is important to align the work function of ETMs closely to the electron affinity of $PC_{71}BM$ to reduce the contact barrier for efficient electron extraction at the cathode. XPS measurements reveal that the work functions of uncrosslinked and crosslinked **bis-FPI** films

both have appropriate energy levels (~3.8 eV) which are close to the electron affinity of $PC_{71}BM$ (3.8 - 3.9 eV) (**Figure 5.6**). Note that the work functions of uncrosslinked and crosslinked **bis-FPI** films are almost the same. This is not surprising considering that most crosslinking likely occurs at the alkyl chain of **bis-FPI** due to the steric hindrance of bulky side groups, thereby preserving the conjugation of fullerene center.

The overall charge extraction efficiency with respect to the energetic and electrical properties of interlayers can be seen in the light intensity dependent photocurrent generation (**Figure 5.7**). If negligible bimolecular recombination occurs, *J*sc should scale linearly with the light intensity (i.e. $Jsc \propto I^{\alpha}$, and $\alpha = 1$). In our SC devices, we observed a sublinear scaling of the *J*sc with the light intensity, indicating the photogenerated charge carriers recombine during

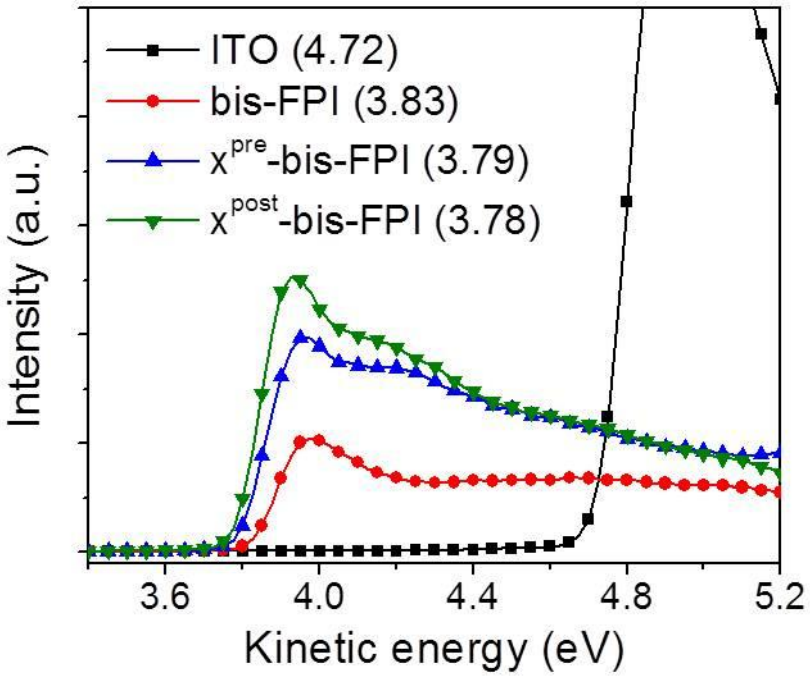

Figure 5.6. Secondary cutoffs of bare ITO, **bis-FPI**, **x^{pre}-bis-FPI**, and **x^{post}-bis-FPI** films on ITO substrate measured by XPS.

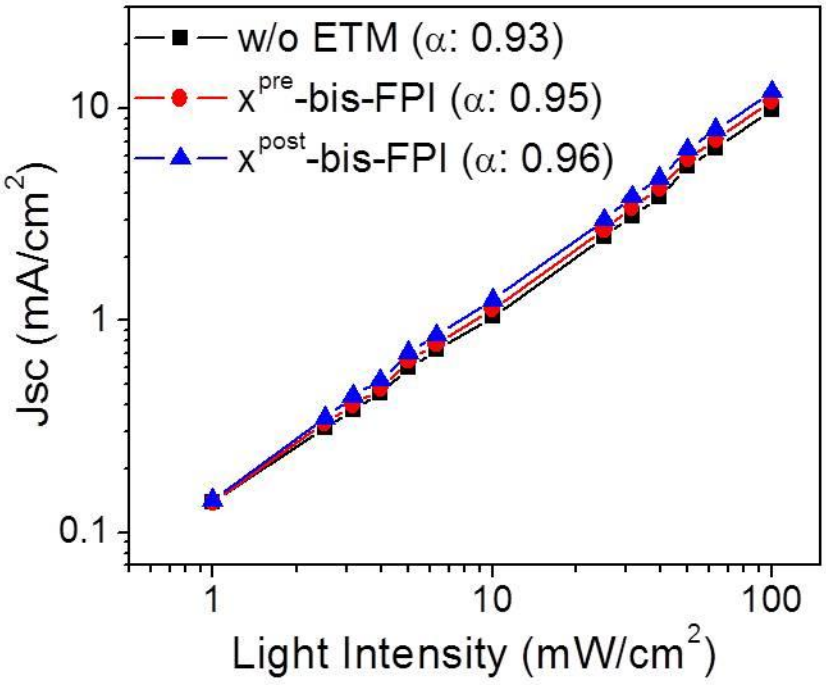

Figure 5.7. Light intensity dependent *J*sc for PSC devices with different interlayers.

charge transport and extraction process. The dependence of *J*sc on light intensity for the devices without ETM, with uncrosslinked **bis-FPI**, and crosslinked **bis-FPI** interlayer is shown in **Figure 5.7**, in which the power law (α) is 0.93, 0.95, and 0.96, respectively. This result shows that introducing crosslinked **bis-FPI** is an efficient method to reduce the surface recombination.

5.2.4 *Fabrication of Multilayered Organic Electronic Devices*

In addition to these encouraging results from single-junction solar cells, the ability to render **bis-FPI** insoluble and conductive without disrupting its energetic and electronic properties enables us to fabricate solution processed multilayer devices. As a proof-of-concept, we fabricated double-junction tandem SCs consisting of a PIDTT-DFQT:$PC_{61}BM$ front cell and PCPDT-FBT:$PC_{71}BM$ rear cell. These two active layers were connected in series by an

interconnection layer comprised of crosslinked **bis-FPI**/Ag/PEDOT:PSS. Owing to the key advantages of crosslinked **bis-FPI** as discussed, the tandem cell showed good device performances with a PCE of 7.3% (**Table 5.1** and **Figure 5.8**). More encouragingly, the *V*oc of the tandem cell is close to the sum of *V*oc of the each sub-cell, indicating the effectiveness of crosslinked **bis-FPI** as an interconnection layer (**Table 5.1**).

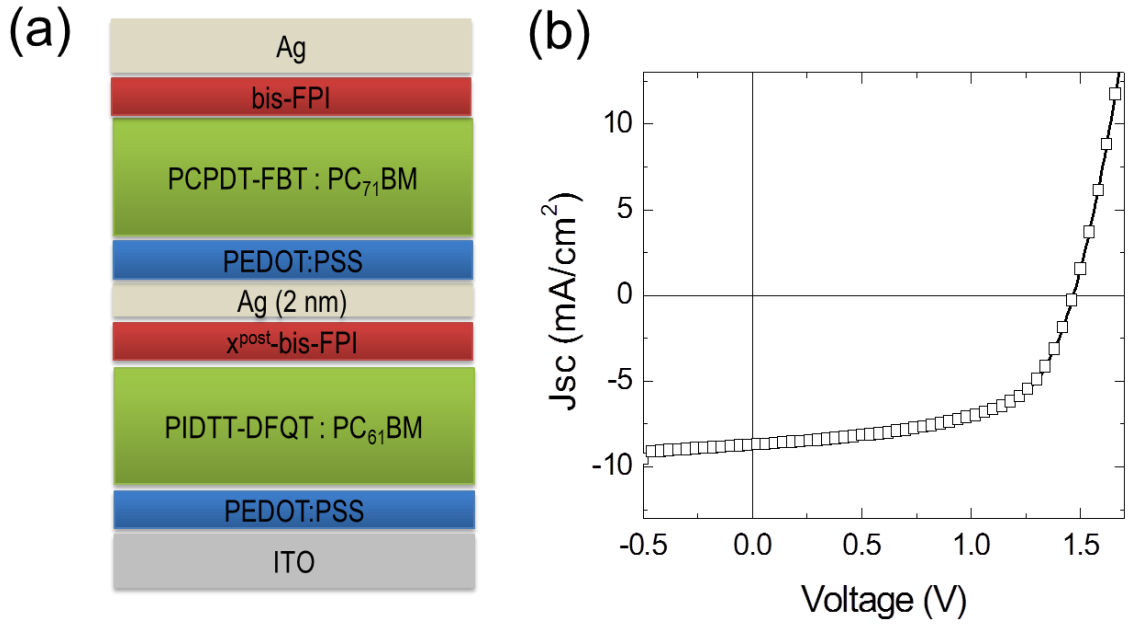

Figure 5.8. (a) Schematic representation of tandem PSCs and (b) corresponding *J-V* characteristics.

5.3 CONCLUSION

In conclusion, we have shown that photo-crosslinking of **bis-FPI** using azide crosslinker improves device performances in single junction PSCs owing to its appropriate kinetic and thermodynamic charge selectivity. By taking advantage of the properties of crosslinked **bis-FPI** such as excellent solvent resistance and electrical conductivity, we have investigated the feasibility of using crosslinked **bis-FPI** for multilayered organic electronic devices. Our results

show promise for the use of **bis-FPI** in highly ordered interdigitated optoelectronic devices based on all-organic photopatterned materials.

5.4 EXPERIMENTAL

Fabrication of single-junction solar cells: The device architecture of the conventional single-junction solar cell is shown in **Figure 5.3a**. ITO-coated glass substrates (15 Ω cm^{-2}) were cleaned stepwise in detergent, water, acetone, and isopropyl alcohol under ultrasonication for 10 min each and subsequently treated with air plasma for 5 min. A PEDOT:PSS layer (Baytron P VP A1 4083) was spin-coated onto the ITO surface. After annealing at 150 ℃ for 15 min in air, the substrates were transferred into an N_2-filled glove box. The active layer (ca. 80 nm) was spin-coated from the blend solutions of 5 mg mL^{-1} PIDTT-DFQT and 20 mg mL^{-1} $PC_{71}BM$ in either ODCB with 3% 1-chloronaphthalene (CN) by volume, followed by annealing at 120 ℃ for 5 min. The **bis-FPI** with the PFPA crosslinker was spin-coated at 5000 r.p.m. on the active layer, with the overall concentration at 2 mg mL^{-1}. The resulting film thickness was ~10 nm. After illumination under UV light for 20 minutes, an Ag layer (100 nm) was then deposited under high vacuum (< 10^{-6} torr) through a shadow mask.

Fabrication of tandem solar cells: The device architecture of the tandem solar cell is shown in **Figure 5.8a**. The fabrication procedure for the bottom cell was the same as the procedure for the single junction devices described previously. After introducing the **x^{post}-bis-FPI** layer, the modified PEDOT:PSS layer (ca. 70 nm) was then spin-coated from PEDOT:PSS solution (Clevious P VP A1 4083) diluted with equal volume of isopropyl alcohol and 0.2 wt.% of Zonyl FSO fluorosurfactant. After annealing at 130 ℃, the active layer for the back cell (ca. 100 nm) was spin-cast from the blend solution of 8 mg mL^{-1} PCPDT-FBT and 20 mg mL^{-1} $PC_{71}BM$ in trichlorobenzene. Subsequently, a **bis-FPI** layer (10 nm) was spin-coated from methanol solution.

After annealing at 110 ℃ for 5 minutes, an Ag layer (100 nm) was deposited under high vacuum (< 10^{-6} torr) through a shadow mask.

Chapter 6. MORPHOLOGY EVOLUTION BY CONTROLLING SOLVENT-SOLUTE INTERACTIONS USING A BINARY SOLVENT IN BULK HETEROJUNCTION SOLAR CELLS

6.1 INTRODUCTION

The morphology of the polymer/fullerene based BHJ solar cells is crucial for efficient charge separation and transport.[31, 32] A bicontinuous phase-separated morphology with domain size on the order of several nanometers to tens of nanometers, matching the exciton diffusion length, can be described as the favorable morphology. The morphology of the BHJ films are determined by the physical interaction among the donor polymers, fullerene acceptors, and the solvents used to process these materials. In other words, the morphology in terms of degree of phase separation and crystallinity (or aggregation) is intrinsically related to the thermodynamic miscibility between donor polymers and fullerene acceptors, solvent-solute interactions, and intrinsic crystallinity of the active materials. In addition, the final morphology of the BHJ films can be controlled by processing conditions.

Several strategies have been employed to control the morphology, like the selection of solvent,[32, 128] solvent annealing,[129] thermal annealing,[130] and slow growth.[131] Particularly, binary solvent systems or processing additives (such as 1,8-diiodooctane,[132] dimethyl sulfoxide,[133] dimethylformamide,[133] N-methyl-2-pyrrolidone,[134] 1-chloronathphalene,[134] chloroform,[132] etc.) have been introduced to control the morphology of the active layer. Among them, processing additives play an important role in adjusting crystallinity, solubility, and miscibility of the donor and acceptor components as well as the domain size and the local composition distribution at the D/A interface[128, 132]. Processing with additive which has preferential solubility to one of the components (such as diiodooctane for PCBM) can help develop morphology with well-ordered phases of the donor polymers and fullerene-rich aggregated domains, which gives rise to a drastic enhancement of device performance.[135] Although these results are very promising, there is still a strong need to understand better how binary solvents and processing additives influence

the crystallinity, domain size, and the phase separation of the active materials. Recently, we have developed a series of indacenodithiophene (IDT)-based ladder-type donor polymers by copolymerization with various acceptors.[136-138] Among these IDT-based polymers, PIDT-PhanQ has shown good device performance with PCE of ~6.2%.[138] However, further improvement of the device performance by controlling morphology using the aforementioned methods such as thermal annealing, solvent annealing, and additives have not been successful in the PIDT-PhanQ-based devices. From X-ray diffraction (XRD) and atomic force microscopy (AFM) study, PIDT-PhanQ seems to have very low levels of crystallinity and good miscibility with $PC_{71}BM$.

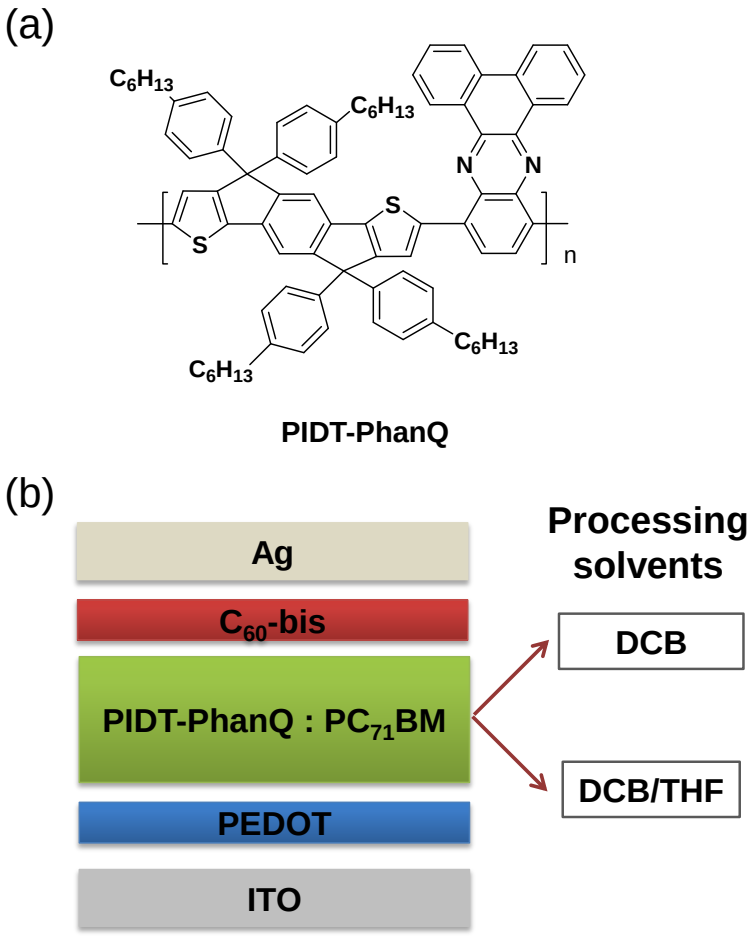

Figure 6.1 The chemical structure of PIDT-phanQ (a) and the device architecture (b).

It is well known, however, that such intimate mixing between the donor polymer and fullerene is undesirable for both charge separation and transport. This is because fullerene aggregates or cystalline domains act as electron percolation pathways, facilitating carrier transport and energetic sinks preventing charge recombination.[139, 140] The difficulties encountered in controlling the degree of crystallinity of PIDT-PhanQ prompted us to seek a new approach to create a more optimized phase-separated morphology by controlling the nanostructure of its counterpart, i.e. PCBM.

In this work, a DCB/THF binary solvent system was used to selectively control the aggregation of PCBM in a BHJ system. **Figure 6.1a** and **6.1b** show the chemical structure of PIDT-PhanQ and the device architecture of the BHJ SCs. We found that adding THF to the DCB solution of PIDT- PhanQ/$PC_{71}BM$ (30% by volume) drastically increases short circuit current density (J_{sc}) from 11.2 to 13.3 mA/cm^2, thus resulting in an increase of the PCE from 6.2 to 6.9%. The improved device performance is attributed to the morphological evolution of the active layer by fine-tuning the solvent-solute interaction. We used a combination of the Flory-Huggins interaction parameter and cohesive energy densities (CED) for PIDT-PhanQ and PCBM with different solvents to understand the phase separation process. The morphological evolution and corresponding device performance were further studied by AFM.

6.2 RESULTS AND DISCUSSION

6.2.1 *Solubility Parameters*

The key considerations for controlling morphology by using additives are the cohesive energy and the solubility parameter, as well as the relative aggregation or crystallization rates of the active materials. The cohesive energy of a liquid is the energy of vaporization, which is

equivalent to the total attractive forces by van der Waals interaction (δ_d), dipole interactions (δ_p), and hydrogen bonding (δ_h).[141] The solubility parameter (δ_t), developed by Hildebrand, is defined as the square root of the cohesive energy density (CED),[142]

$$\delta_t = (CED)^{1/2} = \left[\frac{\Delta E}{V_m}\right]^{1/2} = \left[\frac{\Delta H - RT}{V_m}\right]^{1/2} \qquad (1)$$

where ΔE = the energy change of vaporization, V_m = the molar volume, ΔH = enthalpy of vaporization, T = absolute temperature, and R = ideal gas constant. In order to predict the solvent effect on the morphology in terms of the enthalpic contribution to the free energy of mixing, the Flory-Huggins interaction parameter (χ_{12}) was employed. Traditionally, χ_{12} is estimated from the Hildebrand solubility parameters,[142]

$$\chi_{12} = V_1(\delta_2 - \delta_1)^2/RT \qquad (2)$$

where $\delta_{1=}$ the solubility parameters of the solvent, $\delta_{2=}$ the solubility parameters of the polymer, and V_1 = the solvent molar volume. The solubility parameters of the PIDT-PhanQ, $PC_{71}BM$, DCB, THF, and DCB/THF (30%), and their interaction parameters are listed in **Table 6.1**. The solubility parameters of DCB/THF (30%) were calculated by assuming a linear additive behavior.[141] Molar attraction constants of characteristic groups in PIDT-PhanQ were used to estimate the solubility parameter.[141] **Figure 6.2** shows a three-dimensional representation of each of the solubility parameters for the PIDT-PhanQ, $PC_{71}BM$, DCB, THF, and DCB/THF (30%). Note that there is a significant difference in the solubility parameters of THF (δ_d: 16.8, δ_p: 5.7, δ_h: 8.0 $MPa^{1/2}$) and $PC_{71}BM$ (δ_d: 20.2, δ_p: 5.4, δ_h: 4.5 $MPa^{1/2}$). In practice, the solubility of $PC_{71}BM$ in DCB and THF are 203 and 3.45 mg/ml, respectively.[143] This significant difference originates from the difference in δ_d and δ_h values. Note that the smaller value of χ_{12} indicates a stronger interaction between two materials. As we can see in **Table 6.1**, adding 30% of THF to DCB

increases the χ_{12} values of $PC_{71}BM$ from 0.03 to 0.06, indicating that THF effectively decreases the $PC_{71}BM$-solvent interaction. Meanwhile, the δ_d, δ_p, and δ_h values for THF are quite similar with PIDT-PhanQ (15.4, 5.3, and 8.1 $MPa^{1/2}$, respectively).

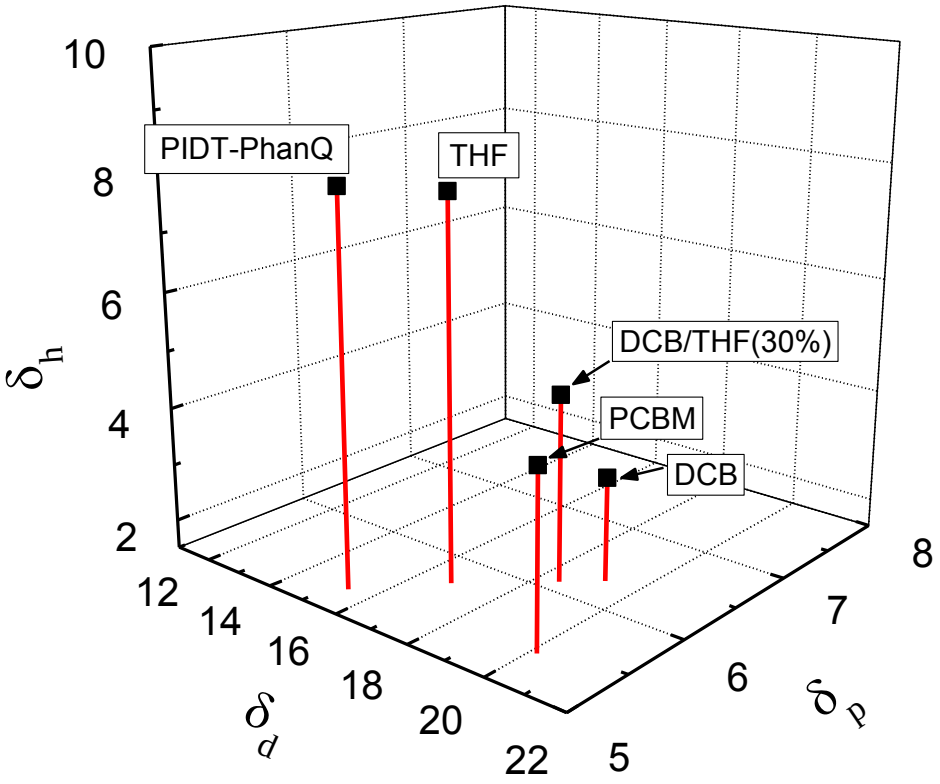

Figure 6.2 Solubility parameter diagram of PIDT-PhanQ, $PC_{71}BM$, DCB, THF, and DCB/THF (30%).

To check the solubility of PIDT-PhanQ (M_n: 82.4 kg/mol, PDI: 2.84), a 40 mg/ml solution of PIDT-PhanQ in THF was centrifuged at 10,000 rpm for 30 min. No residual precipitate was observed, indicating that THF is a good solvent for PIDT-PhanQ. It's worth noting that δ_h values between DCB (3.3 $MPa^{1/2}$) and PIDT-PhanQ (8.1 $MPa^{1/2}$) are quite different, even though DCB is also a good solvent for PIDT-PhanQ. This deviation can be rationalized by the presence of the 1,4-diazanaphthalene (quinoxaline) group, which contributes to hydrogen bonding and results in

a large δ_h. In this context, we hypothesized that the domain size of the PCBM and the degree of phase separation can be effectively controlled by using a particular solvent having selective solubility, facilitating the PCBM aggregation while maintaining the original structure of the donor polymer.

Table 6.1 Solubility parameters for PIDT-PhanQ, $PC_{71}BM$, DCB, THF, and DCB/THF (30%).

	Mol. vol. (cm^3/mol)	δ_d ($MPa^{1/2}$)	δ_p ($MPa^{1/2}$)	δ_h ($MPa^{1/2}$)	δ_t ($MPa^{1/2}$)	χ_{12} $PC_{71}BM$	χ_{12} PIDT-PhanQ
$PC_{71}BM$[a)]	607.3	20.2	5.4	4.5	21.3	-	-
PIDT-PhanQ	1184.6	15.4	5.3	8.1	18.2	-	-
DCB[a)]	112.8	19.2	6.3	3.3	20.5	0.03	0.24
THF[a)]	81.7	16.8	5.7	8.0	19.5	0.12	0.06
DCB/THF (30%)	103.5	18.5	6.1	4.7	20.2	0.06	0.17

[a)]Solubility parameters for $PC_{71}BM$, THF and DCB were taken from the literature.[141, 143]

6.2.2 *Solar Cell Performances*

Solar cell devices were fabricated with ITO/PEDOT:PSS/PIDT-PhanQ:$PC_{71}BM$/C60-bis/Ag stacks (**Figure 6.1**). The experimental details for ITO cleaning, plasma treatment, deposition of PEDOT:PSS and C_{60}-bis were described in elsewhere.[86] The active layers were deposited on top of the PEDOT:PSS layers by spin-coating the PIDT-PhanQ:$PC_{71}BM$ (1:3, weight ratio) solution (40 mg ml^{-1} in DCB with 30% of THF) and then annealed at 110 ℃ for 10 min in the glove box. A metal electrode (Ag) was then vacuum-deposited at a base pressure of 2 × 10^{-6} Torr at a rate of 2 Å s^{-1}. The *J–V* characteristics of the solar cells were tested under simulated AM 1.5G illumination at 100 mW/cm^2 in the glove box using a Keithley 2400 SMU

and an Oriel xenon lamp (450 W). The spectral photocurrent was measured in ambient atmosphere by monochromatic illumination using the 450W xenon lamp. The photocurrent was recorded with a lock-in-amplifier (Stanford Research Systems SR830). The Xe-lamp spectrum was measured with the NREL calibrated silicon photodiode.

Figure 6.3a shows the *J–V* characteristics of PIDT-PhanQ:$PC_{71}BM$ based solar cells fabricated using DCB and DCB/THF. A summary of the photovoltaic parameters for the devices is given in the inset table in **Figure 6.3a**. The PCE increases significantly from 6.2% to 6.9% by using the DCB/THF binary solvent. As shown in **Figure 5.3a** and the inset table, it is clear that these improvements are the result of increased J_{sc} values from 11.2 to 13.3 mA/cm^2. The decrease in *FF*, arising from a decrease in shunt resistance, was observed for the devices fabricated with THF. However, the V_{oc} of these devices showed the same value (0.87 V), indicating that adding THF do not affect the V_{oc}.

Generally, compared to J_{sc}, the V_{oc} is somewhat insensitive to the morphology evolution. This is due to the fact that V_{oc} is mainly determined by the energy level difference between the HOMO levels of donor materials and the LUMO levels of acceptor materials ($\Delta E_{\text{HOMO-LUMO}}$) as given in equation,[144]

$$V_{oc} = \frac{1}{q}\Delta E_{HOMO-LUMO} - \frac{nkT}{q} ln\left(\frac{\gamma N_A N_D}{J_{ph}}\right) \qquad (3)$$

where n= the diode ideality factor, k= the Boltzman's constant, T= temperature, q= elementary charge, γ= recombination rate, and N_A(N_D) = the effective density of states in donor (acceptor). In addition, the increase of J_{ph} in Eq. (3) with increased interface area by controlling morphology can be counterbalanced by increasing the recombination current. The corresponding EQE curves

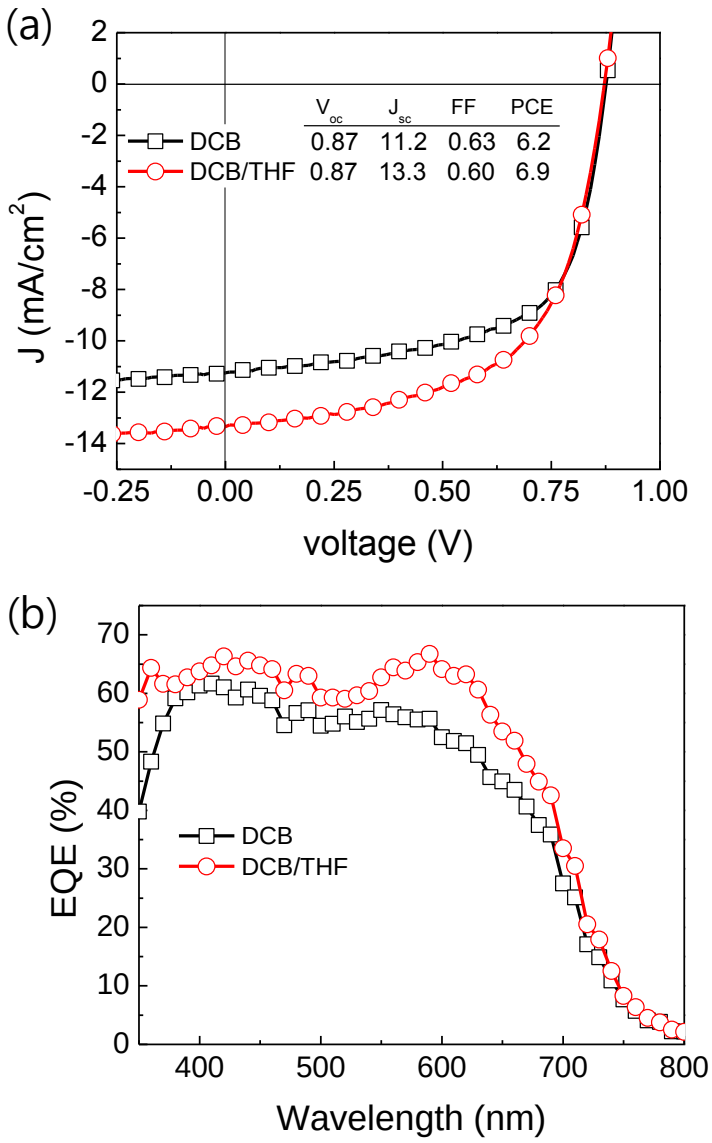

Figure 6.3 *J–V* characteristics (a) and EQE spectra (b) of PIDT-PhanQ:$PC_{71}BM$ devices processed from DCB (squares) and DCB/THF (circles).

of the devices fabricated by DCB and DCB/THF are shown in **Figure 6.4b**. The EQE curves reveal that the quantum yields of both PCBM and PIDT-PhanQ are increased effectively, indicating that aggregated clusters improve overall charge separation and transport in the BHJ layer.

6.2.3 *Morphological Evolution studied by AFM*

AFM was used to investigate how THF affects the morphology of the PIDT-PhanQ:$PC_{71}BM$ film. **Figure 6.4** shows the height and phase images of the films prepared with DCB only (**Figure 6.4a, b**) and 30% THF in DCB (**Figure 6.4c, d**). The topography images show that the surface roughness of the films with DCB only and 30% THF in DCB are 0.49 nm and 0.46 nm, respectively. All films are quite smooth, and there is no significant difference in the roughness value. However, the phase image of the films prepared with 30% of THF show a higher degree of aggregation with domain size of ≈ 20-30 nm , while relatively featureless

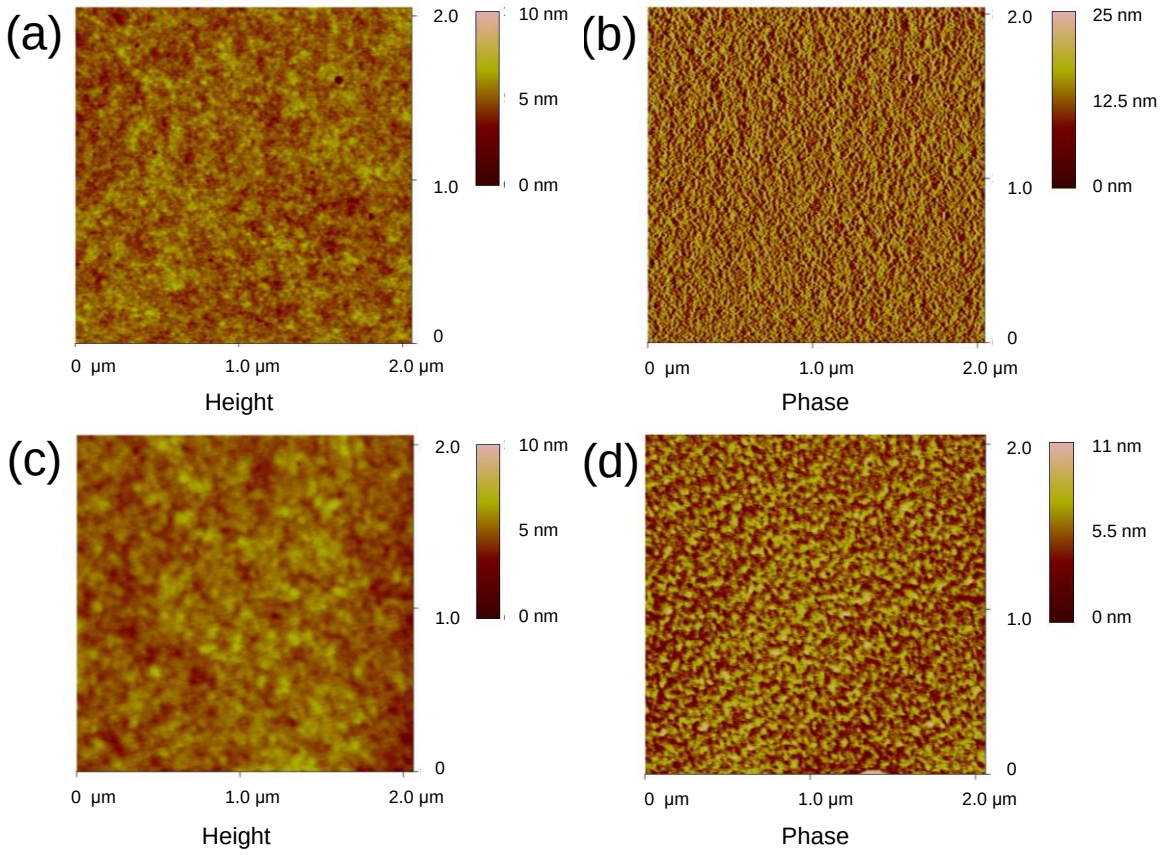

Figure 6.4 AFM topography and phase images (2 µm × 2 µm) of PIDT-PhanQ:$PC_{71}BM$ blended films processed by DCB (a, b) and DCB/THF (c, d).

morphology was observed in the films prepared with DCB due to the homogeneous mixing of the PIDT-phanQ and PC71BM. Although no detailed information could be obtained on the composition of the AFM images, we infer from solubility parameters that aggregation or crystallization originates primarily from the $PC_{71}BM$.

6.3 CONCLUSION

In conclusion, we have demonstrated that the morphology of the BHJ layer can be effectively controlled by using a particular solvent system having selective solubility. It facilitates PCBM aggregation, which generates a continuous percolation pathway for electrons resulting in improved charge transport properties. Our results showed that solubility parameters can be effectively used to control the morphology in BHJ systems. We believe that this study provides a general guideline on how to choose processing solvents through solvent-solute interaction analysis in order to obtain favorable film morphology for enhancing the performance of BHJ solar cells.

Chapter 7. HIGH-DIELECTRIC CONSTANT PHOTOACTIVE FUNCTIONAL SIDE-CHAIN POLYMERS FOR CONTROLLING CHARGE RECOMBIANTION DYNAMICS IN HETEROJUNCTION POLYMER-FULLERENE SOLAR CELLS

7.1 INTRODUCTION

Controlling charge generation and recombination dynamics in organic photovoltaics (OPV) is recognized as an important step towards improving power conversion efficiency.[145-149] It has long been realized that the low dielectric constants ($\varepsilon_r \sim 3$) of organic semiconductors result in stronger interactions between charge carriers than are typical in inorganic semiconductors where the dielectric constants are typically higher ($\varepsilon_r > 10$).

Heterojunction (HJ) architectures that pair appropriate excited state charge donors with complementary ground state charge acceptors are almost universally used to help split photo-generated exciton in order to achieve efficient photo-induced charge transfer in OPVs.[6-10] Nevertheless, photo-generated electrons in the acceptor phase and photo-generated holes in the donor phase still experience a strong Coulomb attraction to one another due to low charge screening in most low permittivity organic materials. This Coulombic attraction can lead to significant recombination losses.

Over the years, a number of authors have proposed modifications of the organic semiconductors' dielectric constant as a way to improve OPV performance by modulating a variety of factors linked to Coulombic interactions in the film. For instance, Koster *et al*. have argued that increasing the dielectric constant of the active layer in OPVs is attractive since this approach could in theory suppress bimolecular (non-geminate) recombination rates, mitigate space charge effects, and possibly decrease the exciton binding energy.[18]

Motivated by these considerations, a number of groups have synthesized organic semiconductors designed to have higher dielectric constants over different frequency bands. For instance, Breselge *et al*. reported that modifying the side-chains of poly-phenylene vinylene (PPV) derivatives using oligo(oxyethylene) groups increased the dielectric constant from 3.1 to

5.5.[150] However, the actual device performance of PEO-PPV was low, likely due to suboptimal morphology. Recently, Schwarz *et al*. reported that decreasing the Coulomb binding energy of the poly(*p*-phenylene) derivatives by increasing the effective conjugation length significantly influences charge separation dynamics.[5] Besides, Engel *et al*. demonstrated that introducing inorganic high dielectric materials such as TiO_2 and $SrTiO_3$ reduced the Coulomb interaction in organic semiconductors by effectively enhancing the permittivity in the organic matrix.[12]

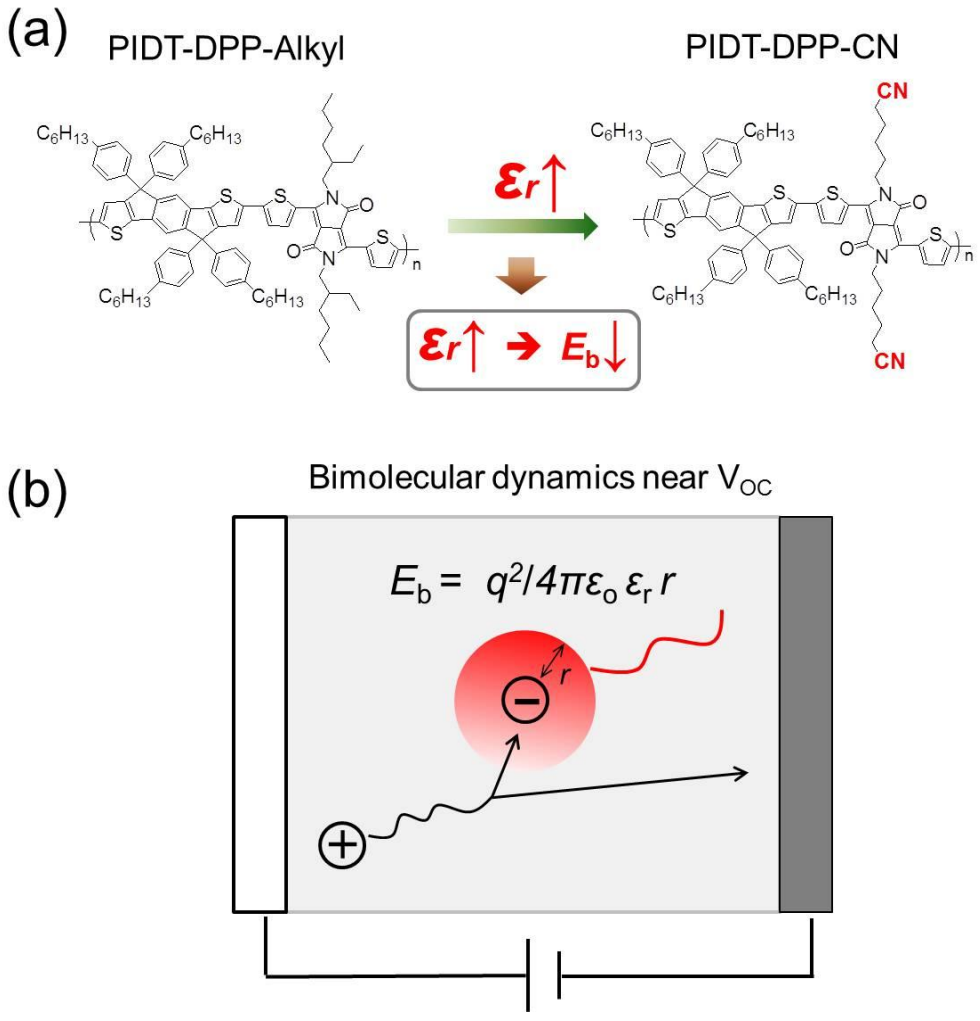

Figure 7.1 (a) The chemical structure of **PIDT-DPP-Alkyl** and **PIDT-DPP-CN**. (b) The schematic diagram of bimolecular dynamics representing the relationships among the dielectric constant, exciton binding energy, and charge recombination.

In general, defining compelling materials design strategies for controlling charge dynamics by tuning the dielectric properties of the active layer materials has proven to be challenging. While modifying dielectric constants remains very attractive in theory, in practice, verifying that the expected performance improvements accompany any changes in the dielectric constant has been more challenging. Here, we employ model polymers possessing non-ionic functional side-chains with conformationally labile polar moieties designed to tune dielectric properties to demonstrate that tailoring the polymer dielectric constant can be used to control recombination dynamics in OPVs. We introduce polar nitrile side-chains tethered to the electron deficient diketopyrrolopyrrole (DPP) unit of an indacenodithiophene (IDT)-based copolymer (**PIDT-DPP-CN**) to control the dielectric properties of this photoactive material compared to an analogous polymer with alkyl side-chains (**PIDT-DPP-Alkyl**) (**Figure 7.1a**). We show that the incorporation of nitrile side-chains both increases the dielectric constant of the donor material and suppresses non-geminate recombination losses in planar heterojunction solar cells, resulting in longer carrier lifetimes, improved open-circuit voltage (V_{OC}) and short-circuit current (J_{SC}).

Previously, we have shown that **PIDT-DPP-alkyl** and **PIDT-DPP-CN** have similar hole mobilities, frontier orbital energy levels, and optical absorption,[151] suggesting that the side-chain modification has a negligible impact on these properties. This behavior allows us to compare how the dielectric properties of these two materials influence charge dynamics irrespective of other characteristics. To exclude unintended morphological effects on device performance, which can be especially problematic when altering dielectric constants, we employed a bilayer heterojunction OPV architecture comprising ITO/PEDOT:PSS/PIDT-DPP-(alkyl or CN)/C_{60}/Ca/Al.

7.2 RESULTS AND DISCUSSION

7.2.1 *Fabrication and Characterization of Solar Cells*

ITO cleaning, plasma treatment, and deposition of PEDOT:PSS were described in previous chapters. The **PIDT-DPP-alkyl** and **PIDT-DPP-CN** films were deposited on top of the PEDOT:PSS layers by spin-coating of the polymer solution (5 mg/ml in DCB) to achieve the thickness of ca. 30 nm and then annealed at 110 ℃ for 10 min in a nitrogen filled glove box. After that, C_{60} (American Dye Source, Inc.) was thermally evaporated (0.5 Å /sec) to a thickness of ca. 40 nm. A metal electrode, Ca (20 nm)/Al (100 nm), was then deposited by thermal evaporation (3-4 Å /sec). The devices were tested under inert conditions with simulated AM 1.5G illumination at 100 mW/cm^2.

We employed a bilayer heterojunction OPV architecture to exclude unintended morphological effects on device performance. However, landing C_{60} has lots of thermal energy during evaporation and this thermal energy can facilitate diffusion for the first few molecules of C_{60} into the polymer layers. Therefore we believe that our solar cell devices are not perfect bilayer structure. However, it's worth noting that C_{60} layers are thermally stable once a certain size is reached which prevents subsequent diffusion. This is because the diffusion coefficients decrease significantly when they form clusters. The influence of thermal annealing on the device performance of bilayer solar cells made by thermally evaporated C_{60} and P3HT revealed that the diffusion of C_{60} into the polymer layer is negligible in room temperature, but C60 start to diffuse near 100 ℃.

Under illumination, **PIDT-DPP-CN** shows superior device performance with simultaneously improved V_{OC}, J_{SC}, and fill factor (*FF*), leading to an nearly doubled power conversion efficiency compared to that of the **PIDT-DPP-alkyl** device (**Figure 7.2** and **Table**

7.1). In the sections below, we show that these marked improvements in device performance are related to the increased dielectric constant of **PIDT-DPP-CN**.

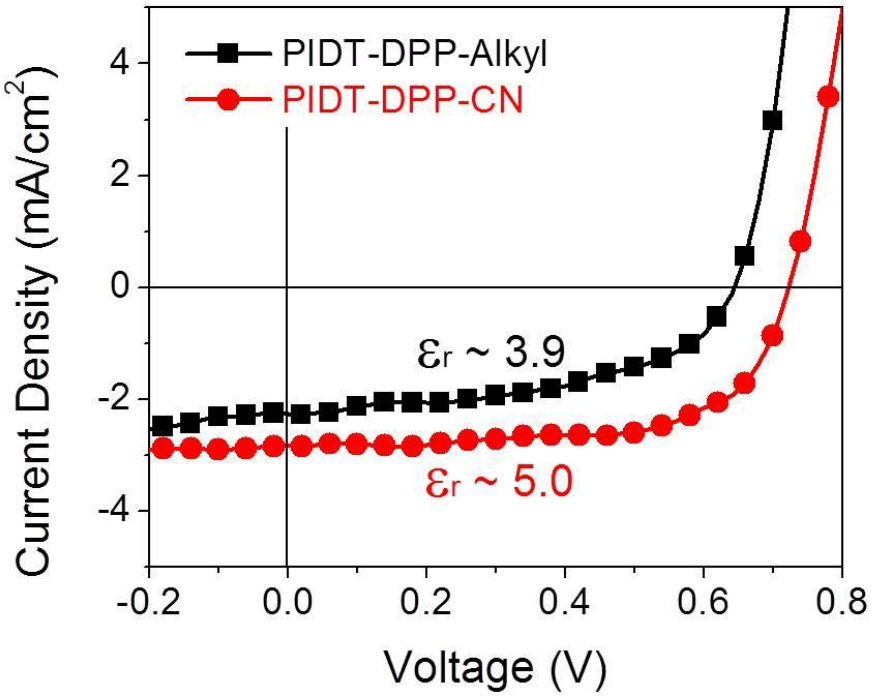

Figure 7.2 (a) *J-V* characteristics of PHJ SCs for **PIDT-DPP-alkyl**/C60 and **PIDT-DPP-CN**/C60 devices.

Table 7.1 Summary of device performance and photovoltage decay for PIDT-DPP-alkyl and PIDT-DPP-CN in PHJ devices.

Donor polymer	ε_r@ 1KHz	ΔE_{DA} [eV]	$V_{OC,Exp}$ [V]	$V_{OC,Calc}$, ε_r and NH [V]	$V_{OC,Calc}$, Only ε_r [V]	J_{SC} [mA/cm^2]	FF	PCE [%]	$\tau\Delta n$ [μs]
PIDT-DPP-Alkyl	3.5	1.67	0.63 ±0.01	0.63	0.63	2.40 ±0.07	0.47 ±0.05	0.72 ±0.05	15.2
PIDT-DPP-CN	5.0	1.67	0.71 ±0.01	0.71	0.67	3.00 ±0.09	0.68 ±0.03	1.44 ±0.09	72.6

7.2.2 *Dielectric Constant Measurement*

The introduction of the nitrile-functionalized side-chains to **PIDT-DPP-CN** increases its dielectric constant to ε_r ~5.0 compared to the alkyl derivative with ε_r ~3.5 (**Figure 7.3**). This is attractive for increasing Coulombic screening of charge carriers (**Figure 7.1b)** since the Coulomb attraction between the electron and hole is inversely proportional to ε_r.[29, 152]

$$E_b = \frac{q^2}{4\pi\varepsilon_0\varepsilon_r r_o} \qquad (1)$$

Here q, ε_o, ε_r, and r_o are the elementary charge, the permittivity of free space, the relative dielectric constant of the material, and the electron and hole separation, respectively. We measured the dielectric constants of **PIDT-DPP-alkyl** and **PIDT-DPP-CN** in MPM (metal-polymer-metal) structures using ITO and Al electrodes with thick polymer films (500-600 nm) by assuming a parallel plate capacitor ($C = \varepsilon_r\varepsilon_o A/d$, where C, A, and d are the measured capacitance, the active area of device, and the thickness of polymer films, respectively).

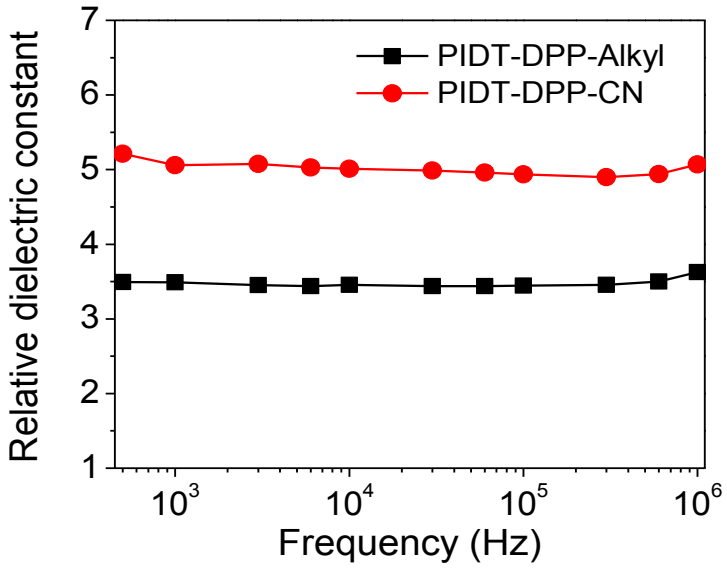

Figure 7.3 Dielectric constant with respect to frequency for **PIDT-DPP-alkyl** and **PIDT-DPP-CN**.

The dielectric constants that we extract from these measurements are plotted in **Figure 7.3** as a function of frequency. In this low frequency region, from 10^3-10^6 Hz, the relative dielectric constants of **PIDT-DPP-CN** and **PIDT-DPP-alkyl** are ~ 5.0 and 3.5, respectively.

As an additional control, we also measured the dielectric constants of our polymers in silicon-based MPOS (Metal-Polymer-SiO_2-Si) devices with p^+-Si/SiO_2/polymer/Al structure for thin films (~15 nm). The dielectric constant of our polymers shows similar value with MPM devices, and the dielectric constant of SiO_2 as a reference is in good aggreement with the accepted value[153] for a Al/SiO_2/p^+-Si MOS capacitor. **Figure 7.4a** shows the device structure (left) and corresponding electrical circuit diagram (right) of MPOS capacitors. In **Figure 7.4b** and **7.4c** we show that the capacitance-voltage (*C*-*V*) characteristics for **PIDT-DPP-CN** and **PIDT-DPP-alkyl** based capacitors using an LCR (Inductance, Capacitance, and Resistance) meter. **Figure 7.4d** shows corresponding dielectric constant of polymers with respect to frequency. **PIDT-DPP-CN** has a dielectric constant of ε_r ~ 4.7 at low frequency. This ε_r is higher than **PIDT-DPP-alkyl** (ε_r ~ 3.7). At negative bias in **Figure 7.4b** and 7**.4c** we see the capacitance of the polymer and the SiO_2 insulator due to accumulated holes from p-Si. At positive bias the capacitance drops as the semiconductor is depleted and then inverted. In the accumulation region, the maximum capacitance (C_{max}) corresponds to the series combination of the polymer layer (C_{pol}) and the SiO_2 layer (C_{SiO2}), *i.e.*,

$$\frac{1}{C_{max}} = \frac{1}{C_{pol}} + \frac{1}{C_{SiO2}} \qquad (2)$$

where $C_{SiO2} = \varepsilon_{SiO2}\varepsilon_o A/d_{SiO2}$ and $C_{pol} = \varepsilon_{pol}\varepsilon_o A/d_{pol}$. Here, A, d, ε_{SiO2} and ε_{pol} are the active area of the device (3.14×10^{-2} cm^2), thickness, relative dielectric constants of SiO_2 and polymer,

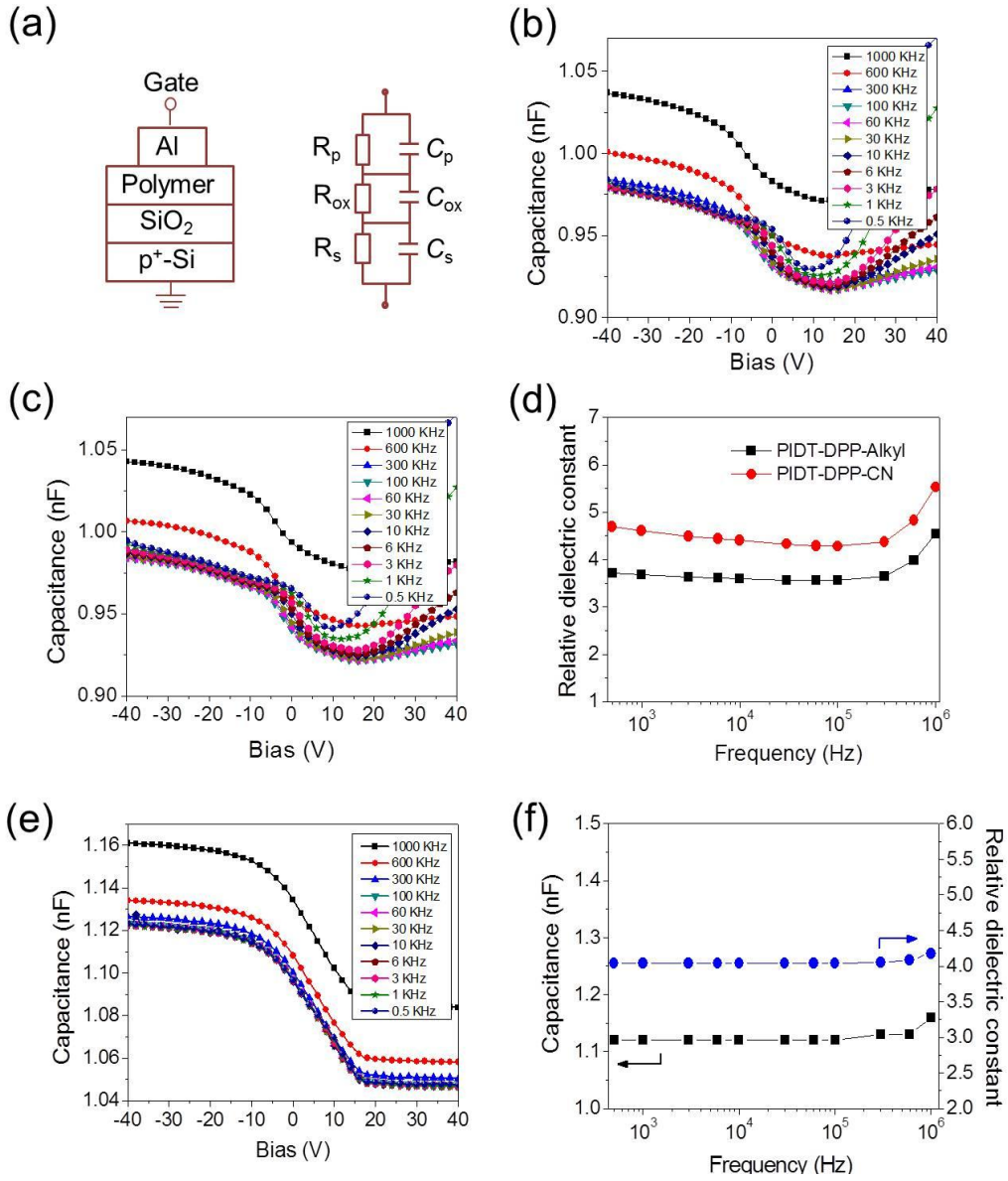

Figure 7.4. (a) The device structure (left) and corresponding electrical circuit diagram (right) of MPOS capacitors (p^+-Si/SiO_2/polymer/Al). (b) Capacitance-Voltage characteristics of **PIDT-DPP-alkyl** and (c) **PIDT-DPP-CN**, and (d) corresponding dielectric constants with respect to frequency. (e) Capacitance-Voltage characteristics of MOS capacitors for bare p^+-Si/SiO_2/Al devices, and (f) corresponding dielectric constant and capacitance with respect to frequency.

respectively, while ε_o represents the permittivity of free space. **Figure 7.4e** and 7**.4f** show the capacitance-voltage characteristics of MOS capacitors for p^+-Si/SiO_2/Al devices and corresponding dielectric constant with respect to frequency, respectively. The dielectric constant of SiO_2 of 4.0 that we calculate in the range of 0.5 KHz to 1000 KHz (**Figure 7.4f**) is in good agreement with the accepted value in the accumulation region for a Al/SiO_2/p^+-Si MOS capacitor.

7.2.3 *The Energy of the Interfacial Charge Transfer and Interfacial Dipoles*

Based on our observation that the V_{OC} produced by the **PIDT-DPP-CN** device is 80 mV larger than that of the **PIDT-DPP-alkyl** device (See **Table 7.1**), one might anticipate the energy of the intermolecular charge transfer (CT) state formed at the **PIDT-DPP-CN**/C_{60} interface to be larger than that formed at the **PIDT-DPP-alkyl**/C_{60} interface.[154] However, as shown in **Figure 7.5a**, we directly measured the energy of these CT states using low temperature electroluminescence (EL) and found them to be nearly identical. By cooling the device to 80K we are able to largely suppress neutral singlet exciton emission from either of the polymers (luminescence peak near 840 nm) and the fullerene (luminescence peak near 720 nm in **Figure 7.5b**). Instead, we observed EL from interfacial charge transfer states in both devices (CT EL peak ca. 1000 nm). The energies of these Gaussian-like CT state EL peaks in **Figure 7.5** are nearly identical, indicating that there is no discernible difference in the energy of the CT state formed at the **PIDT-DPP-alkyl**/C_{60} interface compared to the **PIDT-DPP-CN**/C_{60} interface. We interpret this result as indicating that, despite having different low-frequency (10^3-10^6 Hz) dielectric constants as measured by impedance spectroscopy, the dielectric constants of these materials at ~GHz frequencies (which might be expected to change the energy of the CT states with sub-ns lifetimes) are very similar.

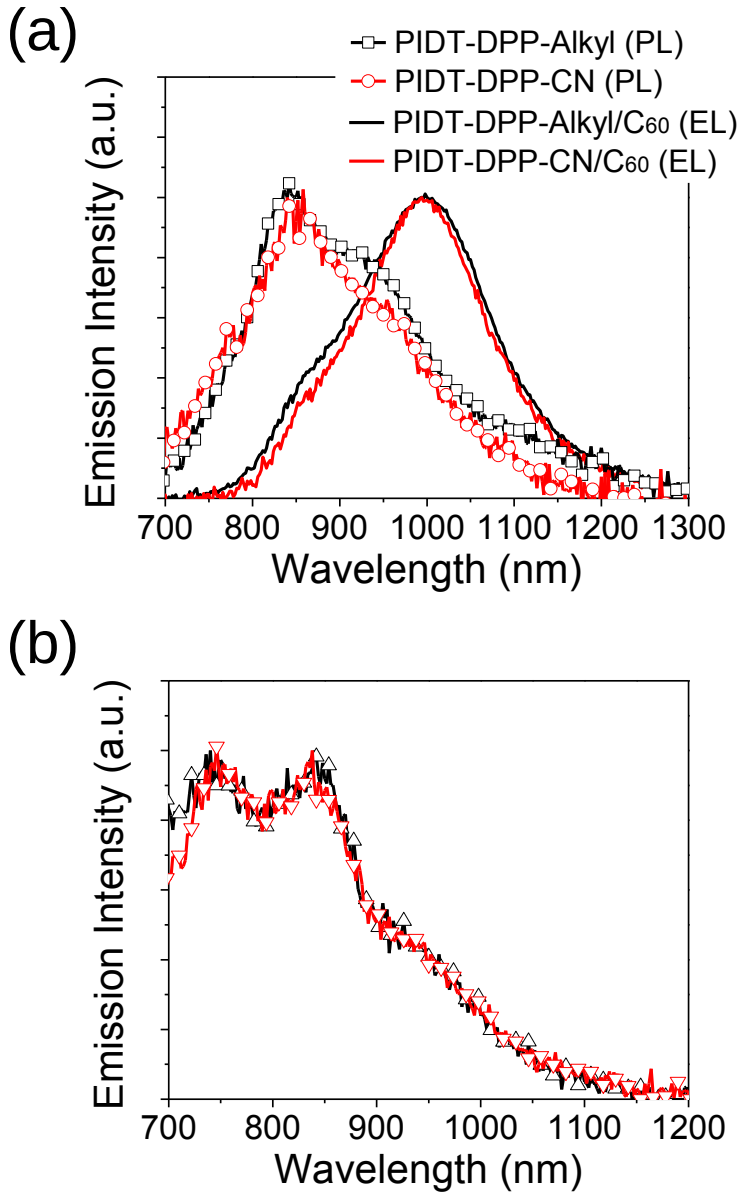

Figure 7.5. (a) The CT state EL bands for PIDT-DPP-alkyl/C60 (black line) and PIDT-DPP-CN/C60 (red line) devices are at nearly identical energies (peak at ca. 1000 nm). The shoulder at 850 nm is polymer fluorescence based on PL spectra for neat PIDT-DPP-alkyl (□) and PIDT-DPP-CN (○). (b) PL from **PIDT-DPP-alkyl**/C_{60} (black △) and **PIDT-DPP-CN**/C_{60} (red ▽) devices.

One might also anticipate that altering the strength and direction of dipoles at the interface between the donor and the acceptor could significantly change the V_{OC}, for example, by using surface-segregated monolayers of fluorinated interface modifiers.[20] However, we exclude this possibility based on the results of sum-frequency-generation (SFG) spectroscopy.

Figure 7.6 shows the SFG spectra in the range from 2150 to 2300 cm^{-1} for **PIDT-DPP-Alkyl** and **PIDT-DPP-CN** prepared on 120 nm Au coated Si-wafers. We do not detect an SFG signal from the nitrile groups in **PIDT-DPP-CN**. Instead we detect only a strong non-resonant SFG background signal from electronic transitions within the Au substrate. This is not surprising considering that our **PIDT-DPP-CN** polymer is symmetrically substituted with nitrile groups, leading to a net cancelation of any possible surface dipole compared to the alkyl derivative.

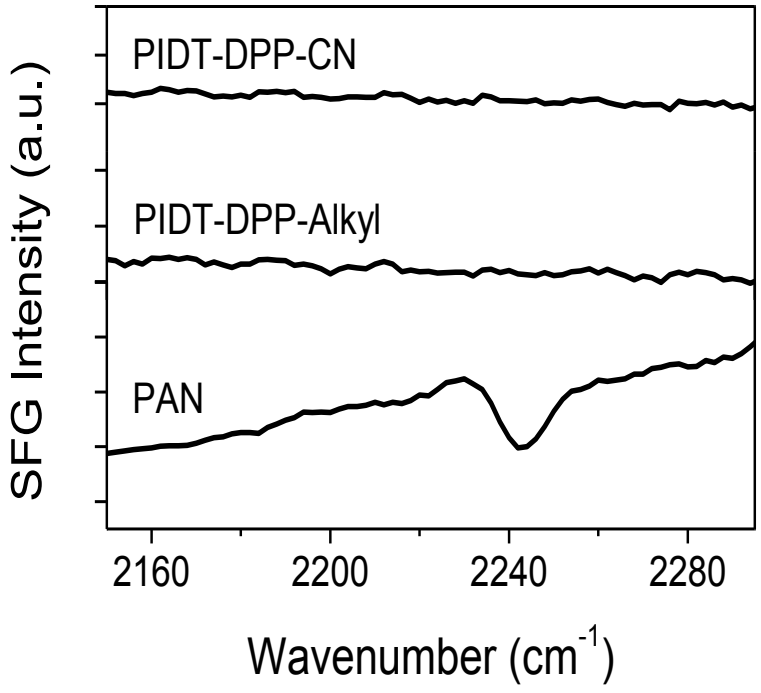

Figure 7.6. SFG spectra of **PIDT-DPP-Alkyl**, **PIDT-DPP-CN**, and polyacrylonitrile (PAN).

On the other hand, significant dipole effects on polymer properties have been observed by asymmetrically functionalizing polymers with alternating polar and non-polar side-chains.[155]

As a control experiment to confirm the sensitivity of our SFG instrumentation to the presence of asymmetrically oriented nitrile side chains, we performed SFG measurements on polyacrylonitrile (PAN) with asymmetrically functionalized nitrile groups.[156] In this case, we observe a significant resonant SFG signal at 2242 cm^{-1} associated with the nitrile groups.[156] This PAN resonance appears as a dip in the non-resonant signal, indicating the transition dipole moment is oriented away from the surface for PAN.[157] Since we observe a significant nitrile contribution to the SFG signal in our PAN control but not in our **PIDT-DPP-CN** samples we conclude that the nitrile groups are isotropically arranged at the **PIDT-DPP-CN** surface. These data suggest a negligible difference between the interfacial dipole in our **PIDT-DPP-CN** devices compared to our **PIDT-DPP-alkyl** devices.

Since the CT state energy is identical for our **PIDT-DPP-alkyl** and **PIDT-DPP-CN** devices and we do not observe significant differences in surface dipole, we hypothesize that the increase in V_{OC} for **PIDT-DPP-CN** arises due to higher carrier densities associated with slower charge recombination at the donor/acceptor (D/A) interface. To test this hypothesis we performed transient photovoltage (TPV) measurements and found that indeed the charge recombination rate is substantially reduced in the **PIDT-DPP-CN**/C_{60} device in contrast to the faster charge recombination rates we measure in our **PIDT-DPP-alkyl**/C_{60} devices.

7.2.4 *Non-Geminate Recombination Rates from TPV/CE*

We used TPV[146, 147, 158] and charge extraction (CE) measurements to measure the rate of non-geminate recombination of carriers near V_{OC}. The TPV and CE techniques are described in the literature[147] and the experimental section. Briefly, the device is illuminated with a steady-state

white light bias at open-circuit conditions while light from a second pulsed LED induces a small voltage perturbation and the decay of this voltage transient is recorded on a digital oscilloscope. **Figure 7.7a** and **7.7b** show the TPV decays and charge carrier lifetimes ($\tau_{\Delta n}$) as a function of charge carrier density (n) for both polymer, respectively.

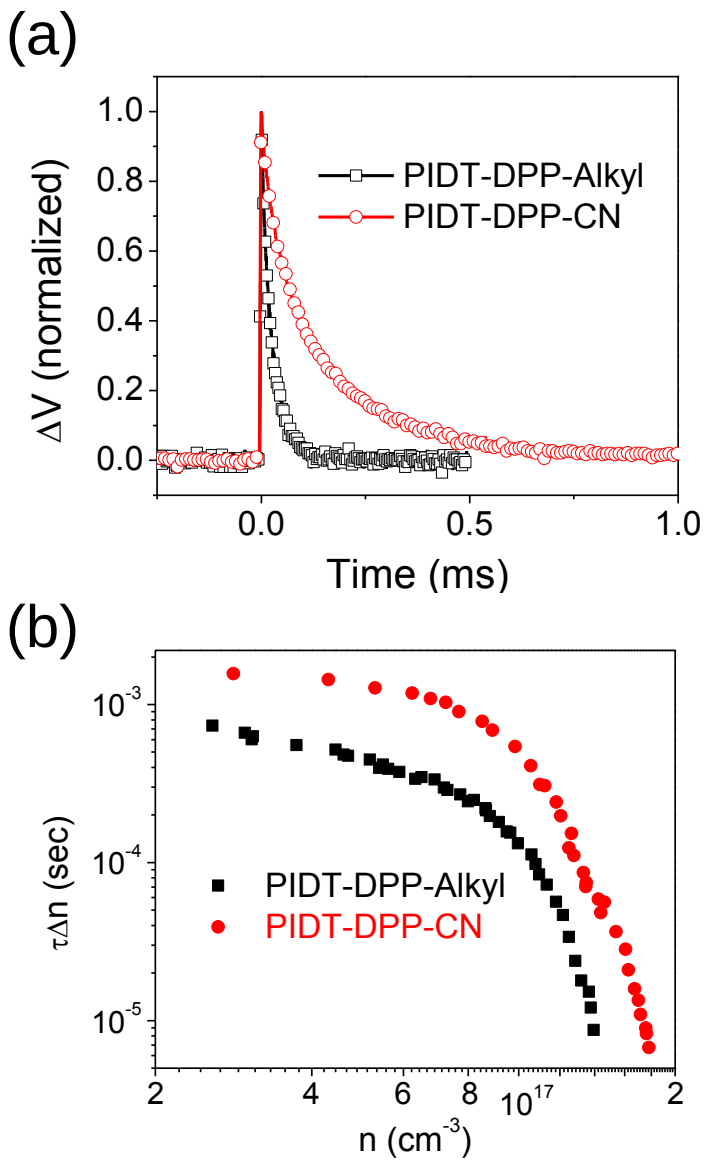

Figure 7.7. (a) Normalized TPV decays for **PIDT-DPP-alkyl**/C_{60} and **PIDT-DPP-CN**/C_{60} devices at a charge carrier density of ~1.3 × 10^{17} cm^{-3}. (b) Comparison of charge carrier lifetime ($\tau_{\Delta n}$) for both polymer devices as a function of charge carrier density (n).

The voltage decay times ($\tau_{\Delta n}$) we measure by TPV[147, 159] in **Figure 7.7a** are roughly five times longer for **PIDT-DPP-CN** devices ($\tau_{\Delta n}$ = 73 μs) than **PIDT-DPP-alkyl** devices ($\tau_{\Delta n}$ = 15 μs) at equivalent charge densities (n = 1.3×10^{17}), in good qualitative agreement with the hypothesis that the larger V_{OC} in our **PIDT-DPP-CN** devices is correlated with slower charge recombination rates. Furthermore, the timescales associated with non-geminate recombination (tens of microseconds) are in the range where we might expect the measured differences in kHz-MHz frequency dielectric constants to show differences between the polymers.

7.2.5 *Detailed Balance Prediction of V_{OC}*

To perform a more quantitative assesment of the role of increased carrier lifetimes on the change in V_{OC} we use the detailed balance formula from Forrest and co-workers:[160]

$$qV_{oc} = \Delta E_{DA} - n_A k_B T ln\left(\frac{k_{fppr}}{k_{dppd}}\frac{k_{rec}N_H H_A}{\frac{J_x}{a_o}}\right) \qquad (3)$$

In Eq. 3 k_{rec} is the bimolecular recombination rate, k_{ppr} and k_{ppd} are respectively the rate constants for polaron pair (synonymous with CT state) recombination and dissociation, N_H is the HOMO edge density of states on the donor side of the junction, H_A is the defect density on the acceptor side, J_X is the exciton flux reaching the donor/acceptor interface, and a_o is the spatial extent of the polaron pair, ΔE_{DA} is the energy offset at the D/A interface, n_A is an ideality factor,[25, 26] k_b is Boltzmann's constant, and T is temperature.

If we fix the parameters in Eq. 3, and decrease the carrier recombination rate at V_{OC} by the amount measured in our TPV experiment we calculate V_{OC} = 0.70 V for **PIDT-DPP-CN** devices with $\tau_{\Delta n}$ = 73 μs and V_{OC} = 0.63 V for **PIDT-DPP-alkyl** devices with $\tau_{\Delta n}$ = 15 μs. Both of these calculated values from Eq. 3 using the kinetics we measure by TPV for the charge carrier lifetimes are in agreement with the experimental V_{OC} values in **Table 7.1**.

From Eq. 3 we can also estimate the fractional increase in the charge carrier lifetime resulting from increasing the dielectric constant of the polymer. According to the Langevin expression[29, 30] $k_{rec} = q(\mu_e + \mu_h)/\varepsilon_o \varepsilon_r$, where μ_e and μ_h are the average charge mobility of electrons and holes, respectively at the donor acceptor interface. We predict V_{OC} values using Eq. 3 by substituting the ε_r values we measured here and the μ_h of **PIDT-DPP-alkyl** (ε_r = 3.5 and μ_h = 0.015 $cm^2/V \cdot s$) and **PIDT-DPP-CN** (ε_r = 5.0 and μ_h = 0.011 $cm^2/V \cdot s$) that we reported previously.[151] As shown in **Table 6.1** the V_{OC} we calculate for **PIDT-DPP-alkyl** /C_{60} is $V_{OC,Calc}$ = 0.63 V and that we obtain experimentally is $V_{OC,Exp}$ = 0.63 V. Similarly, for the **PIDT-DPP-CN**/C_{60} devices $V_{OC,Calc}$ is 0.67 V and $V_{OC,Exp}$ is 0.71 V. These values indicate that more than half of the increase in V_{OC} resulting from the longer $\tau_{\Delta n}$ can be directly attributed to the higher ε_r of **PIDT-DPP-CN**.

From our EL data we know the CT state energies are invariant and from our SFG measurements we can neglect differences in interfacial dipoles. Based on Eq. 3 we postulate that the remainder of the increase in V_{OC} is due to a decrease in either the interface trap state density, the band-edge density of states,[161] or some combination of both. The $V_{OC,Calc}$ values in **Table 7.1** calculated from Eq. 3 are in excellent agreement with the experimental values after accounting for such effects in an *ad hoc* fashion (e.g. decreasing the trap state density, *H*, from 3.7×10^{18} cm^{-3} in **PIDT-DPP-alkyl** to 1.7×10^{18} cm^{-3} in **PIDT-DPP-CN**).

We further note that the J_{SC} of **PIDT-DPP-CN** is slightly higher than that of the **PIDT-DPP-alkyl**. Observed enhancement in the J_{SC} is also expected to be related to a change in geminate recombination losses and exciton dissociation efficiency. Herein we do not intend to cover a detailed analysis of geminate recombination because of limited experimental setup. The increased *FF* also correlated with exciton dissociation and recombination dynamics.

7.3 CONCLUSION

We have shown that photoactive polymers possessing nitrile side-chains show a 40% increase in dielectric constant at frequencies from 10^3-10^6 Hz. Bilayer heterojunctions made with the high dielectric polymer **PIDT-DPP-CN** show improvements in V_{OC}, FF, and J_{SC}. EL and SFG experiments suggest that these increases are most likely not due to changes in the energy of the CT state or changes in interface dipoles, while TPV measurements show that these improvements in device performance appear to be linked to suppressed non-geminate charge recombination rates. To the best of our knowledge this is the first practical report showing that the dielectric properties of the photoactive materials in polymers/fullerene solar cells can be rationally tuned using non-ionic polar side-chains to demonstrate the expected control over charge dynamics that has long been predicted. We believe this finding provides new incentive to pursue molecular design strategies that seek to optimize recombination kinetics in OPVs based on control of local molecular dielectric properties.

7.4 EXPERIMENTAL

C-V Characteristics:

MOS or MPOS capacitors were fabricated by evaporating Al through a shadow mask onto polymer films that were deposited by spin-coating of polymer solution in DCB onto p^+-Si/ SiO_2 substrates. Polymer films were annealed for 10 minutes at 110 ˚C before metal deposition. *C-V* measurements were performed using a HP 4284A LCR meter by sweeping the voltage from -40V to +40V at room temperature, with ramping rate of 0.1 V/s and 25 mV of oscillator levels. A custom-built dual probe station probes from Sigma Corporation was connected to the electrodes for the measurements.

Electroluminescence (EL) measurement:

Thin film electroluminescence (EL) measurements were performed under dynamic vacuum on the same devices used for TPV measurements. EL spectra were collected using a home built spectrometer comprising an Acton dual-grating imaging monochromatic (Acton SP-2150i) and a dual-band Si/InGaAs photodetector (Thorlabs DSD2). The EL signal was electrically modulated to generate square wave emission (100 Hz) using a homebuilt amplifier circuit driven by a function generator and a DC power supply. EL emission intensity at each wavelength was monitored by lock-in detection (SR830 lock-in amplifier) referenced to the function generator after amplifying the signal by 500 pA/V (SR570 current preamplifier). All emission spectra were spectrally corrected for instrument response using a calibrated light source (Ocean Optics). Photoluminescence data were recorded using the same experimental setup using lock-in detection referenced to the drive signal used to power a frequency modulated Luxeon Rebel Royal-Blue LED.

Vibrational SFG spectroscopy:

The second-order nonlinear optical processes involved in producing SFG signal cannot be generated in isotropic media or within systems with inversion symmetry,[162] making SFG spectroscopy useful for detecting surface dipoles. During the SFG experiment, a visible pulse overlaps in space with a tunable IR pulse to generate a coherent sum-frequency signal of the two incident beams. Scanning the IR beam over IR and Raman active resonances enhances the SFG signal, resulting in a vibrational spectrum from asymmetry on the surface of the sample.[163]

SFG intensities have been acquired with a commercial SFG spectrometer (EKSPLA, Lithuania) utilizing 35 ps light pulses at a repetition rate of 50 Hz. Visible (532 nm, 200 μJ, p-polarized) and tunable IR beams (150 μJ, p-polarized) were overlapped at the sample spatially and temporally with incidence angles of 67° and 55°, respectively. Plotted SFG intensities (p-

polarized) were normalized by a reference SFG line using a ZnSe crystal. To avoid damage of the 120 nm Au coated Si-wafer, all beams were defocussed to a diameter of about 2mm at the sample stage.

SFG spectra were recorded in between 2100 and 2300 cm^{-1} to capture CN vibrations in the polymer side chain. We also recorded spectra in between 2800 and 3100 cm^{-1}, but due to the complex nature of diverse contributions from alkyl chains and potentially the main polymer backbone, only rather broad signals were detected. Therefore, we only focus on spectra obtained from the cyano group in the side chain.

Transient photovoltage (TPV) and Charge extraction (CE) measurements:

Both TPV and CE measurements were performed on devices under vacuum (typically ~20 mTorr) in a homebuilt test chamber. In the TPV measurement, a Royal-Blue Rebel 447.5nm LED (Luxeon Star LXML-PR01-0425) was pulsed (30 Hz, 4 μs width, 20 ns edge) using a homebuilt LED driver circuit and Agilent 33210A 10 MHz Function/Arbitrary waveform generator to create small (~20 mV) voltage perturbations that were measured by an oscilloscope (Textronix TDS 2024B). The device was held under open-circuit by a Bridgelux BXRA-56C9000-J white LED that was controlled by custom LabVIEW software and a TTI Instruments (CPX400SA) power supply. The decaying voltage transients were collected at various white light intensities, and the decay lifetime, $\tau_{\Delta n}$, was calculated by fitting a single exponential to each decay trace. During CE measurements, the device was again held at open-circuit while the white light was on, but then switched to short-circuit when the light was turned off. The white LEDs were triggered by the function generator (10 Hz square wave, 50% duty cycle), and customized LabVIEW software was used to collect the voltage decay transient that was measured by the oscilloscope. The device was connected to a circuit (built in-house) containing

a switch that was open while the white light was on (charges build up in the device), and the switch closes when the white light turns off (charge measured as voltage transient by oscilloscope). The collected charge extraction voltage transients were converted to current transients using Ohm's Law (R = 511ohms), and the device area and thickness were used to calculate the current volume. The current volume curves were then integrated to determine charge carrier density, n.

BIBLIOGRAPHY

1. http://oxforddictionaries.com.
2. http://www.txses.org/solar/content/solar-energy-facts-you-should-know.
3. D. Chapin, C. Fuller and G. Pearson, *J. Appl. Phys.*, 1954, **25**, 676.
4. M. A. Green, K. Emery, Y. Hishikawa, W. Warta and E. D. Dunlop, *Progress in Photovoltaics: Research and Applications*, 2012, **20**, 12.
5. J. You, L. Dou, K. Yoshimura, T. Kato, K. Ohya, T. Moriarty, K. Emery, C.-C. Chen, J. Gao, G. Li and Y. Yang, *Nat. Commun.*, 2013, **4**, 1446.
6. R. Coffin, J. Peet, J. Rogers and G. Bazan, *Nat. Chem.*, 2009, **1**, 657.
7. Y. Li and Y. Zou, *Adv. Mater.*, 2008, **20**, 2952.
8. Y. Liang, Y. Wu, D. Feng, S. Tsai, H. Son, G. Li and L. Yu, *J. Am. Chem. Soc.*, 2009, **131**, 56.
9. J. Hou, H. Chen, S. Zhang, G. Li and Y. Yang, *J. Am. Chem. Soc*, 2008, **130**, 16144.
10. P. Troshin, H. Hoppe, J. Renz, M. Egginger, J. Mayorova, A. Goryachev, A. Peregudov, R. Lyubovskaya, G. Gobsch and N. Sariciftci, *Adv. Funct. Mater.*, 2009, **19**, 779.
11. C. Yang, J. Kim, S. Cho, J. Lee, A. Heeger and F. Wudl, *J. Am. Chem. Soc*, 2008, **130**, 6444.
12. M. Jørgensen, K. Norrman and F. Krebs, *Sol. Energ. Mat. Sol. Cells*, 2008, **92**, 686.
13. S. Hau, H. Yip, K. Leong and A. Jen, *Org. Electron.*, 2009, **10**, 719.
14. S. Hau, H. Yip, H. Ma and K. Alex, *Appl. Phys. Lett.*, 2008, **93**, 233304.
15. C. L. Braun, *J. Chem. Phys.*, 1984, **80**, 4157.
16. L. Onsager, *Phys. Rev.*, 1938, **54**, 554.
17. C. Deibel and V. Dyakonov, *Rep. Prog. Phys.*, 2010, **73**, 096401.
18. L. J. A. Koster, S. E. Shaheen and J. C. Hummelen, *Adv. Energy Mater.*, 2012, **2**, 1246.
19. M. Lenes, F. B. Kooistra, J. C. Hummelen, I. Van Severen, L. Lutsen, D. Vanderzande, T. J. Cleij and P. W. M. Blom, *J. Appl. Phys.*, 2008, **104**, 114517.
20. A. Tada, Y. Geng, Q. Wei, K. Hashimoto and K. Tajima, *Nat. Mater.*, 2011, **10**, 450.
21. C. Deibel, T. Strobel and V. Dyakonov, *Phys. Rev. Lett.*, 2009, **103**, 36402.
22. C. Schwarz, H. Bässler, I. Bauer, J. M. Koenen, E. Preis, U. Scherf and A. Köhler, *Adv. Mater.*, 2012, **24**, 922.
23. Y. Yuan, T. J. Reece, P. Sharma, S. Poddar, S. Ducharme, A. Gruverman, Y. Yang and J. Huang, *Nat. Mater.*, 2011, **10**, 296.
24. K. Asadi, P. de Bruyn, P. W. M. Blom and D. M. de Leeuw, *Appl. Phys. Lett.*, 2011, **98**, 183301.
25. K. Nalwa, J. Carr, R. Mahadevapuram, H. Kodali, S. Bose, Y. Chen, J. Petrich, B. Ganapathysubramanian and S. Chaudhary, *Energy Environ. Sci.*, 2012, **5**, 7042.
26. K. Sugi, H. Ishii, Y. Kimura, M. Niwano, E. Ito, Y. Washizu, N. Hayashi, Y. Ouchi and K. Seki, *Thin solid films*, 2004, **464**, 412.
27. S. Duhm, G. Heimel, I. Salzmann, H. Glowatzki, R. L. Johnson, A. Vollmer, J. P. Rabe and N. Koch, *Nat. Mater.*, 2008, **7**, 326.
28. H. L. Yip, S. K. Hau, N. S. Baek, H. Ma and A. K. Y. Jen, *Adv. Mater.*, 2008, **20**, 2376.
29. M. Pope and C. E. Swenberg, *Electronic processes in organic crystals and polymers*, Oxford University Press, Oxford, 1999.
30. P. Langevin, *Ann. Chim. Phys.*, 1903, **28**, 433.

31. C. J. Brabec, M. Heeney, I. McCulloch and J. Nelson, *Chem. Soc. Rev.*, 2011, **40**, 1185.
32. H. Hoppe and N. S. Sariciftci, *J. Mater. Chem.*, 2005, **16**, 45.
33. N. C. Giebink, B. E. Lassiter, G. P. Wiederrecht, M. R. Wasielewski and S. R. Forrest, *Physical Review B*, 2010, **82**, 155306.
34. C. Deibel and V. Dyakonov, *Reports on Progress in Physics*, 2010, **73**, 096401.
35. http://www.itacanet.org/the-sun-as-a-source-of-energy/part-2-solar-energy-reaching-the-earths-surface/.
36. C. Brabec, N. Sariciftci and J. Hummelen, *Adv. Funct. Mater.*, 2001, **11**, 15.
37. J. Halls, C. Walsh, N. Greenham, E. Marseglia, R. Friend, S. Moratti and A. Holmes, *Nature*, 1995, **376**, 498.
38. G. Yu, J. Gao, J. Hummelen, F. Wudl and A. Heeger, *Science*, 1995, **270**, 1789.
39. H. Chen, J. Hou, S. Zhang, Y. Liang, G. Yang, Y. Yang, L. Yu, Y. Wu and G. Li, *Nat. Photon.*, 2009, **3**, 649.
40. Y. Liang, Z. Xu, J. Xia, S. Tsai, Y. Wu, G. Li, C. Ray and L. Yu, *Adv. Mater.*, 2010, **22**, E135.
41. C. Kim, S. Lee, E. Gomez, J. Kim and Y. Loo, *Appl. Phys. Lett.*, 2009, **94**, 113302.
42. G. Lakhwani, R. Roijmans, A. Kronemeijer, J. Gilot, R. Janssen and S. Meskers, *J. Phys. Chem. C*, 293.
43. T. Kuwabara, Y. Kawahara, T. Yamaguchi and K. Takahashi, *ACS Appl. Mater. & Interfaces*, 2009, **1**, 2107.
44. T. Kuwabara, C. Iwata, T. Yamaguchi and K. Takahashi, *ACS Appl. Mater. & Interfaces*, 222.
45. S. Hau, H. Yip, O. Acton, N. Baek, H. Ma and A. Jen, *J. Mater. Chem.*, 2008, **18**, 5113.
46. S. Hau, Y. Cheng, H. Yip, Y. Zhang, H. Ma and A. Jen, *ACS Appl. Mater. & Interfaces*, 57.
47. C. Hsieh, Y. Cheng, P. Li, C. Chen, M. Dubosc, R. Liang and C. Hsu, *J. Am. Chem. Soc*, 2010, **132**, 4887.
48. D. A. Rider, B. J. Worfolk, K. D. Harris, A. Lalany, K. Shahbazi, M. D. Fleischauer, M. J. Brett and J. M. Buriak, *Adv. Funct. Mater.*, 2010, **20**, 2404.
49. L. Motiei, Y. Yao, J. Choudhury, H. Yan, T. J. Marks, M. E. Boom and A. Facchetti, *J. Am. Chem. Soc.*, 2010, **132**, 12528.
50. A. Werner, F. Li, K. Harada, M. Pfeiffer, T. Fritz and K. Leo, *Appl. Phys. Lett.*, 2003, **82**, 4495.
51. N. Cho, H. L. Yip, S. K. Hau, K. S. Chen, T. W. Kim, J. A. Davies, D. F. Zeigler and K. Y. J. Alex, *J. Mater. Chem.*, 2011, **21**, 6956.
52. K. Harada, F. Li, B. Maennig, M. Pfeiffer and K. Leo, *Appl. Phys. Lett.*, 2007, **91**, 092118.
53. A. Nollau, M. Pfeiffer, T. Fritz and K. Leo, *J. App. Phys.*, 2000, **87**, 4340.
54. K. Walzer, B. Maennig, M. Pfeiffer and K. Leo, *Chem. Rev*, 2007, **107**, 1233.
55. C. Chan and A. Kahn, *Applied Physics A: Materials Science & Processing*, 2009, **95**, 7.
56. C. Chan, W. Zhao, A. Kahn and I. Hill, *Appl. Phys. Lett.*, 2009, **94**, 203306.
57. P. Wei, J. Oh, G. Dong and Z. Bao, *J. Am. Chem. Soc.*, 2010, **132**, 8852.
58. F. Huang, Y. Cheng, Y. Zhang, M. Liu and A. Jen, *J. Mater. Chem.*, 2008, **18**, 4495.
59. A. Hains, J. Liu, A. Martinson, M. Irwin and T. Marks, *Adv. Funct. Mater.*, **20**, 595.
60. Y. Sun, X. Gong, B. Hsu, H. Yip, K. Alex and A. Heeger, *Appl. Phys. Lett.*, **97**, 193310.

61. R. Png, P. Chia, J. Tang, B. Liu, S. Sivaramakrishnan, M. Zhou, S. Khong, H. Chan, J. Burroughes and L. Chua, *Nat. Mater.*, 2009.
62. F. Kim, X. Guo, M. Watson and S. Jenekhe, *Adv. Mater.*, 2009, **22**, 478.
63. Z. Chen, Y. Zheng, H. Yan and A. Facchetti, *J. Am. Chem. Soc.*, 2009, **131**, 8.
64. H. Yan, Z. Chen, Y. Zheng, C. Newman, J. Quinn, F. Dotz, M. Kastler and A. Facchetti, *Nature*, 2009, **457**, 679.
65. M. Durban, P. Kazarinoff and C. Luscombe, *Macromolecules*, 2010, **43**, 6348.
66. S. X. Cai, J. Nabity, M. Wybourne and J. F. W. Keana, *Chem. Mater.*, 1990, **2**, 631.
67. X. Q. Zhu, M. T. Zhang, A. Yu, C. H. Wang and J. P. Cheng, *J. Am. Chem. Soc.*, 2008, **130**, 2501.
68. M. M. Durban, P. D. Kazarinoff and C. K. Luscombe, *Macromolecules*, 2010, **43**, 6348.
69. H. L. Yip and A. K. Y. Jen, *Ener. Environ. Sci.*, 2012, **5**, 5994.
70. H. Ma, H.-L. Yip, F. Huang and A. K. Y. Jen, *Adv. Funct. Mater.*, 2010, **20**, 1371.
71. C. Tengstedt, W. Osikowicz, W. R. Salaneck, I. D. Parker, C.-H. Hsu and M. Fahlman, *Appl.Phys. Lett.*, 2006, **88**, 053502.
72. I. Lange, J. C. Blakesley, J. Frisch, A. Vollmer, N. Koch and D. Neher, *Phys. Rev. Lett.*, 2011, **106**, 216402.
73. G. Li, C.-W. Chu, V. Shrotriya, J. Huang and Y. Yang, *Appl. Phys. Lett.*, 2006, **88**, 253503.
74. C. Waldauf, M. Morana, P. Denk, P. Schilinsky, K. Coakley, S. A. Choulis and C. J. Brabec, *Appl. Phys. Lett.*, 2006, **89**, 233517.
75. X. Bulliard, S.-G. Ihn, S. Yun, Y. Kim, D. Choi, J.-Y. Choi, M. Kim, M. Sim, J.-H. Park, W. Choi and K. Cho, *Adv. Funct. Mater.*, 2010, **20**, 4381.
76. D. S. Germack, C. K. Chan, B. H. Hamadani, L. J. Richter, D. A. Fischer, D. J. Gundlach and D. M. DeLongchamp, *Appl. Phys. Lett.*, 2009, **94**, 233303.
77. D. S. Germack, C. K. Chan, R. J. Kline, D. A. Fischer, D. J. Gundlach, M. F. Toney, L. J. Richter and D. M. DeLongchamp, *Macromolecules*, 2010, **43**, 3828.
78. D. Kim, Y. Park, Y. Jang, H. Yang, Y. H. Kim, J. Han, D. Moon, S. Park, T. Chang and C. Chang, *Adv. Funct. Mater.*, 2005, **15**, 77.
79. A. F. Tillack, K. M. Noone, B. A. MacLeod, D. Nordlund, K. P. Nagle, J. A. Bradley, S. K. Hau, H.-L. Yip, A. K.-Y. Jen and G. T. Seidler, *ACS Appl. Mater. Interfaces*, 2011, **3**, 726.
80. K. Lee, J. Y. Kim, S. H. Park, S. H. Kim, S. Cho and A. J. Heeger, *Adv. Mater.*, 2007, **19**, 2445.
81. V. C. Tung, J. Kim, L. J. Cote and J. Huang, *J. Am. Chem. Soc.*, 2011, **133**, 9262.
82. H. Kang, S. Hong, J. Lee and K. Lee, *Adv. Mater.*, 2012, **24**, 3005.
83. Y. Zhou, C. Fuentes-Hernandez, J. Shim, J. Meyer, A. J. Giordano, H. Li, P. Winget, T. Papadopoulos, H. Cheun, J. Kim, M. Fenoll, A. Dindar, W. Haske, E. Najafabadi, T. M. Khan, H. Sojoudi, S. Barlow, S. Graham, J. L. Brédas, S. R. Marder, A. Kahn and B. Kippelen, *Science*, 2012, **336**, 327.
84. Z. He, C. Zhong, X. Huang, W.-Y. Wong, H. Wu, L. Chen, S. Su and Y. Cao, *Adv. Mater.*, 2011, **23**, 4636.
85. C.-Z. Li, C.-C. Chueh, H.-L. Yip, K. M. O'Malley, W.-C. Chen and A. K.-Y. Jen, *J. Mater. Chem.*, 2012, **22**, 8574.
86. K. M. O'Malley, C.-Z. Li, H.-L. Yip and A. K.-Y. Jen, *Adv. Energy Mater.*, 2012, **2**, 82.
87. K. Walzer, B. Maennig, M. Pfeiffer and K. Leo, *Chem. Rev.*, 2007, **107**, 1233.

88. R. Meerheim, B. Lussem and K. Leo, *Proceedings of the IEEE*, 2009, **97**, 1606.
89. J. Drechsel, B. Mannig, F. Kozlowski, M. Pfeiffer, K. Leo and H. Hoppe, *Appl. Phys. Lett.*, 2005, **86**, 244102.
90. Y. Matsuo, Y. Sato, T. Niinomi, I. Soga, H. Tanaka and E. Nakamura, *J. Am. Chem. Soc.*, 2009, **131**, 16048.
91. A. Werner, F. Li, K. Harada, M. Pfeiffer, T. Fritz, K. Leo and S. Machill, *Adv. Funct. Mater.*, 2004, **14**, 255.
92. G. Parthasarathy, C. Shen, A. Kahn and S. Forrest, *J. Appl. Phys.*, 2001, **89**, 4986.
93. N. Cho, H. L. Yip, S. K. Hau, K. S. Chen, T. W. Kim, J. A. Davies, D. F. Zeigler and A. K. Y. Jen, *J. Mater. Chem.*, 2011, **21**, 6956.
94. N. Cho, H. L. Yip, J. A. Davies, P. D. Kazarinoff, D. F. Zeigler, M. M. Durban, Y. Segawa, K. M. O'Malley, C. K. Luscombe and A. K.-Y. Jen, *Adv. Energy Mater.*, 2011, **1**, 1148.
95. C.-Z. Li, C.-C. Chueh, H.-L. Yip, K. M. O'Malley, W.-C. Chen and A. K. Y. Jen, *J. Mater. Chem.*, 2012, **22**, 8574.
96. K. M. O'Malley, C.-Z. Li, H.-L. Yip and A. K. Y. Jen, *Adv. Energy Mater.*, 2012, **2**, 82.
97. C.-Z. Li, C.-C. Chueh, F. Ding, H.-L. Yip, L. P.-W., X. Li and J. A. K.-Y., *Adv. Mater.*,, 2013, **25**, 4425.
98. C.-Z. Li, C.-C. Chueh, H.-L. Yip, F. Ding, X. Li and A. K.-Y. Jen, *Adv. Mater.*, 2013, **25**, 2457.
99. Y. J. Cheng, C. H. Hsieh, P. J. Li, C. H. Chen, M. Dubosc, R. M. Liang and C. S. Hsu, *J. Am. Chem. Soc.*, 2010, **132**, 4887.
100. M. T. Rispens, A. Meetsma, R. Rittberger, C. J. Brabec, N. S. Sariciftci and J. C. Hummelen, *Chem. Commun.*, 2003, **0**, 2116.
101. S.-I. Na, T.-S. Kim, S.-H. Oh, J. Kim, S.-S. Kim and D.-Y. Kim, *Appl. Phys. Lett.*, 2010, **97**, 223305.
102. Y. Zhou, F. Li, S. Barrau, W. Tian, O. Inganäs and F. Zhang, *Sol. Energy Mater. Sol. Cells*, 2009, **93**, 497.
103. C.-Z. Li, C.-C. Chueh, H.-L. Yip, K. M. O'Malley, W.-C. Chen and A. K. Y. Jen, *J. Mater. Chem.*, 2012, **22**, 8574.
104. J. F. Salinas, H. L. Yip, C. C. Chueh, C. Z. Li, J. L. Maldonado and A. K.-Y. Jen, *Adv. Mater.*, 2012, **24**, 6362.
105. E. L. Ratcliff, B. Zacher and N. R. Armstrong, *J. Phys. Chem. Lett.*, 2011, **2**, 1337.
106. R. Steim, F. R. Kogler and C. J. Brabec, *J. Mater. Chem.*, 2010, **20**, 2499.
107. W. J. Potscavage Jr, A. Sharma and B. Kippelen, *Acc. Chem. Res.*, 2009, **42**, 1758.
108. L.-M. Chen, Z. Xu, Z. Hong and Y. Yang, *J. Mater. Chem.*, 2010, **20**, 2575.
109. H. Ma, H. L. Yip, F. Huang and A. K. Y. Jen, *Adv. Funct. Mater.*, 2010, **20**, 1371.
110. C.-Z. Li, C.-Y. Chang, Y. Zang, H.-X. Ju, C.-C. Chueh, P.-W. Liang, N. Cho, D. S. Ginger and A. K.-Y. Jen, *Adv. Mater.*, 2014, **26**, 6262.
111. H. Ishii, K. Sugiyama, E. Ito and K. Seki, *Adv. Mater.*, 1999, **11**, 605.
112. D. Donetsky, S. Anikeev, G. Belenky, S. Luryi, C. Wang and G. Nichols, *Appl. Phys. Lett.*, 2002, **81**, 4769.
113. A. Wagenpfahl, D. Rauh, M. Binder, C. Deibel and V. Dyakonov, *Phys. Rev. B*, 2010, **82**, 115306.
114. J. Drechsel, B. Männig, F. Kozlowski, M. Pfeiffer, K. Leo and H. Hoppe, *Appl. Phys. Lett.*, 2005, **86**, 244102.

115. S. Guo, S. B. Kim, S. K. Mohapatra, Y. Qi, T. Sajoto, A. Kahn, S. R. Marder and S. Barlow, *Adv. Mater.*, 2012, **24**, 699.
116. C.-Z. Li, C.-C. Chueh, H.-L. Yip, F. Ding, X. Li and A. K. Y. Jen, *Adv. Mater.*, 2013, **25**, 2457.
117. N. Cho, C.-Z. Li, H.-L. Yip and A. K. Y. Jen, *Energy Environ. Sci.*, 2014, **7**, 638.
118. N. Cho, H. L. Yip, J. A. Davies, P. D. Kazarinoff, D. F. Zeigler, M. M. Durban, Y. Segawa, K. M. O'Malley, C. K. Luscombe and A. K. Y. Jen, *Adv. Energy Mater.*, 2011, **1**, 1148.
119. L. Zuo, C.-C. Chueh, Y.-X. Xu, K.-S. Chen, Y. Zang, C.-Z. Li, H. Chen and A. K.-Y. Jen, *Adv. Mat.*, 2014, **26**, 6778.
120. K. M. O'Malley, C. Z. Li, H. L. Yip and A. K. Y. Jen, *Adv. Energy Mater.*, 2012, **2**, 82.
121. S. Dhariwal and D. Mehrotra, *Solid-State Electron.*, 1988, **31**, 1355.
122. T. Kirchartz and J. Nelson, *Phys. Rev. B*, 2012, **86**, 165201.
123. A. Wagenpfahl, C. Deibel and V. Dyakonov, *IEEE J. Sel. Top. Quantum Electron.*, 2010, **16**, 1759.
124. J. G. Fossum, *IEEE Trans. Electron Devices*, 1977, **24**, 322.
125. T.-W. Jung, F. A. Lindholm and A. Neugroschel, *IEEE Trans. Electron Devices*, 1984, **31**, 588.
126. E. V. Kerschaver and G. Beaucarne, *Prog. Photovolt.*, 2006, **14**, 107.
127. Z. Shuai, L. Wang and C. Song, *Theory of charge transport in carbon electronic materials*, Springer, Berlin Heidelberg, 2012.
128. K. S. Chen, H.-L. Yip, C. W. Schlenker, D. S. Ginger and A. K.-Y. Jen, *Org. Electron.*, 2012, **13**, 2870.
129. G. Li, Y. Yao, H. Yang, V. Shrotriya, G. Yang and Y. Yang, *Adv. Funct. Mater.*, 2007, **17**, 1636.
130. F. Padinger, R. S. Rittberger and N. S. Sariciftci, *Adv. Funct. Mater.*, 2003, **13**, 85.
131. G. Li, V. Shrotriya, J. Huang, Y. Yao, T. Moriarty, K. Emery and Y. Yang, *Nature Mater.*, 2005, **4**, 864.
132. L. Ye, S. Zhang, W. Ma, B. Fan, X. Guo, Y. Huang, H. Ade and J. Hou, *Adv. Mater.*, 2012, **24**, 6335.
133. T. Y. Chu, S. Alem, S. W. Tsang, S. C. Tse, S. Wakim, J. Lu, G. Dennler, D. Waller, R. Gaudiana and Y. Tao, *App. Phys. Lett.*, 2011, **98**, 253301.
134. X. Guo, C. Cui, M. Zhang, L. Huo, Y. Huang, J. Hou and Y. Li, *Energy Environ. Sci.*, 2012, **5**, 7943.
135. J. Peet, J. Kim, N. E. Coates, W. L. Ma, D. Moses, A. J. Heeger and G. C. Bazan, *Nature Mater.*, 2007, **6**, 497.
136. Y.-X. Xu, C.-C. Chueh, H.-L. Yip, F.-Z. Ding, Y.-X. Li, C.-Z. Li, X. Li, W.-C. Chen and A. K.-Y. Jen, *Adv. Mater.*, 2012, **24**, 6356.
137. Y. Zhang, J. Zou, H.-L. Yip, K. S. Chen, J. A. Davies, Y. Sun and A. K.-Y. Jen, *Macromolecules*, 2011, **44**, 4752.
138. Y. Zhang, J. Zou, H.-L. Yip, K. S. Chen, D. F. Zeigler, Y. Sun and A. K.-Y. Jen, *Chem. Mater.*, 2011, **23**, 2289.
139. A. Mayer, M. F. Toney, S. R. Scully, J. Rivnay, C. J. Brabec, M. Scharber, M. Koppe, M. Heeney, I. McCulloch and M. D. McGehee, *Adv. Funct. Mater.*, 2009, **19**, 1173.
140. F. C. Jamieson, E. B. Domingo, T. McCarthy-Ward, M. Heeney, N. Stingelin and J. R. Durrant, *Chem. Sci.*, 2012, **3**, 485.

141. C. M. Hansen, *Hansen solubility parameters: a user's handbook*, CRC Press, Boca Ranton, FL. USA, 2002.
142. J. H. Hildebrand and R. Scott, *J. Chem. Phys.*, 1952, **20**, 1520.
143. B. Walker, A. Tamayo, D. T. Duong, X. D. Dang, C. Kim, J. Granstrom and T. Q. Nguyen, *Adv. Energy Mater.*, 2011, **1**, 221.
144. L. J. A. Koster, V. D. Mihailetchi, R. Ramaker and P. W. M. Blom, *Appl. Phys. Lett.*, 2005, **86**, 123509.
145. J. L. Brédas, J. E. Norton, J. Cornil and V. Coropceanu, *Acc. Chem. Res.*, 2009, **42**, 1691.
146. D. Credgington, F. C. Jamieson, B. Walker, T. Q. Nguyen and J. R. Durrant, *Adv. Mater.*, 2012, **24**, 2135.
147. A. Maurano, C. G. Shuttle, R. Hamilton, A. M. Ballantyne, J. Nelson, W. Zhang, M. Heeney and J. R. Durrant, *J. Phys. Chem. C*, 2011, **115**, 5947.
148. A. A. Bakulin, A. Rao, V. G. Pavelyev, P. H. van Loosdrecht, M. S. Pshenichnikov, D. Niedzialek, J. Cornil, D. Beljonne and R. H. Friend, *Science*, 2012, **335**, 1340.
149. C. W. Schlenker and M. E. Thompson, *Chem.Commun.*, 2011, **47**, 3702.
150. M. Breselge, I. Van Severen, L. Lutsen, P. Adriaensens, J. Manca, D. Vanderzande and T. Cleij, *Thin solid films*, 2006, **511**, 328.
151. Y. Sun, S. C. Chien, H. L. Yip, K. S. Chen, Y. Zhang, J. A. Davies, F. C. Chen, B. Lin and A. K. Y. Jen, *J. Mater. Chem.*, 2012, **22**, 5587.
152. J. Frenkel, *Phys. Rev.*, 1931, **37**, 17.
153. C. T. Sah, *Fundamentals of solid-state electronics*, World Scientific, 1991.
154. K. Vandewal, K. Tvingstedt, A. Gadisa, O. Inganäs and J. V. Manca, *Nat. Mater.*, 2009, **8**, 904.
155. Y. Geng, Q. Wei, K. Hashimoto and K. Tajima, *Chem. Mater.*, 2011, **23**, 4257.
156. V. Lachat, V. Varshney, A. Dhinojwala and M. S. Yeganeh, *Macromolecules*, 2009, **42**, 7103.
157. P. Kett, M. Casford and P. Davies, *Mol. Phys.*, 2013, **111**, 175.
158. R. A. Street, S. Cowan and A. J. Heeger, *Phys. Rev. B*, 2010, **82**, 121301.
159. A. Foertig, A. Wagenpfahl, T. Gerbich, D. Cheyns, V. Dyakonov and C. Deibel, *Adv. Energy Mater.*, 2012, **2**, 1483.
160. B. P. Rand, D. P. Burk and S. R. Forrest, *Phys. Rev. B*, 2007, **75**, 115327.
161. G. Garcia-Belmonte, P. P. Boix, J. Bisquert, M. Lenes, H. J. Bolink, A. La Rosa, S. Filippone and N. Martín, *J. Phys. Chem. Lett.*, 2010, **1**, 2566.
162. P. A. Franken and J. F. Ward, *Rev. Mod. Phys.*, 1963, **35**, 23.
163. Y. Shen, *Nature*, 1989, **337**, 519.